UC-426

SAWTEETH IN THE MST REVERSED FIELD PINCH

J.A. Beckstead

DOE/ER/53198-167 September 1990

NOTICE

Printed in the United States of America
Available from
National Technical Information Service
U.S. Department of Commerce
5285 Port Royal Road
Springfield, VA 22161

NTIS Price codes
Printed copy: A07
Microfiche copy: A01

SAWTEETH IN THE MST REVERSED FIELD PINCH

by

Jeffrey Andrew Beckstead

A thesis submitted in partial fulfillment of the
requirements for the degree of

Doctor of Philosophy
(Physics)

at the

University of Wisconsin-Madison

September 1990

ABSTRACT

A dynamo mechanism has been used in astrophysics to explain the self-generation of the magnetic fields observed throughout the universe. This same type of phenomenon is believed to occur in the reversed field pinch (RFP) plasmas. The RFP dynamo has been a major theoretical and experimental investigation since the first observations of the self-reversal process in early pinch research. A discrete dynamo event has been observed in the experimental RFP plasmas; this event is termed the RFP sawtooth. This phenomenon is similar to the sawtooth phenomenon observed in tokamak plasmas, but the two events differ in many respects. Both events are a result of the inward diffusion of the plasma current density. This causes the plasma to become unstable to the m = 1 tearing modes. It has been shown theoretically that the nonlinear interaction of these modes can generate the reversed toroidal field in the RFP. This thesis is a study of the RFP sawtooth phenomenon on the MST RFP. This includes experimental observations as well as 1-D numerical simulations of the sawtooth rise-time. During the rise-time of the sawtooth, the plasma is undergoing a purely diffusive process - no dynamo is occuring during this phase. The dynamo only occurs during the sawtooth crash. During the rise-time, the m = 1 modes are observed to grow, and nonlinear interactions are observed prior to the sawtooth crash. At the time of the crash, many of the plasma profiles are flattened; these include the current density, the plasma temperature and the plasma density. The period of the sawteeth is observed to increase with

the plasma current, as well as the magnetic Reynolds number, S. In the MST, sawteeth are observed at all values of Θ, including nonreversed discharges. The sawtooth activity increases with Θ as predicted by 3-D MHD simulations. This increase is observed in the amount of toroidal flux generated during the sawtooth crash, as well as in the period of the sawtooth.

ACKNOWLEDGEMENTS

Where do I start ...

First of all, I would like to thank Richard Dexter. Thank you for your guidance and the freedom to do my own thing, even though it was sometimes wrong. I wish you the best of luck and happiness in your many years of retirement - happy camping, camper. Next I would like to thank the one who is responsible for me continuing my education and entering graduate school, Morton Fineman. I have cursed you many times over the last six years, but thank you for the encouragement during my stay at Lycoming and in the years since. It was worth it, and you were correct, I can handle it. (An interesting note to add - why do my advisors always retire when I graduate ?)

To Richard Nebel and Kenneth Werley of Los Alamos National Laboratory, thank you for a wonderful time in Los Alamos and for your assistance in learning RFPB. (A special note to Rick, thank you for answering all those theoretical questions I kept asking you; the answers were very useful in understanding the sawteeth as well as RFPs in general).

Now back in Madison... I would like to thank all those whose help I have appreciated enormously. This includes all the professors, and the graduate students, those who helped me get through both the qualifier and the prelim (back when the prelim was an exam !), and all those

student hourlies who have experienced that wonderful world of "big time research". A special thanks to those who get left in the background, but are needed to survive. John Laufenberg, I will always remember my introduction to plasma physics - sanding the inside of the Octupole. Glenn Fleet, you can remove all my data requests now. Kay Shatrawka, you put up with so much and get so little in return, thank you very much for the help with the little things over the years.

A special thanks goes out to those two "Chicos" and the "Fins" for keeping me from going insane over the last few years. I owe all of you a beer at the "Onion" some Friday afternoon; say about 3 o'clock?

On a more personal note, I would like to give my thanks to my friends and family for both the support and the opportunities to get away, especially to *Keeeeewauuuuneeee*. Thanx, Dad, Deb, Lauri, Becky and Micah (even though you won't be able to read this for a few years), Art and Judy, Penny, Kevin and Mary, and Ron and Michele.

To the one who has put up with the most, I would like to dedicate this thesis to my loving wife Diane. She has followed me out to this "cow country" and now she doesn't want to leave. You have put up with six long years of "Physics on the brain", especially the last few months. I love you for it, and let's go on a long vacation ! **You deserve it !**

TABLE OF CONTENTS

overcome the classical diffusion.[4] This *regeneration* of reversed-toroidal field is termed the *dynamo effect* in analogy to the dynamo which occurs in astrophysics.[5] The method of *regeneration* is unknown, and is one of the prime areas of RFP research both theoretically, and experimentally. This thesis is an experimental attempt to understand the dynamo in the RFP - it is a study of the sawtooth phenomena in the MST device.

In the early 1980's, discrete events were observed on the ZT-40M RFP[6] during deeply reversed or high Θ discharges (Θ is referred to as the pinch parameter, and is defined as $\Theta \equiv \frac{B_\theta(a)}{<B_\phi>}$ where $B_\theta(a)$ is the poloidal field at the wall, and $<B_\phi>$ is the average toroidal field, defined as $<B_\phi> \equiv \Phi_\phi / \pi a^2 = \int B_\phi \, da_\phi / \pi a^2$). At each event or *"flux jump"*, the average toroidal field, $<B_\phi>$, increased, while the toroidal field at the wall, $B_\phi(a)$, decreased with little or no change in the toroidal plasma current (see figure 1.2). Since the toroidal field at the wall, $B_\phi(a)$, is in the opposite direction to the axial toroidal field, the increase in the total toroidal flux, $<B_\phi>$, and the simultaneous increase in the reversal, $B_\phi(a)$, can only occur if additional toroidal flux is created inside the plasma boundary. This will be explained in more detail in chapter 2.

After each flux jump, the toroidal field decays classically, the average toroidal field decreasing, and the toroidal field at the wall increasing (becoming less negative). This interval has been shown to be a purely

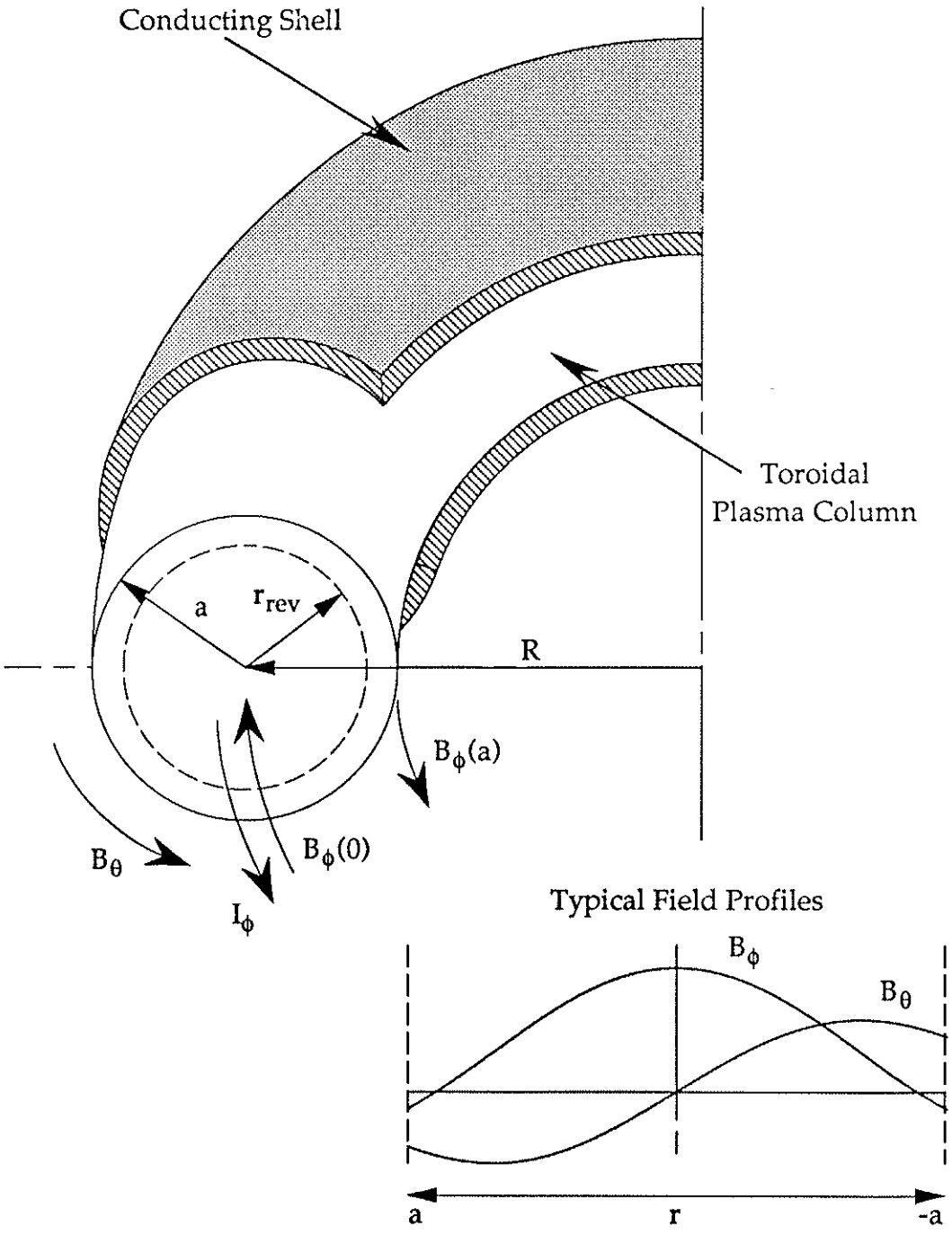

Figure 1.1: Magnetic geometry for the RFP.

resistive process by Werley, et al.[7] Using a 1-D transport code, the toroidal field decay was successfully modeled for the ZT-40M device. This simulation did not include any model of the dynamo effect; however, in the ZT-40M discharges, reversal was maintained. This implies that the reversal was maintained purely by the presence of the flux jumps - the flux jumps appeared to be discrete dynamo events!

During the interval while the fields are decaying, the central chord soft x-ray emission increases due to the heating of the center of the discharge (the soft x-ray emission from a plasma increases with the temperature and the density of the plasma). This interval will be referred to as the *"rise-time"* of the flux jump. The emission continues to increase until the next flux jump occurs, at which time the emission decreases suddenly. Afterwards, the heating reoccurs. This gives the appearance of a *"sawtooth"* oscillation in the central chord soft x-ray signal, see figure 1.2.

The *sawtooth* feature in the central chord soft x-ray emission has been observed in tokamaks for quite some time.[8] It is a result of the center of the plasma heating which allows the current density to diffuse radially inward generating peaked current profiles.[9] When the central current density increases to the point that the on-axis safety factor falls below unity, $q(0) \equiv rB_\phi/RB_\theta < 1$, the tokamak plasma becomes unstable to the (m,n) = (1,1) tearing mode (m being the poloidal mode number and n being the toroidal mode number). The unstable mode grows at an accelerated growth rate until it magnetically reconnects. The

reconnection flattens the current profiles, stabilizing the plasma. As the mode increases in amplitude, the center of the plasma becomes stochastic. This allows for a rapid radial transport of the plasma from the hot central region to the cooler edge. This is seen experimentally as a sudden decrease in the central soft x-ray emission and as an increase in the edge soft x-ray emission. This process is repeated as the center of the plasma begins to reheat, resulting in the sawtooth oscillation observed in the central soft x-ray emission.

The process in the RFP is quite different, but the similarity between the sawteeth in the soft x-ray signals observed during the RFP *flux jumps* and those observed during the tokamak *sawteeth* resulted in the RFP phenomena being termed *sawteeth* as well. From this point on, the term *sawtooth* will be used to describe the RFP *flux jump* phenomenon. The term *sawtooth crash* will refer to the sudden drop in the central chord soft x-ray signal. This corresponds to the increase in the average toroidal field and the decrease in toroidal field at the wall. The term *sawtooth rise-time* will refer to the heating phase of the sawtooth. In some instances the term *flux jump* will still be used to distinguish the magnetic event from the soft x-ray crash.

Since their first observation on ZT-40M, sawteeth have been observed on many other RFP's throughout the world when operated at high values of Θ,[10] typically $\Theta \geq 1.6$. During the initial operation of the MST, sawteeth have been observed at all values of Θ, even in nonreversed

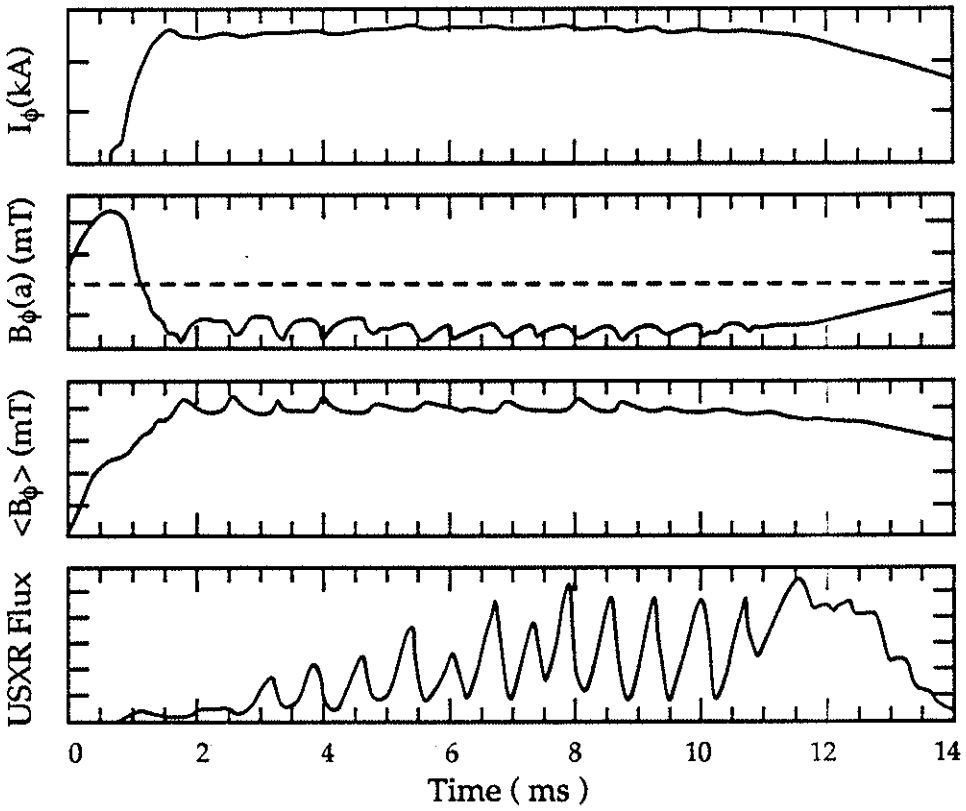

Figure 1.2: Flux jumps / sawteeth observed in the ZT-40M RFP (reproduced from Ref. 11).

discharges. The sawteeth appeared to be the only occurrence of the RFP dynamo in many of the MST discharges. This thesis is a study of the sawteeth in the MST device.

The organization of this thesis is as follows. Chapter 2 is a brief review of the RFP confinement device and its equilibrium characteristics. A review of the sawtooth theory will also be given in this chapter. Connections to the tokamak configuration and its sawtooth

theory will also be presented in order to identify the similarities and differences between the two sawtooth phenomena. The MST device is described in chapter 3 as well as some of the diagnostics used for this thesis. Chapter 4 presents the experimental results of this thesis. Comparisons with sawteeth on other RFP devices will be made in this chapter. The results of a 1-D modeling of the sawtooth rise-time will be presented in chapter 5. This is similar to the modeling of the ZT-40M sawteeth by Werley, et al. mentioned above. A summary of the results and conclusions of this research are presented in chapter 6.

References

[1]H. A. B. Bodin, A. A. Newton, Nucl. Fusion **20**, 1255 (1980).

[2]see for example, J. P. Friedberg, Rev. Mod. Phys. **54**, 801 (1982).

[3]J. B. Taylor, Rev. Mod. Phys. **58**, 741 (1986).

[4]E. J. Caramana, and D. A. Baker, Nuc. Fusion **24**, 423 (1984).

[5]H. K. Moffatt, *Magnetic Field Generation in Electrically Conducting Fluids* (Cambridge Univ. Press, Cambridge 1978).

[6]R. G. Watt, and R. A. Nebel, Phys. Fluids **26**, 1168 (1983).

[7]K. A. Werley, R. A. Nebel, and G. A. Wurden, Phys. Fluids **28**, 1450 (1985).

[8]S. von Goeler, W. Stodiek, and N. Sauthoff, Phys. Rev. Lett. **33**, 1201 (1974).

[9]see for example, G. L. Jahns, M. Soler, B. V. Waddell, J. D. Callen, and H. R. Hicks, Nucl. Fusion **18**, 609 (1978).

[10]see for example, V. Antoni, and S. Ortolani, Phys. Fluids **30**, 1489 (1987); Y. Hirano, Y. Kondoh, Y. Maejima, Y. Nogi, K. Ogawa, M. Sato, T. Shimada, T. Tagi, and H. Yoshimura, in *Proc. 10th Int. Conf. on Plasma Physics and Controlled Nuclear Fusion Researc*, London, 1984 (IAEA, Vienna, 1985), Vol. 2, p. 475; or

H. Y. W. Tsui, and J. Cunnane, Plasma Phys. and Cont. Fusion **30**, 865 (1988).

[11]R. A. Nebel, K. A. Werley, and M. M. Pickrell, Los Alamos National Laboratory Report LA-10653-MS (1986).

CHAPTER 2

A REVIEW OF THE RFP CONFIGURATION AND SAWTOOTH THEORY

Although the RFP concept has been studied for quite some time, it is in the early stages of experimental research. This is in contrast to the tokamak which is probably the most studied magnetic fusion device. The two concepts are very similar, the differences being primarily due to the magnetic topology. This chapter will give a brief review of the RFP concept and its equilibrium characteristics. Comparisons will be made with the tokamak equilibrium in order to later compare the sawtooth theory of the RFP to that of the tokamak. This will be presented in section 2.2. Detailed reviews of the RFP configuration can be found in references 1-3, and reviews of the tokamak configuration can be found in references 4 and 5.

2.1 Review of the RFP equilibrium

The RFP plasma, like that of the tokamak, is confined by a poloidal field, B_θ, which is created by the plasma's toroidal current and a toroidal field, B_ϕ, which is created by currents in external windings. The major difference between the two devices is the strength of the magnetic fields. In the RFP, the magnetic fields are comparable in strength, that is $| B_\phi | \approx B_\theta$, while in the tokamak, the toroidal field is much stronger than the poloidal field, $B_\phi \gg B_\theta$. Also, the RFP's toroidal field on the edge

reverses direction relative to the axial toroidal field. Figure 2.1 shows the magnetic field profiles of the RFP and the tokamak for comparison.

One of the first RFP devices was the ZETA device at Harwell (see reference 3 for a review of the ZETA results). On this device, an increase in stability was observed when the toroidal field at the wall reversed direction relative to the axial toroidal field. This field reversal occurred spontaneously and was termed *self-reversal*. During the reversed period, the fluctuation levels decreased dramatically, and the global plasma parameters such as the electron temperature and the confinement time increased until the reversal was lost. This same phenomenon is also observed in modern RFP devices which are able to maintain the reversed state much longer than the original ZETA device.

This self-reversal process can be explained by a minimum energy state developed by Taylor[6] in the early 70's. If one considers a pressureless, low resistance plasma that is bounded by a perfectly conducting wall, the total magnetic helicity within the plasma is an invariant. The total magnetic helicity is defined as

$$K = \int \mathbf{A} \cdot \mathbf{B} \, d\tau \qquad 2\text{-}1$$

where $\mathbf{A}$ is the magnetic vector potential satisfying $\nabla \times \mathbf{A} = \mathbf{B}$, and the integration is taken over the entire plasma volume. Using this constraint to minimize the magnetic energy, the equilibrium magnetic fields can then be described by

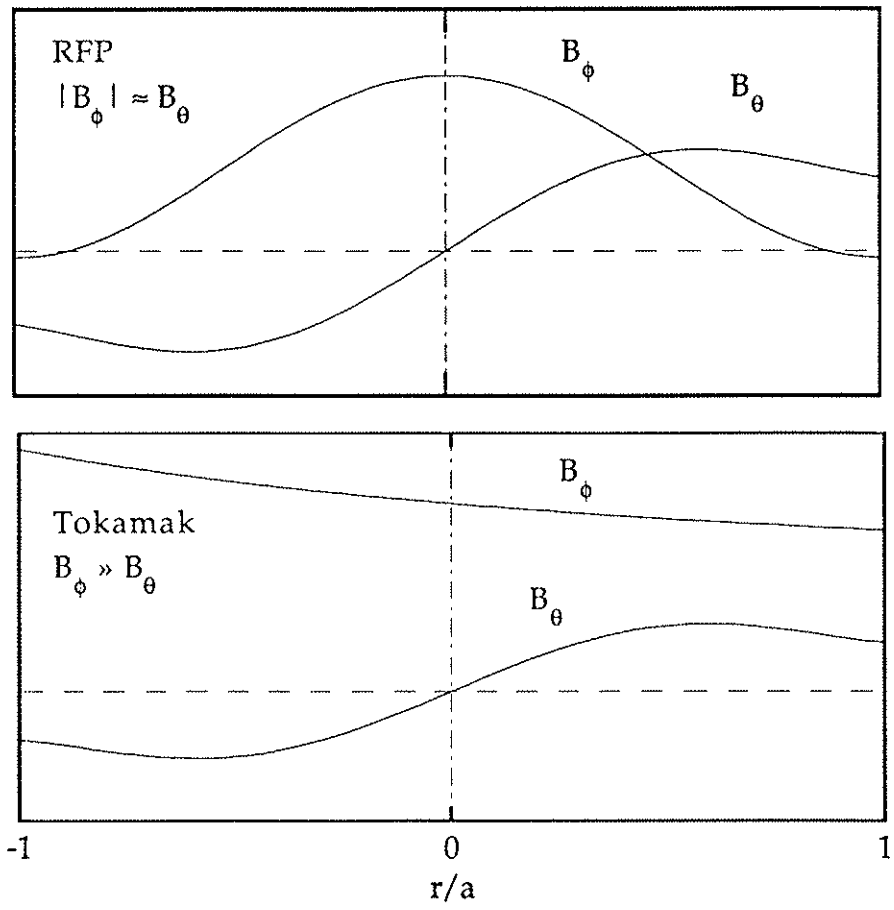

Figure 2.1: Comparison of the magnetic field profiles for the RFP and the tokamak.

$$\nabla \times \mathbf{B} = \lambda \mathbf{B} \qquad 2\text{-}2$$

where λ is a constant. The value of λ is specified by the values of the total magnetic helicity and of the total toroidal flux, $\Phi_\phi = \int da_\phi B_\phi = \pi a^2 < B_\phi >$.

Due to the large aspect ratio of many RFP experiments, toroidal curvature effects are minor, so the RFP can often be approximated as a periodic circular cylinder. Using this approximation, the solutions to Eq. 2-2 are known as the Bessel Function Model (BFM), and the magnetic fields are given by

$$B_\phi = B_o J_o(\lambda r), \quad B_\theta = B_o J_1(\lambda r), \quad B_r = 0 \qquad 2\text{-}3$$

where J_o and J_1 are the zeroeth and first order Bessel functions and B_o is the magnetic field strength on axis. This model predicts reversal in the toroidal field for $\lambda a > 2.4$. Figure 2.2 shows these solutions along with experimentally measured profiles from the HBTX1A RFP.[7] The BFM model fits the data reasonably well with the departure being mainly in the edge region. The reason for this departure will be discussed below.

RFP equilibria are typically expressed in terms of the normalized edge magnetic fields. This is accomplished by defining two parameters, F (the reversal parameter) and Θ (the pinch parameter):

$$F \equiv \frac{B_\phi(a)}{<B_\phi>}, \text{ and } \Theta \equiv \frac{B_\theta(a)}{<B_\phi>}. \qquad 2\text{-}4$$

For the BFM, these two parameters are related by the following expression:

$$F = \Theta \frac{J_o(2\Theta)}{J_1(2\Theta)} \qquad 2\text{-}5$$

In this formalism, reversal, $F < 0$, is predicted for $\Theta > 1.2$, and Θ is related to λ by the relation $\Theta = a\lambda/2$.

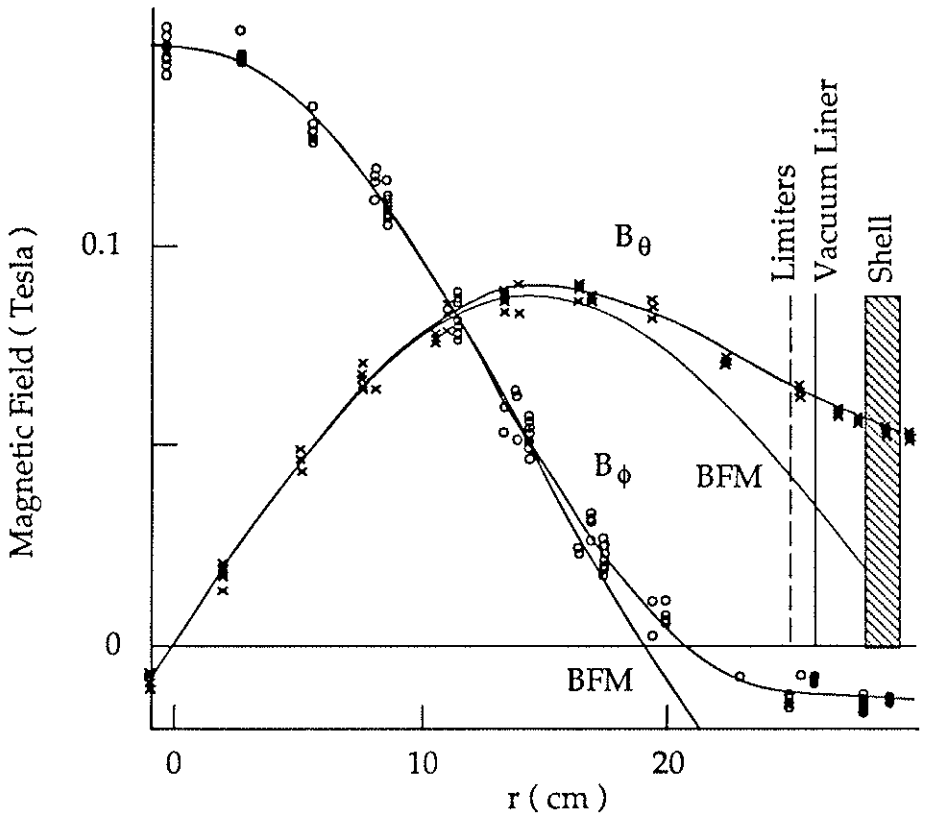

Figure 2.2: Experimentally measured magnetic profiles in the HBTX1A RFP and the profiles derived for the BFM (adapted from Fig. 4 of Ref. 7).

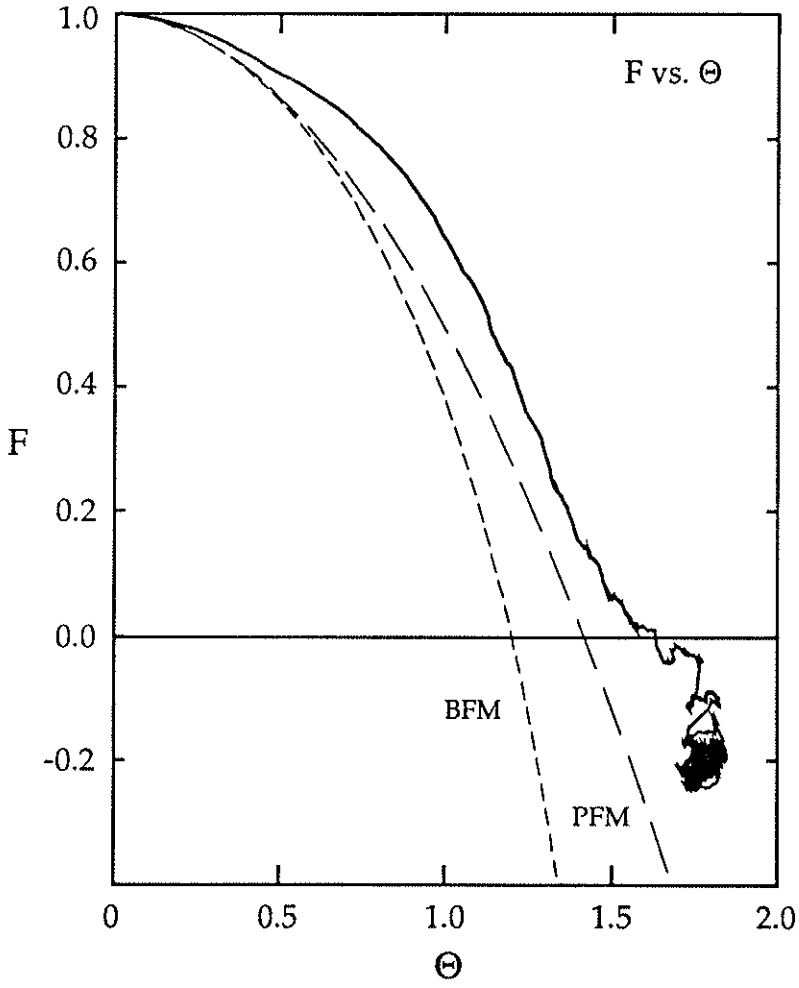

Figure 2.3: A F-Θ diagram for a MST discharge. Dashed line is that predicted by the BFM, Eq. 2-5. Long dash line is that predicted by the Polynomial Function Model, PFM (this model is used on the MST and will be described in chapter 3).

RFP experiments are thought to evolve from their non-reversed configuration at start-up to their reversed "steady state" configuration through a set of Taylor's minimum energy states. This feature is shown in figure 2.3 where F and Θ are plotted for a MST discharge. Also plotted is the BFM relation, Eq. 2-5. The plasma tends to follow the trajectory, but lies to the right of the BFM curve. The reason for this departure is discussed next.

In equation 2-2, λ can be expressed as $\lambda = \mathbf{J} \cdot \mathbf{B} \ / \ B^2$ (the normalized parallel current). The BFM requires λ to be a constant across the plasma radius. In experiments J is zero at the wall primarily due to the high resistivity at the edge of the plasma. It also varies smoothly in the edge. As a result, λ must go to zero at the edge - it cannot be constant across the entire plasma region. Secondly, the BFM assumes a pressureless plasma which is unrealistic. The violation of these two assumptions results in the experimental plasmas lying above the minimum energy state, the BFM curves, as can be seen in figures 2.2 and 2.3. Various other models have been developed which include a more realistic plasma by decreasing J on the edge, as well as including the effect of the plasma pressure. One such model is the Polynomial Function Model (PFM)[8] which is often used on the MST. This model will be discussed in more detail in chapter 3. The F-Θ curve for this model is also shown in figure 2.3. It lies closer to the experimental curve, but again it does not follow exactly. Reference 3 can be seen for more detail on the other plasma models.

Even though the Taylor minimum energy state can explain why the edge toroidal field reverses direction, the reversed configuration cannot be maintained in a cylindrically symmetric, resistive plasma. This is a result of applying Cowling's theorem to the RFP.[9] By integrating Faraday's law over the plasma cross section, the time rate of change of the total toroidal flux can be related to the poloidal emf at the wall:

$$\frac{\partial \Phi_\phi}{\partial t} = -2\pi a E_\theta(a) . \qquad 2\text{-}6$$

Thus, for a cylindrically symmetric plasma, the total toroidal flux, Φ_ϕ, can only change by what is "pushed in" or "pulled out" at the surface (r = a). Similarly, $B_\phi(r_{rev}) = 0$ at the reversal surface, and the poloidal current is positive, $J_\theta(r_{rev}) > 0$; see figure 2.2. Consequently, the component of Ohm's law parallel to **B** is given by $E_\theta(r_{rev}) = \eta J_\theta(r_{rev})$, which is positive. This result in combination with the derivation leading to Eq. 2-6 requires that the toroidal flux inside the reversal surface must decrease.

This effect was demonstrated by a one dimensional magnetohydrodynamic (MHD) simulation by Caramana and Baker in which they showed that an RFP equilibrium cannot be maintained classically.[10] The reversed equilibrium was lost by resistive diffusion on a very short time scale in comparison with experimental time scales (less than 1% of the experimental discharge time). The loss of reversal was independent of the assumed resistivity profile. This result will be important in discussing the sawtooth rise-time simulations in chapter 5.

However, experimental RFPs typically maintain equilibria for several resistive diffusion times, and many see an increase in the total toroidal flux at the same time that the reversal is deepening. Both are violations of Cowling's theorem. This requires some mechanism internal to the plasma which is generating the reversed field; this mechanism is called the *dynamo*.

Likewise, the RFP sawtooth described in chapter 1 is a violation of the equation 2-6. The total toroidal flux increased while the toroidal field at the edge decreased. For this to occur, the toroidal field must be created internal to the plasma. Any externally created *positive* flux would decrease the amount of reversal (increase the $B_\phi(a)$ signal), not deepen the reversal. On the other hand, if *negative* flux was created externally - which would deepen the reversal - the total toroidal flux would decrease, not increase. As a result, the flux must be created internally - the sawtooth crash is a discrete dynamo event.

2.2 Review of RFP Sawtooth theory

As described above, the RFP equilibrium is fairly well understood, but in order to maintain the reversed configuration, the plasma must create the additional reversed toroidal field needed to overcome the classical diffusion process. This effect cannot be explained by simple linear MHD theory as demonstrated by Caramana and Baker. Many theoretical models have been proposed which attempt to explain the dynamo mechanism. These models either include a dynamo electric field which

is driven by kinetic effects[11] or include nonlinear interactions of the MHD instabilities to drive the dynamo.[12-19] The one which has been the most relevant to the RFP sawtooth phenomena is the nonlinear MHD model. This theory has been successful in simulating the RFP sawtooth.[20] However, this does not exclude the kinetic dynamo from occurring, especially at low values of Θ where strong sawtooth activity is not observed on many of the experiments. While the MHD model is the most relevant to the RFP sawtooth at this time, it has not been proved to explain the dynamo mechanism completely.

A brief description of the nonlinear MHD model and the numerical simulations which have been done will be presented in this section. The references listed above and herein should be consulted for a more detailed explanation of all the models concerning the RFP dynamo mechanism.

As mentioned in chapter 1, the nonlinear evolution of the $(m,n) = (1,1)$ mode is responsible for the tokamak sawtooth. A similar nonlinear interaction of the $m = 1$ mode is responsible for the RFP sawtooth. The underlying theory of this interaction will be presented here. Due to its similar nature, limited comparisons with the tokamak sawtooth theory will be made. Reference 21 should be consulted for a general description of the tokamak sawtooth.

The MHD equations have been fairly successful in explaining many features of the collective behavior of magnetically confined plasmas.

The effect of plasma perturbations (modes) in MHD theory is approximated by introducing perturbed quantities with a spatial structure of the form $f(r) = f_0 e^{i(k \cdot x)}$ where $k = \frac{m}{r} \hat{\theta} - \frac{n}{R} \hat{\phi}$ (m and n are the poloidal and toroidal wave numbers, respectively). These modes are said to be resonant where $\mathbf{k} \cdot \mathbf{B} = 0$. This corresponds to positions where q = m/n, q being the safety factor defined as $q(r) \equiv rB_\phi / RB_\theta$ for cylindrical geometry. At these positions, the modes have the same helical structure as the equilibrium magnetic field. Figure 2.4 shows a typical q profile for the RFP equilibrium as well as for the tokamak equilibrium for comparison. The RFP profile is a monotonically decreasing function of minor radius which reverses sign near the wall. The on-axis value, q(0) is aspect-ratio dependent; therefore it is device dependent, but typically has a value of 0.1 - 0.2. The edge value is device dependent as well, and it is also dependent on the depth of field reversal, $q_{edge} = r F / R\Theta$. On the other hand, the tokamak q profile is a monotonically increasing function of minor radius with an on-axis value near unity. The edge value, which is device dependent as well, is typically about 3.

Although certain q profiles of the type shown in figure 2.4 can be stable for certain RFP and tokamak equilibria,[22] perturbations can be driven unstable as a result of the plasma's evolution. As the center of the plasma is heated either ohmically or by external sources, the resistivity at the center decreases due to the inverse dependence of the resistivity on the temperature. This decrease in resistivity allows the current to diffuse radially inward causing the current profile to become

peaked on axis. This in turn causes the resistivity to decrease further due to the increased ohmic heating on axis thus peaking the profiles even more. As the profiles become peaked, the on-axis value of q decreases. The resulting profiles can become unstable to various types of plasma perturbations. The sawtooth phenomenon is characterized by this type of instability - the perturbation being the $m = 1$ tearing mode.

The $m = 1$ mode has been shown to be the fastest growing mode for both the RFP and the tokamak.[23] For the tokamak q profile, there is only one resonant $m = 1$ mode, $(m, n) = (1, 1)$, and only if $q(0)$ falls below unity. While the RFP has many $m = 1$ modes which could be resonant, $n \geq 5$ in the non-reversed region, and $n \leq -20$ in the reversed region. This is shown in figure 2.4 where the dotted horizontal lines represent values of q at which the $m = 1$ modes would be resonant. Due to their robust nature in linear MHD theory,[24] the $m = 1$ modes are prime candidates to be studied in the nonlinear regime.

In nonlinear MHD theory, the coupling of two $m = 1$ modes with helicities $(m, n) = (1, n_1)$ and $(1, n_2)$ can result in modes with helicities $(m, n) = (0, n_1 - n_1)$ and $(2, n_1 + n_1)$. The means by which these modes interact is currently a major theoretical investigation. A brief description

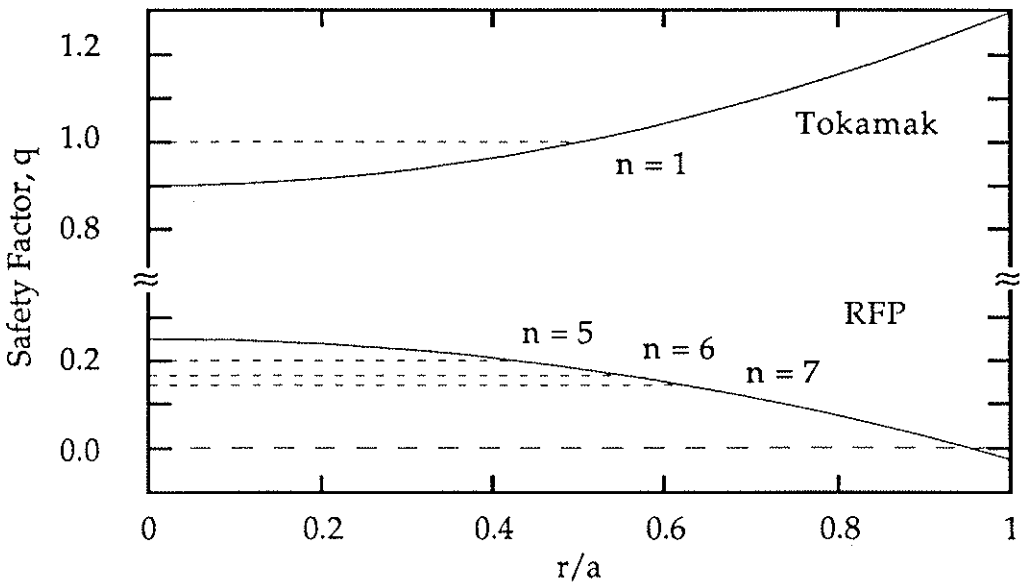

Figure 2.4 Comparison of the safety factor, q, profiles for the tokamak and the RFP. Horizontal lines indicate where the m = 1 helical modes would be resonant, q = 1/n.

of the results will be given here. The references listed herein should be consulted for a more detailed description.

The RFP sawtooth was predicted to exist as one of the results of a 2-D, single helicity, nonlinear MHD simulation by Caramana, Nebel and Schnack.[25] In this simulation, the nonlinear evolution of a single (m, n) = (1, n) mode was observed, the n being chosen such that it was resonant for the assumed q profile. During the simulation, the mode became unstable as the plasma evolved due to the ohmic heating. As the mode grew, it began to nonlinearly interact with itself and magnetic reconnection was observed. The reconnection process was actually a

double reconnection in which the first reconnection lowered the q(0) value, thus removing the resonance surface, but leaving the plasma in a deformed helical state. A second reconnection then occurred which raised the q(0) value bringing the resonance surface back into the plasma. However, a saturated m = 1 magnetic island remained, and the resulting profile was once again stable. Since this simulation was only single helicity, only modes with helicity $m'/n' = 1/n$ could be included. This eliminated all the secondary modes as well. Similar results were obtained for other single (1, n') modes which were resonant within the plasma, it was not a particular n that was responsible for the reconnection. When the mode was not resonant within the plasma, only the second reconnection was observed.

This result is very similar to the tokamak sawtooth which is a result of the (1, 1) mode becoming unstable when q(0) falls below unity.[21] When the perturbation enters the nonlinear regime, it experiences an accelerated growth, after which it reconnects resulting in $q(0) > 1$, stabilizing the plasma. But unlike the tokamak, there may be many m = 1 modes resonant in a RFP (as can be seen in figure 2.4). Therefore, to truly understand the RFP reconnection process, all helicities need to be included - all of the m = 1 modes and all of the secondary modes which could result from the nonlinear coupling process. This requires a full 3-D nonlinear MHD calculation.

This type of calculation has been performed by several groups.[26,27,28] The results are very similar to the 2-D simulation discussed above with

the m = 0 and m = 2 modes being generated by the interaction of the m = 1 modes. However, variances arise in determining which mode is responsible for the dynamo, the m = 1 or the m = 0. Simulations by Schnack, Caramana and Nebel,[26,29] and by Ho and Craddock[27] show that it is the m = 1 mode which is responsible for producing the reversed field. The m = 0 modes are necessary in order to have the reconnection of the m = 1 mode, but it is the m = 1 mode which drives the *dynamo electric field* which generates the reversed magnetic field. On the other hand, Kusano and Sato's 3-D simulations[28] show that it is the m = 0 modes which are responsible for generating the reversed field. The m = 1 mode is only the source of the m = 0. Likewise, the analytical work of Holmes, et al.[30] shows that it is the interaction between the m = 1 and the m = 0 which is the cause of the reversed field. Despite this variance, all the above simulations have been able to maintain the reversed field over the period of the simulation, typically a few hundred Alfven times ($\tau_A = a\sqrt{\mu_o \rho}$ / B where ρ is the plasma density).

Even though there is some variance regarding which mode is the one responsible for the dynamo, one simulation that is relevant to this thesis is an additional simulation performed by Kusano and Sato in which the simulation was carried out for a time much longer than the resistive diffusion time.[31] The results of this simulation are shown in figure 2.5. Repetitive sawteeth were produced in the reversal parameter and in the magnetic energy. This type of simulation was able to be accomplished with limited computer time due to the fact that the code was run at a low

aspect ratio, 1.6, and a low magnetic Reynolds number, $S \equiv \tau_R / \tau_A = 3 \times 10^3$. It is believed that the 3-D code of Schnack, Caramana, and Nebel would show the same repetitive nature if run for this amount of time as well.[32] As a result, the conclusion of this simulation - being able to reproduce repetive sawteeth - is not a solution to the variance, just an example.

For the Kusano and Sato simulation, an increase in the m = 1 energy correlated well with the decrease in F, the sawtooth crash. Also an increase in the m = 0 energy occurred after the m = 1 mode began to grow, see figure 2.5. Figure 2.5 also shows a simulation in which all the perturbed modes were discarded. This case does not show the sawtooth effect, and it experiences a loss of reversal. Hence, the perturbed modes are responsible for the sawteeth and for the maintenance of the reversal. A similiar result has been observed by Ho and Craddock[27] where the sawtooth structure was not seen in a simulation which suppressed the m = 0 mode and maintained the m = 1 modes. Unlike the results of Kusano and Sato, the field reversal was maintained.

Between sawtooth crashes, the plasma is undergoing resistive diffusion. It is this diffusion which is the driving force behind the sawtooth phenomena. This phase of the simulation is similar to a 1-D simulation performed by Werley, et al. for the sawteeth observed on the ZT-40M RFP at Los Alamos National Laboratory.[33] In this simulation, the rise-time of the sawtooth could be modeled without the inclusion of any dynamo term. The plasma was undergoing purely resistive

diffusion (this simulation will be described in more detail in chapter 5 where the same modeling has been applied to the MST sawtooth rise-time). Since the rise-time of the sawtooth is a resistive process (no dynamo present), the period of the sawteeth should increase as the resistivity is lowered, or as the magnetic Reynolds number is increased., $S \alpha 1/\eta$. This was shown to occur in the Kusano and Sato simulation where three separate cases were run with three different S values, see figure 2.6. Their results show that the period of the sawtooth increased with S.

In all of the 3-D simulations mentioned above, the center of the discharge becomes stochastic as the m = 1 modes begin to grow. As the m = 0 modes are created, the edge region becomes stochastic as well. This allows a rapid radial transport of the hot central plasma towards the edge. Consequently, the center of the discharge is rapidly *cooled*. This is the cause of the rapid crash in the central soft x-ray signal observed in the experiments. After the reconnection occurs, *good* flux surfaces reappear in the edge, improving the confinement, and allowing the center of the plasma to reheat. The 3-D MHD simulations cannot simulate the soft x-ray crash because the MHD equations do not treat the temperature of the plasma as an independent quantity - this would require a full 3-D transport code.

Also, all of the MHD simulations demonstrate that the reconnection process is more dramatic at higher values of Θ (deeper reversal). This is

due to the proximity of the reversal surface to the wall and the wall's stabilizing effects on the m = 0 modes. For a flux-conserving shell, the amplitude of the m = 0 island, which is resonant on the reversal surface, is limited by the amount of reversed flux that is between the reversal surface and the conducting wall. At high values of Θ, there is a greater amount of reversed flux. Consequently the m = 0 modes can grow larger in amplitude than they can in the lower Θ discharges, resulting in stronger sawtooth activity at high Θ.

As mentioned above, the two 3-D simulations (Caramana, Nebel and Schnack's, and Kusano and Sato's) have variances. These variances lie in which modes are primarily responsible for the dynamo - either the m = 1 or the m = 0. The study of the non-linear interactions of the helical modes is accessible to experiment and further theory, and progress is expected to occur rapidly. Experiments are already beginning to show the mode evolution during a sawtooth[34] and the nonlinear interaction of these modes. These results will be discussed in chapter 4.

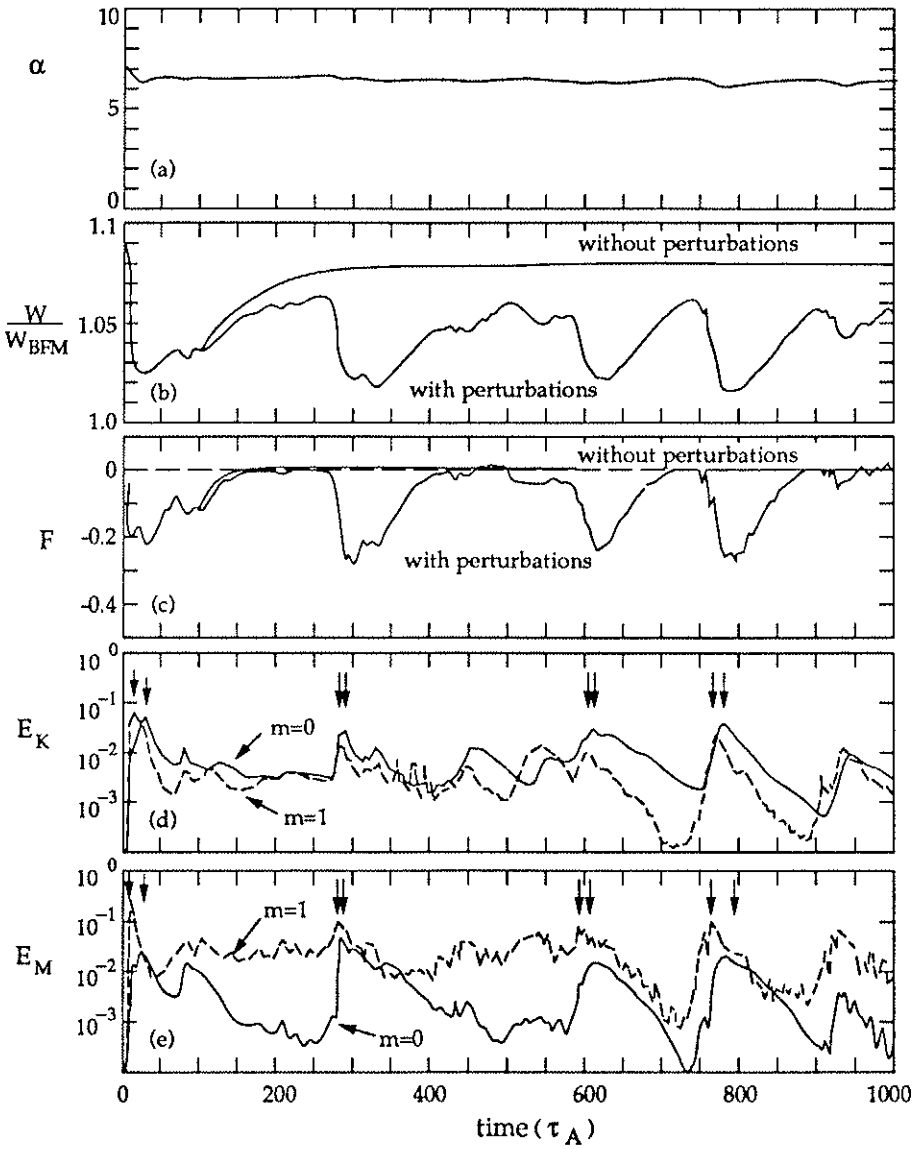

Figure 2.5 Time history of a) the total magnetic helicity, α, b) the normalized magnetic energy, W/W_{BFM}, c) the reversal parameter, F, and d) the kinetic, E_K, and e) the magnetic energy, E_M, of the perturbation modes (reproduced from Ref. 20).

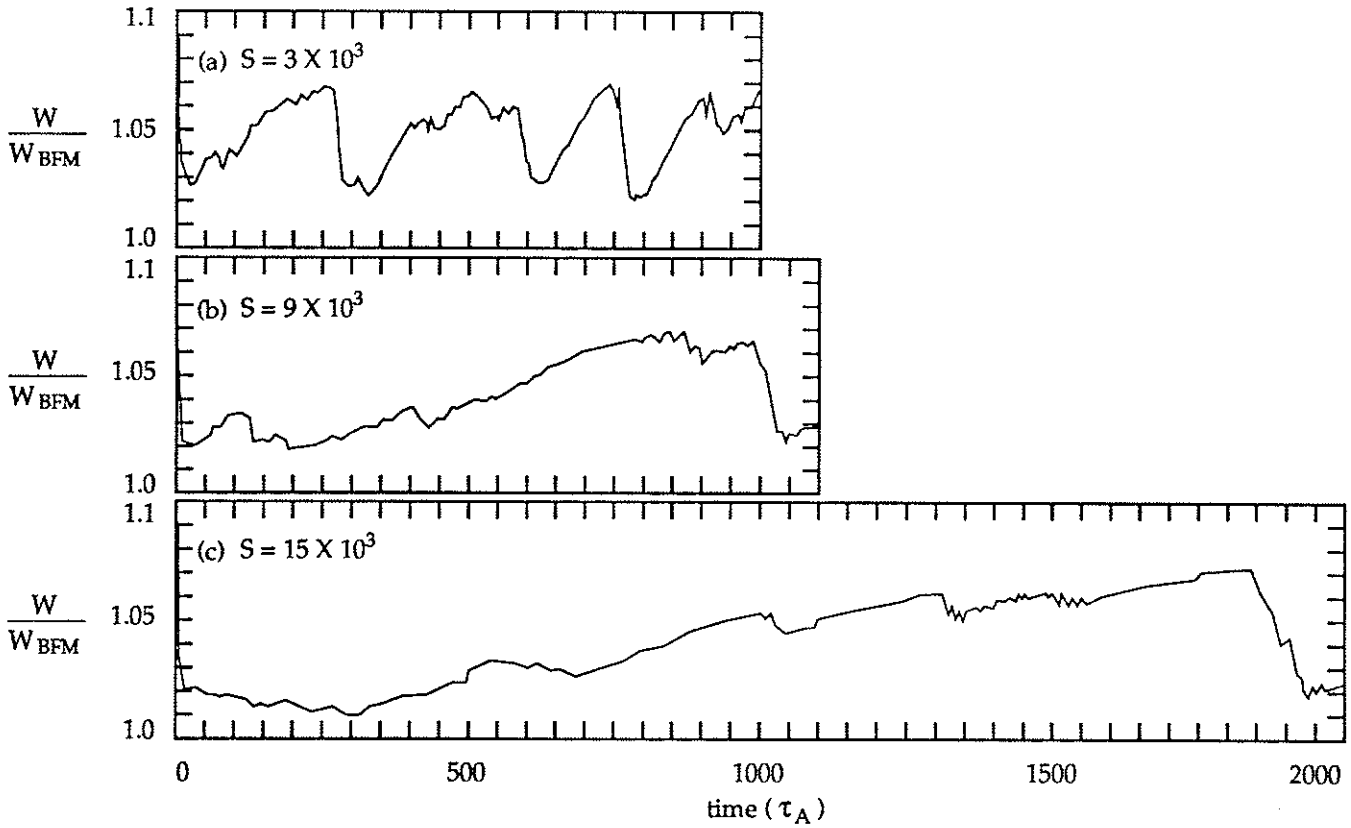

Figure 2.6 Time history of the normalized magnetic energy, W / W_{BFM}, for three different S values a) $S = 3 \times 10^3$, b) $S = 9 \times 10^3$ and c) $S = 1.5 \times 10^4$. (Ref. 20)

References

[1]J. B. Taylor, Rev. Mod. Physics, 58, 741 (1986).

[2]H. A. B. Bodin, Nucl. Instrum. and Methods, **207**, 1 (1983).

[3]H. A. B. Bodin, and A. A. Newton, Nucl. Fusion **20**, 1255 (1980).

[4]H. P. Furth, Nucl. Fusion **15**, 487 (1975).

[5]*Status of Tokamak Research*, ed. by J. M. Rawls (U.S. Dept. of Energy, Washington, D.C., 1979).

[6]original paper by J.B. Taylor, Phys. Rev. Lett. **33**, 1139 (1974). or

review paper by J.B. Taylor, Rev. Mod. Phys. **58**, 741 (1986).

[7]D. Brotherton-Ratcliffe, and I. H. Hutchinson, Culham Laboratory Report CLM-R246 (1984).

[8]J. C. Sprott, Phys. Fluids, **31**, 2266 (1988).

[9]T. G. Cowling, Mon. Not. Roy. Astr. Soc., **94**, 39 (1934).

[10]E. J. Caramana, and D. A. Baker, Nucl. Fusion **21**, 423 (1984).

[11]A. R. Jacobson, and R. W. Moses, Phys. Rev. A **29**, 3335 (1984).

[12]A. Sykes, and J. A. Wesson, in *Proceedings of the 8th European Conference on Controlled Fusion and Plasma Physics*, Prague (Czechoslovak Academy of Science, Prague, 1977), Vol. 1, p. 80.

[13]A. Y. Aydemir, and D. C. Barnes, Phys. Rev. Lett. **52**, 930 (1984).

[14]H. R. Strauss, Phys. Fluids **27**, 2580 (1984).

[15]A. Y. Aydemir, D. C. Barnes, E. J. Caramana, A. A. Mirin, R. A. Nebel, D. D. Schnack, and A. G. Sgro, Phys. Fluids **28**, 898 (1985).

[16]D. D. Schnack, E. J. Caramana, and R. A. Nebel, Phys. Fluids **28**, 321 (1985).

[17]A. Bhattacharjee, and E. Hameiri, Phys. Rev. Lett. **57**, 206 (1986).

[18]K. Kusano, and T. Sato, Nucl. Fusion **27**, 821 (1987).

[19]J. A. Holmes, B. A. Carreras, P. H. Diamond, and V. E. Lynch, Phys. Fluids **31**, 1166 (1988).

[20]K. Kusano, and T. Sato, submitted to Nucl. Fusion.

[21]see, for example, G. L. Jahns, M. Soler, B. V. Waddell, J. D. Callen, and H. R. Hicks, Nucl. Fusion **18**, 609 (1978).

[22]J. P. Friedberg, Rev. Mod. Phys. **54**, 801 (1982).

[23]see, for example, E. J. Caramana, R. A. Nebel, and D. D. Schnack, Phys. Fluids **26**, 1305 (1983) and references therein.

[24]*Ibid.*, pp. 1306-1307 and references therein.

[25]E. J. Caramana, R. A. Nebel, and D. D. Schnack, Phys. Fluids **26**, 1305 (1983).

[26]D. D. Schnack, E. J. Caramana, and R. A. Nebel, Phys. Fluids **28**, 321 (1985).

[27]Y. L. Ho, private communication.

[28]K. Kusano, and T. Sato, Nucl. Fusion **27**, 821 (1987).

[29]R. A. Nebel, E. J. Caramana, and D. D. Schnack, Phys. Fluids B **1**, 1671 (1989).

[30]J. A. Holmes, B. A. Carreras, P. H. Diamond, and V. E. Lynch, Phys. Fluids **31**, 1166 (1988).

[31]K. Kusano, and T. Sato, submitted to Nucl. Fusion.

[32]R. A. Nebel, private communication

[33]K. A. Werley, R. A. Nebel, and G. A. Wurden, Phys. Fluids **28**, 1450 (1985).

[34]K. Hattori, T. Shimada, Y. Hirano, Y. Yagi, and K. Ogawa, submitted to Phys. Rev. Lett.

CHAPTER 3

DESCRIPTION OF THE MST RFP

The Madison Symmetric Torus (MST) is a 52 cm minor radius, 150 cm major radius reversed-field pinch which began operation in June 1988. The experimental goal of the MST is to explore the boundary conditions of large RFPs in support of the next generation RFPs such as the ZT-H device at the Los Alamos National Laboratory,[1] and the RFX device in Italy.[2] This chapter will give a brief description of the MST RFP and of some of the diagnostics used for this thesis. For a more detailed description of the MST, see reference 3.

3.1 The MST Device

RFP devices throughout the world have shown an improvement in the plasma's performance with a reduction in the magnetic field errors.[4] One of the major design goals of the MST device was to minimize the external field errors. The MST is primarily a research device, consequently easy diagnostic access was also a design goal. To achieve these goals, the design incorporates some unconventional features for RFP devices. These features include a 5 cm thick aluminum torus, a poloidal field winding which is tightly wrapped around an iron core, and a pumping duct to avoid the magnetic field errors which would result from large pumping ports. Figures 3.1 and 3.2 show two views of the

MST and the relative positions of these unique features. Each of these feature will be described in more detail below.

The MST torus is made from 5 cm. thick aluminum (r = 0.52 m, and R = 1.50 m). It serves as the vacuum vessel, the toroidal field winding, and the stabilizing conducting shell. The latter two functions, and the requirement of low magnetic field errors, require that there be no large holes in the torus. The largest holes in the vacuum vessel are 4 - 11.4 cm diameter diagnostic ports. All other diagnostic ports are 5 cm in diameter or smaller. To reduce the field error due to large pumping ports, pumping of the vacuum vessel is done through 193 - 3.8 cm diameter holes which connect the torus to a pumping duct located at the bottom of the vessel. This feature retains the high pumping speed required to maintain a low base pressure, and eliminates the field errors due to larger pumping ports.

The vacuum vessel also serves as the conducting shell on the MST. A highly conductive shell near the plasma boundary is required for linear MHD stability[5] and for the existence of the "relaxed Taylor state" as described in chapter 2. Other RFP experiments use a separate conducting shell outside their vacuum vessel for this purpose. The MST uses the vacuum vessel as the conducting shell. This requires special gap protection to allow the magnetic fields to enter the vacuum vessel at both the poloidal gap, $\phi = 0°$, and the toroidal gap, $\theta = 180°$. The current

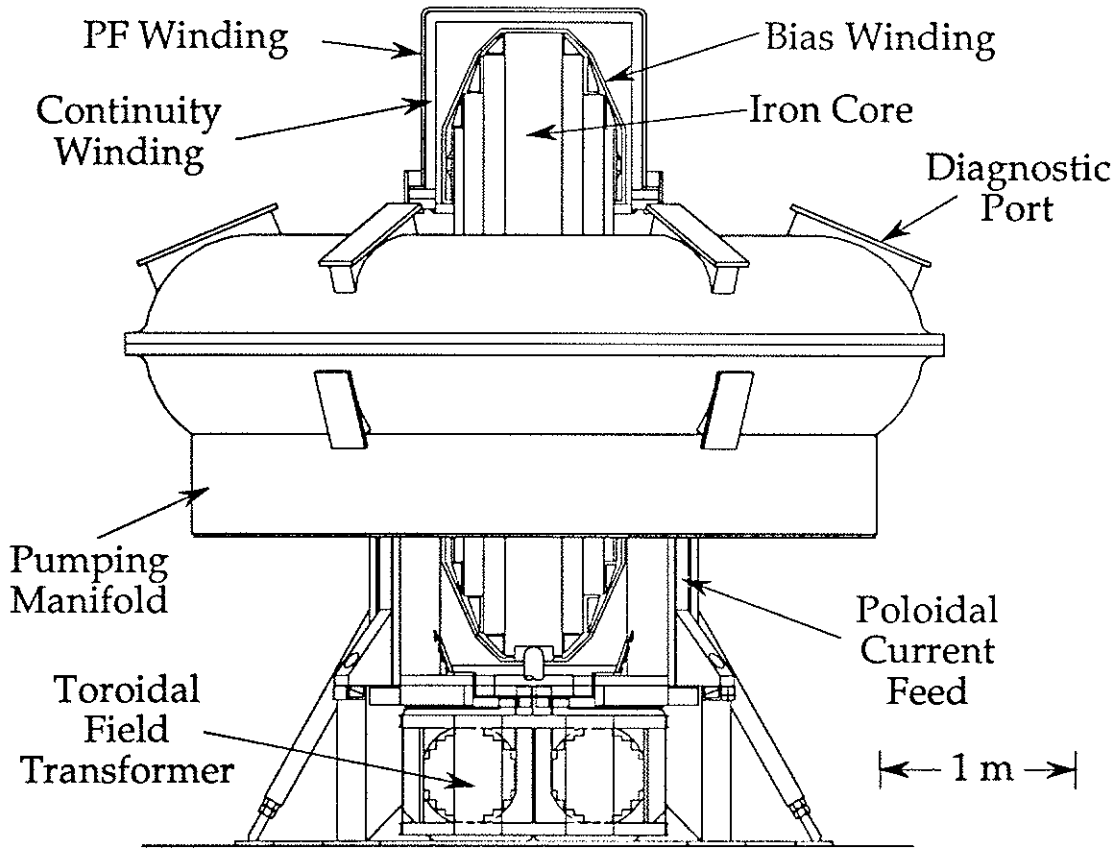

Figure 3.1 View of MST looking west.

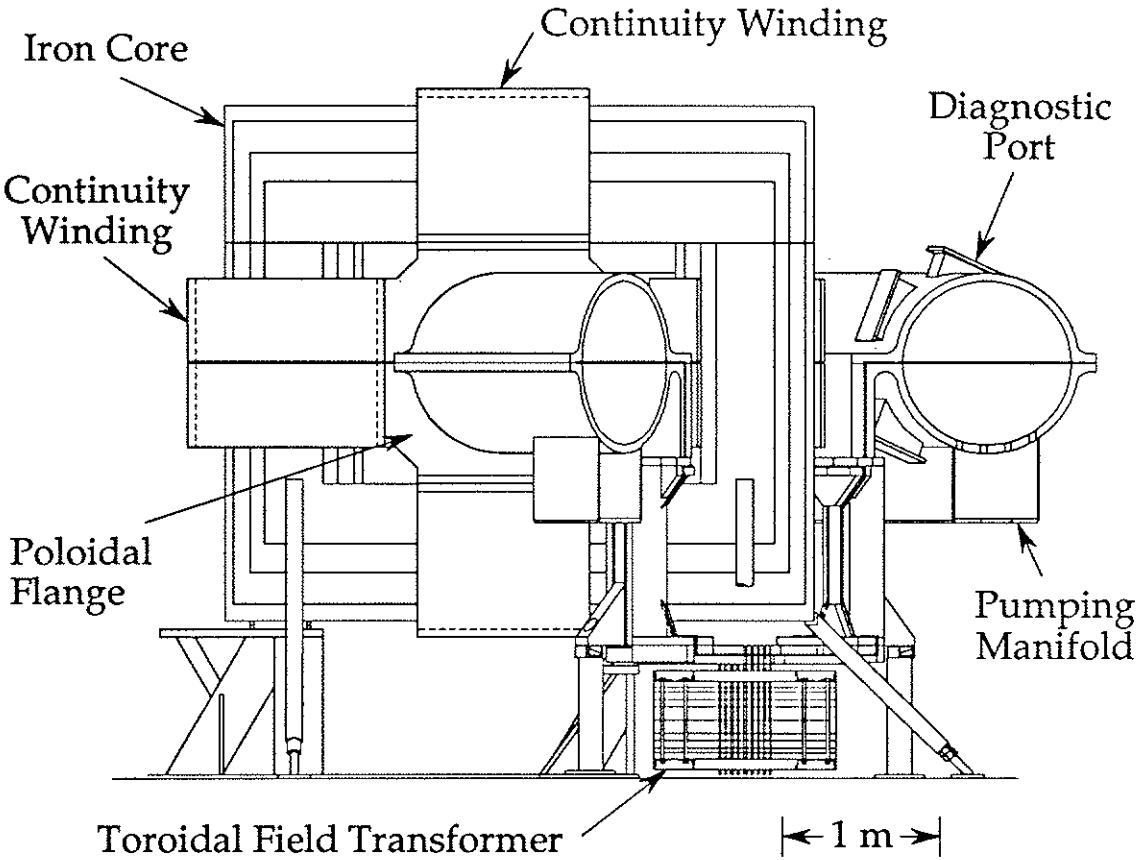

Figure 3.2 View of MST looking north.

scheme has been able to hold off several hundred volts across the poloidal gap during the startup of the discharge. The gap protectors also act as a limiter, extending ~1.25 cm into the plasma from the vacuum vessel wall.

Incorporation of the vacuum vessel in the toroidal field system is shown in figure 3.3. Poloidal currents are inductively driven through the vessel wall, thus creating a single turn toroidal field winding. This scheme reduces the toroidal magnetic field ripple which is produced by having discrete toroidal field windings. The radial field that enters the toroidal gap in vacuum produces a dominant $m = 0$, $n = 4$ Fourier component with a magnitude about 0.2% of the vacuum toroidal field on axis, $R = 1.50$ m.[6] The $n = 4$ is expected, as there are four current feed legs like those shown in Fig. 3.3 which link the vacuum vessel to the toroidal field transformer.

The poloidal field system for the MST is shown in figure 3.4. It consists of three sets of windings: a DC bias winding, a poloidal field winding and a *continuity winding*. The DC bias winding is used to reverse bias a 2 Volt-sec iron core with a DC current in order to get the maximum change in the poloidal flux thru the core during a discharge. It was placed tightly around the iron core, and it was positioned to minimize the DC magnetic field within the plasma region to less than one Gauss (this is less than 0.1% of the poloidal field). The poloidal field winding (the PF winding) is the main ohmic heating winding. It

was positioned to minimize the low-m magnetic field errors due to the discrete number of poloidal windings (40 total turns which are able to be connected in a variety of turn-ratios). It encircles the iron core, and it was placed as close to the plasma as possible at the poloidal gap in the vacuum vessel. The third winding is the continuity winding. This winding is required due to the nonaxisymmetry of the PF winding. The continuity winding is a sheet of aluminum which connects one side of the poloidal gap to the other side. It is attached to the vacuum vessel by a *poloidal flange*. This flange minimizes the field errors arising from design imperfections. All three windings are wrapped around the iron core, allowing easy diagnostic access to the vacuum vessel.

During the initial operation of the MST, the PF winding was not installed. The bias winding was used both as the DC biasing winding and as the pulsed ohmic heating winding. This resulted in large magnetic field errors at the poloidal gap.[6] These field errors were reduced by a modest correction scheme, but they still remained large (the root-mean-square (RMS) value of the radial field at the gap is 23 % of the equilibrium poloidal field at the wall). The PF winding was completed during the early part of 1990. The field errors at the poloidal gap were substantially reduced (RMS value of radial field at the gap is 5 % of the equilibrium poloidal field at the wall),[7] and an improvement in the plasma performance was also observed.[8] Further reduction of the remaining field errors is an ongoing effort.

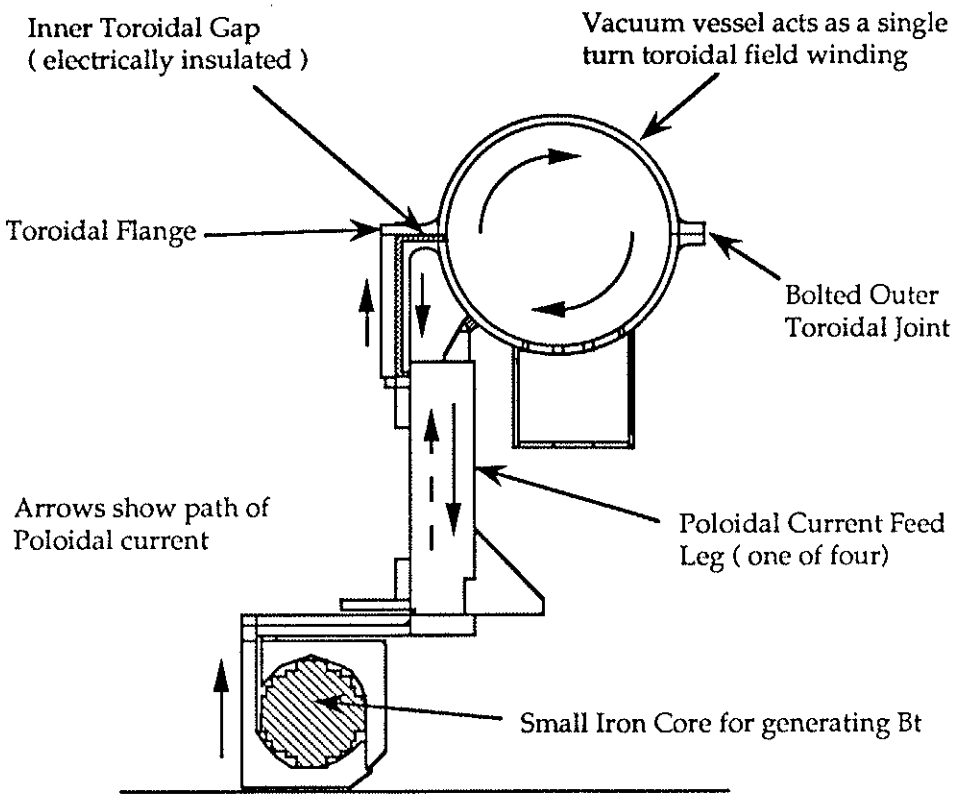

Figure 3.3: The toroidal field system of the MST device. The poloidal currents are driven through the vacuum vessel resulting in a single turn toroidal field winding.

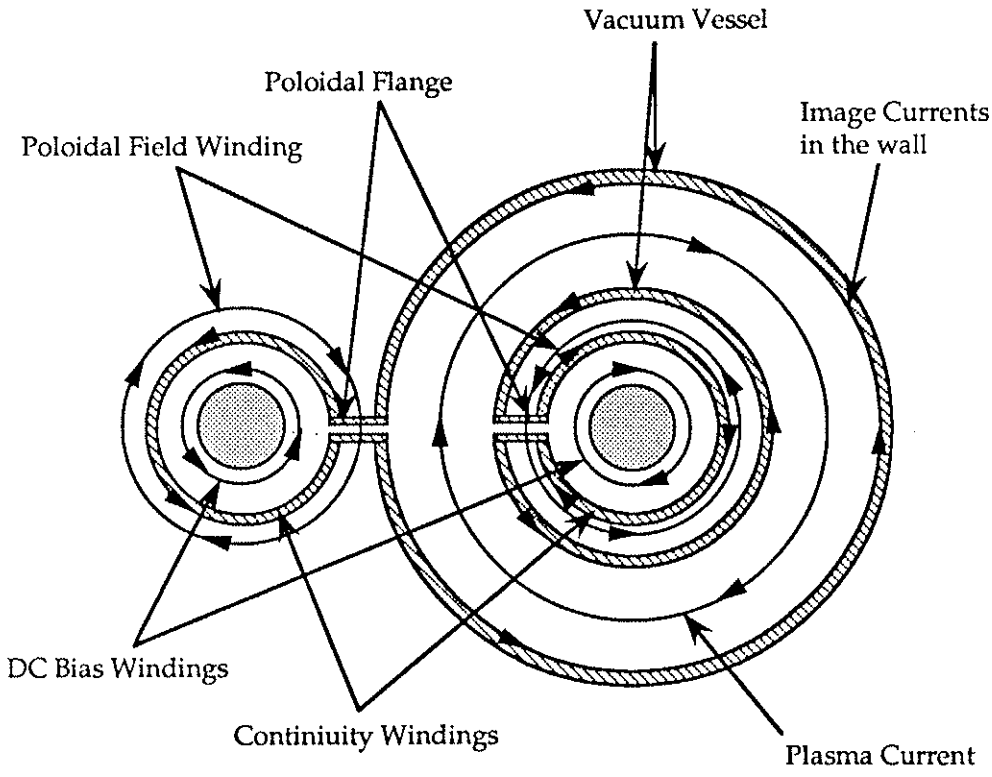

Figure 3.4: The poloidal field system on the MST device. During the initial operation, the DC bias winding was used as the pulsed ohmic heating winding as well as providing a DC biasing for core.

This thesis spans both operation stages of the MST (initial operation without the PF winding, and operation with the PF winding), the majority of the data being obtained during the initial operation.

3.2 Diagnostics on the MST device

Table 3.2 lists the diagnostics available on the MST which were used for this thesis. In the following sections, a few of these diagnostics will be described in more detail.

Table 3.2 Diagnostics available on the MST

Global plasma characteristics monitored by a variety of magnetic coils and electrical probes
Internal poloidal and toroidal magnetic pickup coil arrays measuring B_r, B_ϕ and B_θ at the wall
"Poloidal" soft x-ray array, and several toroidal, central chord, soft x-ray detectors
A swivel soft x-ray detector capable of viewing the central chord of the plasma out to the edge
Single point Thomson scattering measuring $T_e(r=0)$ and $n_e(r=0)$
Microwave interferometer measuring line averaged electron density

3.2.1 Global Operational Signals

The global operational signals on the MST are measured using a variety of Rogowskii loops, flux loops, and electrical probes.[9] Many of these are standard on any RFP device, but one worth mentioning for the MST is the toroidal field at the wall, $B_\phi(a)$. Since the vacuum vessel is used as the toroidal field winding, the $B_\phi(a)$ is related to the poloidal current in the vacuum vessel, I_θ : $B_\phi(a) = \frac{\mu_o I_\theta}{2\pi R}$. In order to remove the $1/R$ dependence, $B_\phi(a)$ is normalized to be equal to the average toroidal field, $< B_\phi >$, in vacuum resulting in $F \equiv \frac{B_\phi(a)}{< B_\phi >} = 1.0$ in vacuum. This measurement is a poloidally averaged value of the true $B_\phi(a,\theta)$, and agrees with internal measurements of the $B_\phi(a,\theta)$ by internal magnetic coils.

To obtain the global characteristics of the plasma, particularly the plasma resistance, the Polynomial Function Model (PFM) is used.[10] This model assumes the magnetic field and current profiles can be approximated by polynomial functions. Maxwell's equations are solved to obtain the magnetic profiles which match the global characteristics of the plasma, I_ϕ, $B_\phi(a)$, and $< B_\phi >$. This model predicts an F-Θ curve of the form $\Theta = (3 - F) \sqrt{\frac{2 - 2F}{9 - 6F}}$. This curve was plotted in figure 2.3 along with the BFM F-Θ curve and an experimental curve from the MST. The PFM curve is in reasonable agreement with the experimental curve. Once **J** and **B** are determined by the PFM, the plasma pressure can be determined from the equilibrium condition, $\nabla p = \mathbf{J} \times \mathbf{B}$.

The plasma resistance, R, can be determined from measurable quantities by the relation $V_{pg} = L\, dI_\phi/dt + AV_{tg} + R\, I_\phi$ where V_{pg} is the driving voltage across the poloidal gap, V_{tg} is the driving voltage across the toroidal gap. The variables L and A can be evaluated assuming PFM profiles and can be expressed as functions of Θ. The product $R\, I_\phi$ is called the loop voltage, V_{loop}, on the MST, and for a steady state plasma, $V_{pg} = V_{loop}$. This loop voltage will be used in chapter 4 to determine the plasma resistance, $R = V_{loop} / I_\phi$.

An alternate version of the PFM is the Modified Polynomial Function Model (MPFM).[11] This model uses the same techniques as the PFM, except it uses F and Θ as the independent variables where the PFM only uses Θ. The MPFM is used in this thesis to get a general idea of the shape of the internal profiles on MST.

3.2.2 Internal Magnetic Signals

In the past, the magnetic properties of RFP plasmas have often been measured by inserting movable magnetic pick-up coils into the plasma. Due to the high temperatures in the MST, probes could not be inserted past the edge of the plasma except for low current discharges, $I_\phi \approx 200$ kAmps. For this reason, the majority of magnetic signals used in this thesis were obtained from magnetic pick-up coils which are mounted inside the vacuum vessel wall. These coils will be describe in this section.

During the initial operation of the MST (no PF winding), an internal array of eight poloidally separated coil sets measuring B_ϕ, B_θ, and B_r, were mounted to the upper half of the vacuum vessel. The mounting scheme positions the coils 0.5 cm above the vacuum vessel wall. This array was completed during the installation of the PF winding, making a 16 coil poloidal array. Also at this time, a toroidal set of 64 coils and a second poloidal set of 8 coils were installed. Figure 3.5 shows the positioning of the two poloidal sets. The poloidal location of the toroidal set is also shown in figure 3.5.

The coil signals were either integrated to obtain the equilibrium magnetic field, or they were amplified and filtered in the 1-250 kHz range to obtain magnetic fluctuation measurements. Results of these measurements will be shown in chapter 4.

3.2.3 Soft X-ray Signals

Currently, the only way to *view* the interior of the plasma on the MST, other than single point Thomson scattering and a single chord microwave interferometer, is through the radiation emitted by the plasma. The soft x-ray radiation is a common diagnostic on hot plasma devices. On the MST, the soft x-ray radiation is measured by a "poloidal" array of surface barrier diodes (SBD). Thin beryllium filters are used in order to view the soft x-ray radiation in the 50 eV - 500 eV bandwidth. This array is described in this section, and is shown in figure 3.6a.

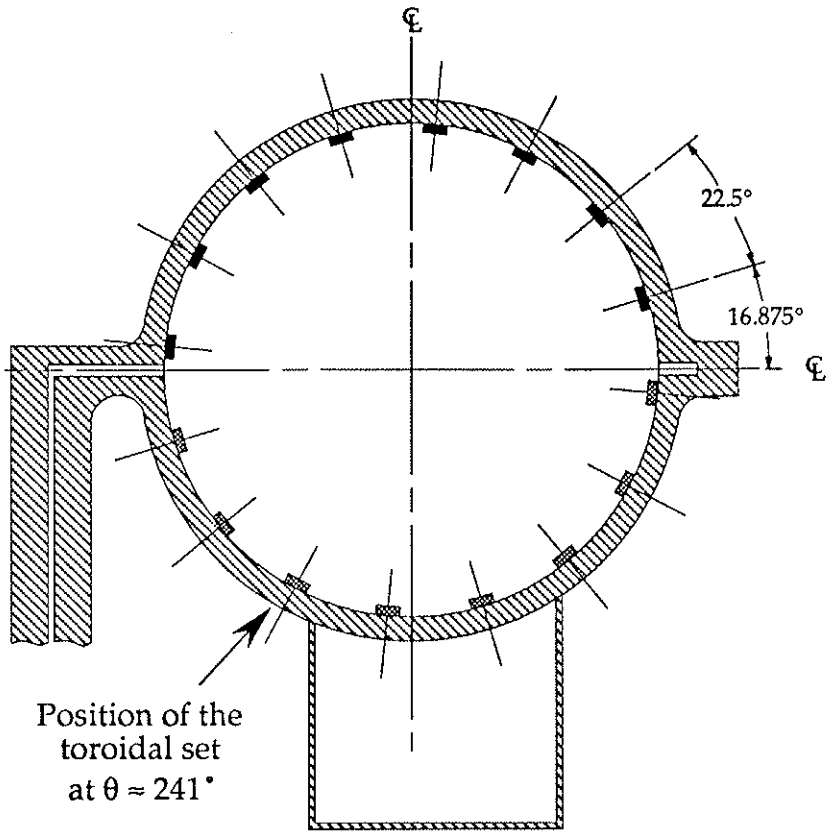

- coils used for the initial operation of the MST without PF windings

- coils added during the installation of the PF winding

Coils are not drawn to scale

Figure 3.5 : Arrangement of the internal magnetic pick-up coil arrays, two poloidal arrays located at $\phi \approx 180°$ and $\phi \approx 155°$. The toroidal array is positioned at $\theta \approx 241°$, and the coils are evenly spaced about the poloidal gap, $\phi = 0°$

The original experimental goal of the MST was to study the boundary effects of the RFP by operating with various conducting shells placed within the vacuum vessel; the size of these shells was to be 32 cm in radius. The soft x-ray detectors were positioned in order to give a full view out to this 32 cm radius (the dotted circle in figure 3.6). This makes tomographic inversions of the soft x-ray emission difficult since all of the detectors view the edge twice since they are chordal views. But there are no detectors which view only the edge. This makes it impossible to remove the edge contribution from the central chordal signals. To view the edge of the plasma during the initial operation of the MST, a swivel soft x-ray detector was installed. Figure 3.6 b shows the range of this swivel detector. Shot averaged profiles out to the plasma edge could be obtained using this swivel detector, and are shown in chapter 4. During the PF installation, the soft x-ray array was extended to include edge sampling of the 52 cm plasma. At the time of completion of this thesis, the additional detectors had not been installed; consequently no further edge information could be obtained from the "poloidal" array.

Later in chapter 4 references will be made to the "radial" soft x-ray array, this refers to the top 13 detectors of the "poloidal" array.

Also available during both operation periods were single SBD detectors. These detectors could be mounted at various positions around the vessel to toroidally sample the central chord plasma emission.

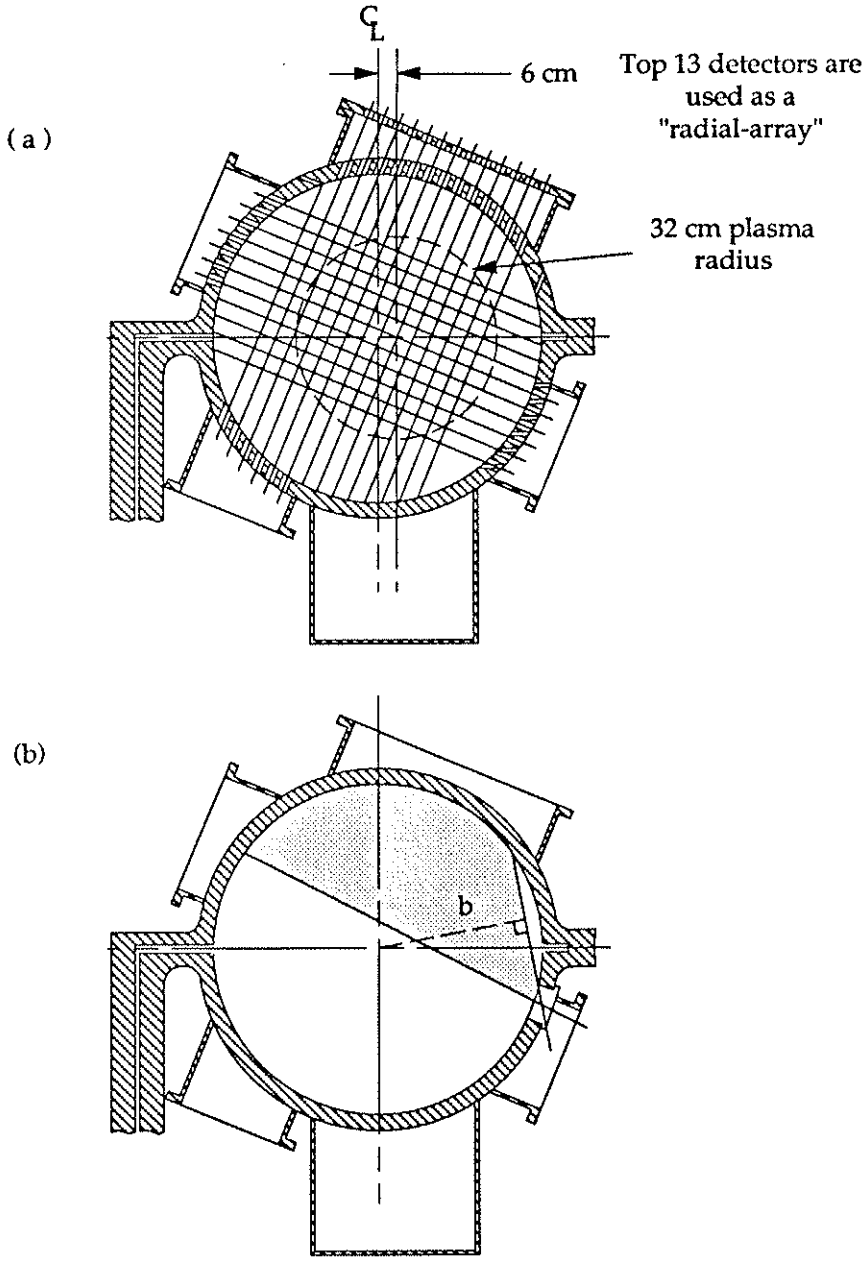

Figure 3.6 : Positions of various soft x-ray detectors on the MST, a) a poloidal array at $\phi \approx 160°$, and b) a swivel detector mounted at $\phi \approx 138°$.

3.3 Discharge characteristics

In this section, the global characteristics of the discharges on the MST will be described. The MST is still in a mode of optimization, so the discharge shown here is only a sample of the type of discharge that can be run on the MST. References 8 and 12 can be consulted for a complete description of the global characteristics of MST discharges.

A reversed discharge is shown in figure 3.7. This discharge occurred after the PF winding installation. The features of the RFP sawteeth can be seen in the total toroidal flux ($< B_\phi >$), and in the toroidal field at the wall ($B_\phi(a)$) signals: the $< B_\phi >$ increases, and at the same time $B_\phi(a)$ decreases (becomes more negative). Recall that for a reversed discharge, the toroidal field at the wall is in the opposite direction to the toroidal field on axis. For the total toroidal flux to increase while the toroidal field at the wall decreases, toroidal flux must have been created inside the reversal radius. This feature is the topic of this thesis, and it will be discussed in more detail in chapter 4.

Table 3.1 lists the parameters achieved on the MST. These parameters are the best in each category and do not represent a single discharge together. Substantial improvement has been achieved in many of these categories mainly due to the reduction of the field errors with the installation of the PF winding. As mentioned earlier, the MST is still in a period of optimization with the primary effort being further

reduction of the magnetic field errors, therefore continued improvement is expected.

Table 3.1 Operational Parameters Achieved on the the MST.

	Achieved (6/90)
Discharge duration	80 msec
Reversal duration	70 msec
Plasma current, I_ϕ	600 kAmps
V_{loop}	~ 15 V at 500 kAmps
Central electron temperature, $T_e(0)$	50 - 430 eV
Line-averaged electron density, $\langle n_e \rangle$	0.75 - 3 X 10^{19} m^{-3}
Particle confinement time, τ_e	$\leq$ 1.5 ms.

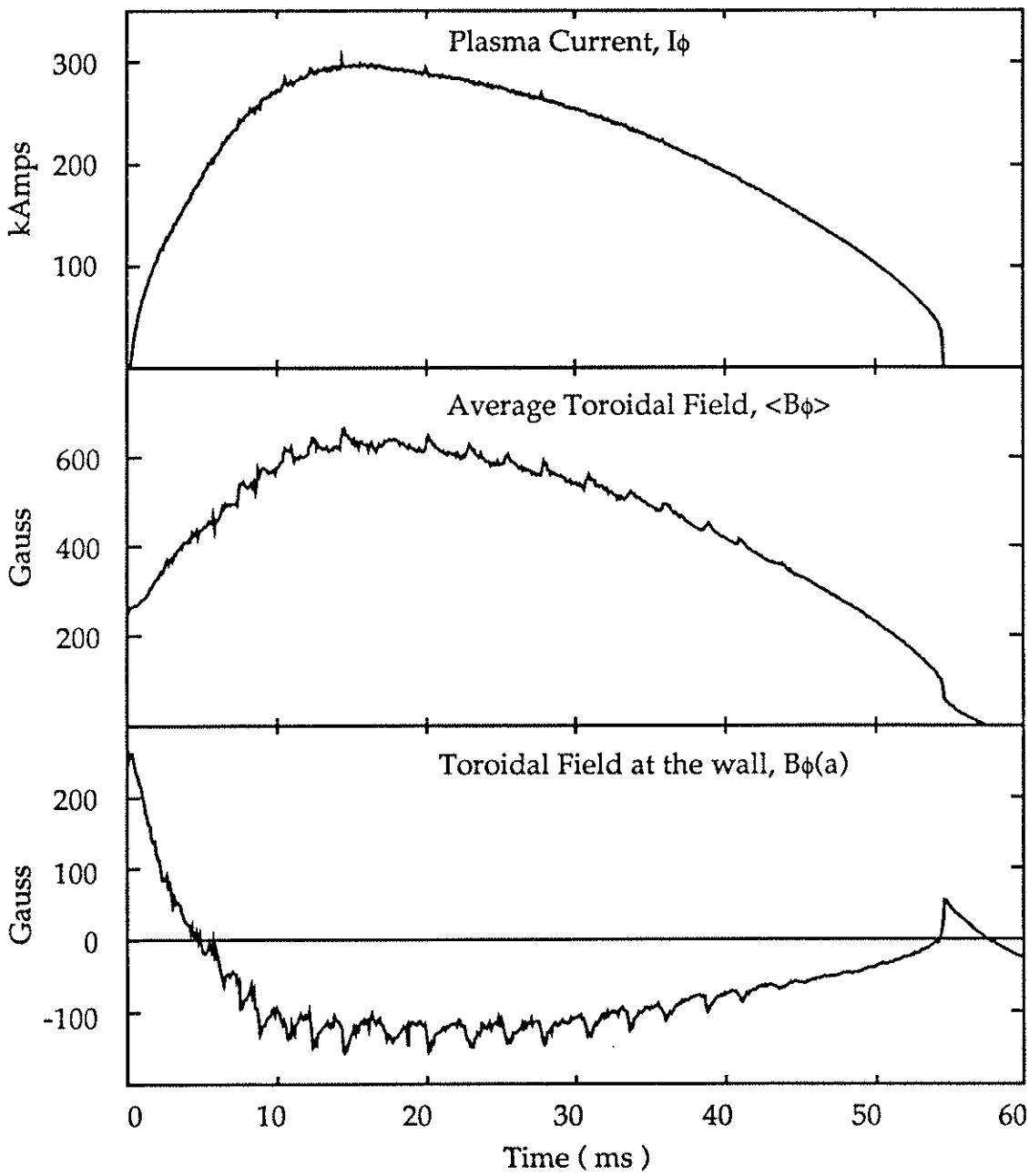

Figure 3.7: Time evolution of a reversed discharge on the MST.

References

[1]H. Dreicer, *International School of Plasma Physics, Physics of Mirrors, Reversed Field Pinches and Compact Tori*, Varenna, Vol. 1, 359 (1987).

[2]G. Malesani, *International School of Plasma Physics, Physics of Mirrors, Reversed Field Pinches and Compact Tori*, Varenna, Vol. 1, 331 (1987).

[3]R.N. Dexter, D.W. Kerst, T.W. Lovell, S.C. Prager, J.C. Sprott, "MST Technical Design Considerations," PLP 965, University of Wisconsin-Madison (1985); or

R.N. Dexter, D.W. Kerst, T.W. Lovell, S.C. Prager, J.C. Sprott, submitted to Fusion Technology, November, 1989.

[4]see for example: P. G. Noonan, H. Y. W. Tsui, and A. A. Newton, Plasma Phys. and Cont. Fus **27**, 1307 (1985); T. Shimada, Y. Hirano, Y. Yagi, A. A. Newton, K. Ogawa, in *Plasma Physics and Cont. Fusion Research, 1986*, Proc. of the 11th International Conf., Kyoto (IAEA, Vienna, 1987), Vol. 2, p 453; or R. S. Massey, C. J. Buchenauer, L. C. Burkhardt, A. R. Jacobson, J. G. Melton, G. Miller, R. W. Moses, K. F. Schoenberg, and R. W. Watt, Los Alamos National Laboratory Report LA-9567-MS (1983).

[5]D.C. Robinson, Nucl. Fusion **18**, 939 (1978).

[6]A. F. Almagri, S. C. Prager, and J. C. Sprott, Bull. Am. Phys. Soc. **34**, 2107 (1989).

[7]A. F. Almagri, private communication

[8]T. D. Rempel, A. F. Almagri, S. Assadi, J. A. Beckstead, R. N. Dexter, D. J. Den Hartog, G. Chartas, S. A. Hokin, T. W. Lovell, S. C. Prager, J. S. Sarff,

E. Scime, W. Shen, C. W. Spragins, J. C. Sprott, and F. Venneri, *Proc. of the IEEE Inter. Conf. on Plasma Science*, Oakland, CA, May 1990.

[9]J. C. Sprott, and E. Goetz, *"IBMPC MST Monitor System"*, University of Wisconsin-Madison, PLP 1039 (1988).

[10]J. C. Sprott, Phys. Fluids, **31**, 2266 (1988).

[11]J. C. Sprott, private communication.

[12]D. J. Den Hartog, Ph.D. thesis, University of Wisconsin-Madison (1989).

CHAPTER 4

EXPERIMENTAL RESULTS AND COMPARISONS WITH OTHER EXPERIMENTS

This chapter will describe the experimental observations on the RFP sawteeth. It will include results of this thesis as well as the results of studies performed on other RFPs. Comparisons will be made to show the general nature of the sawteeth as well as differences from device to device. The majority of the analysis has come from data taken during the initial operation of the MST (no PF winding). When there are differences between the sawteeth before and after the addition of the PF winding, these differences will be pointed out in detail. Additional comparisons will be made in chapter 5 where the results of a 1-D transport code simulation of the sawtooth rise-time will be presented.

The organization of this chapter is as follows. First, the general characteristics of the sawteeth are presented. Many of these are common on all RFPs that have observed sawteeth. A few peculiarities of the MST sawteeth will be presented in section 4.2 and will be more relevant to later discussion of the data analysis. Next, the profile modifications which occur during the sawtooth crash will be discussed - the sawtooth crash flattens the temperature, density and the current density profiles. In section 4.4, the toroidal nature of the sawtooth crash will be presented - the flux generation is initiated at one toroidal location and propagates around the torus. The evolution of the mode structure, the

precursor modes, will be presented in section 4.5 - initial results suggest that nonlinear interaction of the m = 1 modes is occurring. In the next two sections 4.6 and 4.7, the dependency of various plasma parameters on the Θ value and the plasma current will be presented. Finally, a brief summary of the experimental results will be given in section 4.8. This summary will be expanded upon in chapter 6 along with the conclusions from chapter 5.

4.1 General characteristics

A reversed discharge for the MST device is shown in figure 4.1. The sawtooth characteristics are quite evident in the toroidal field at the wall, $B_\phi(a)$, as well as in the average toroidal field, $\langle B_\phi \rangle$. For this discharge, the sawteeth occur throughout the discharge, and they appear to be the only source of reversal which is maintaining the field against the resistive diffusion. The $F - \Theta$ curve for this discharge is shown in figure 4.2. As mentioned in chapter 2, the experimental curve lies to the right of the BFM curve, and in this case to the right of the PFM curves as well.

An expanded view of a sawtooth is shown in figure 4.3. During the rise-time of the sawtooth ($t \approx 25.5$ ms to 27.5 ms), the plasma is moving further away from the "relaxed Taylor state" (the BFM curve) - this curve lies to the left in this figure. At the time of the sawtooth crash

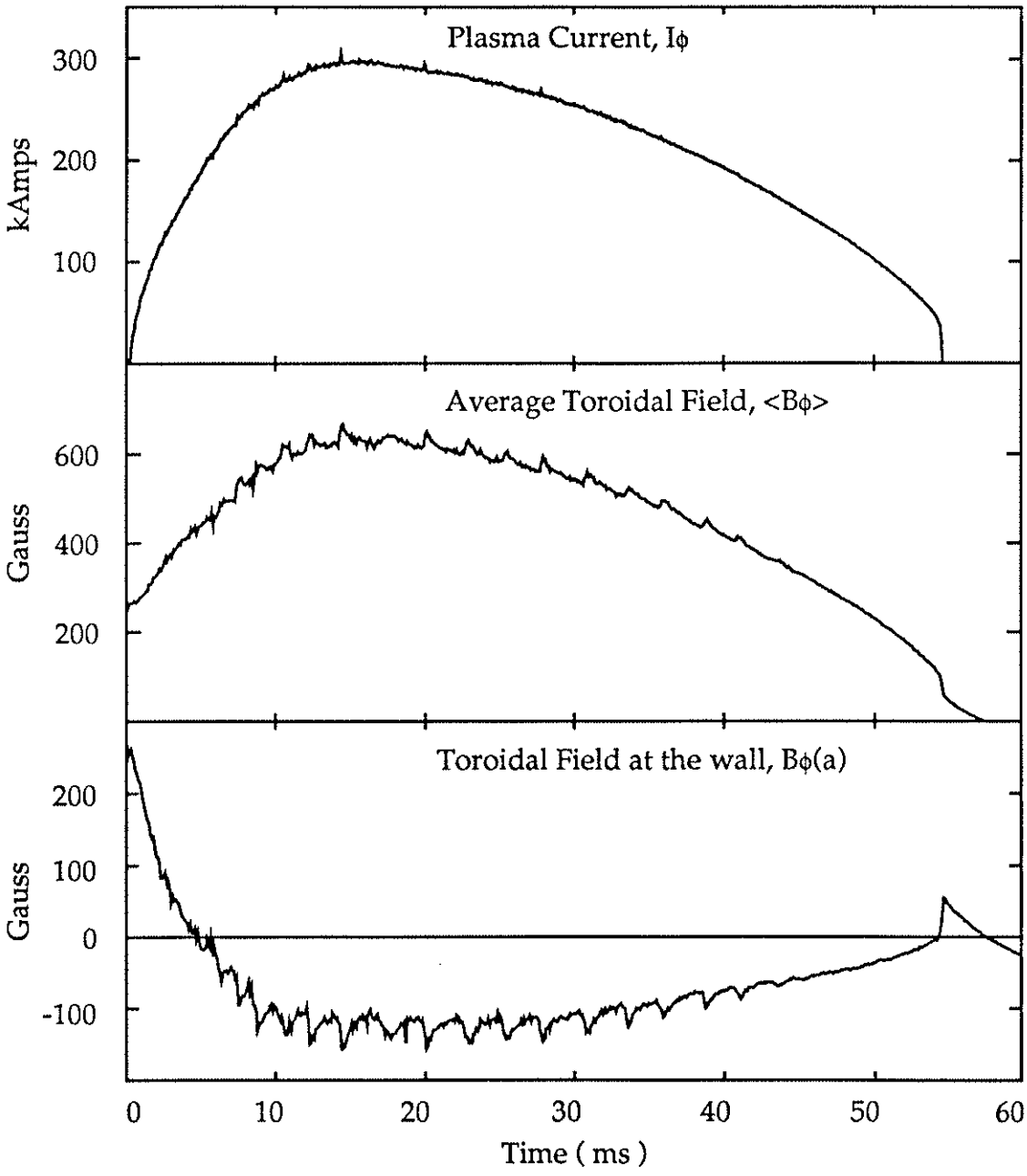

Figure 4.1: Time evolution of a reversed discharge in the MST.

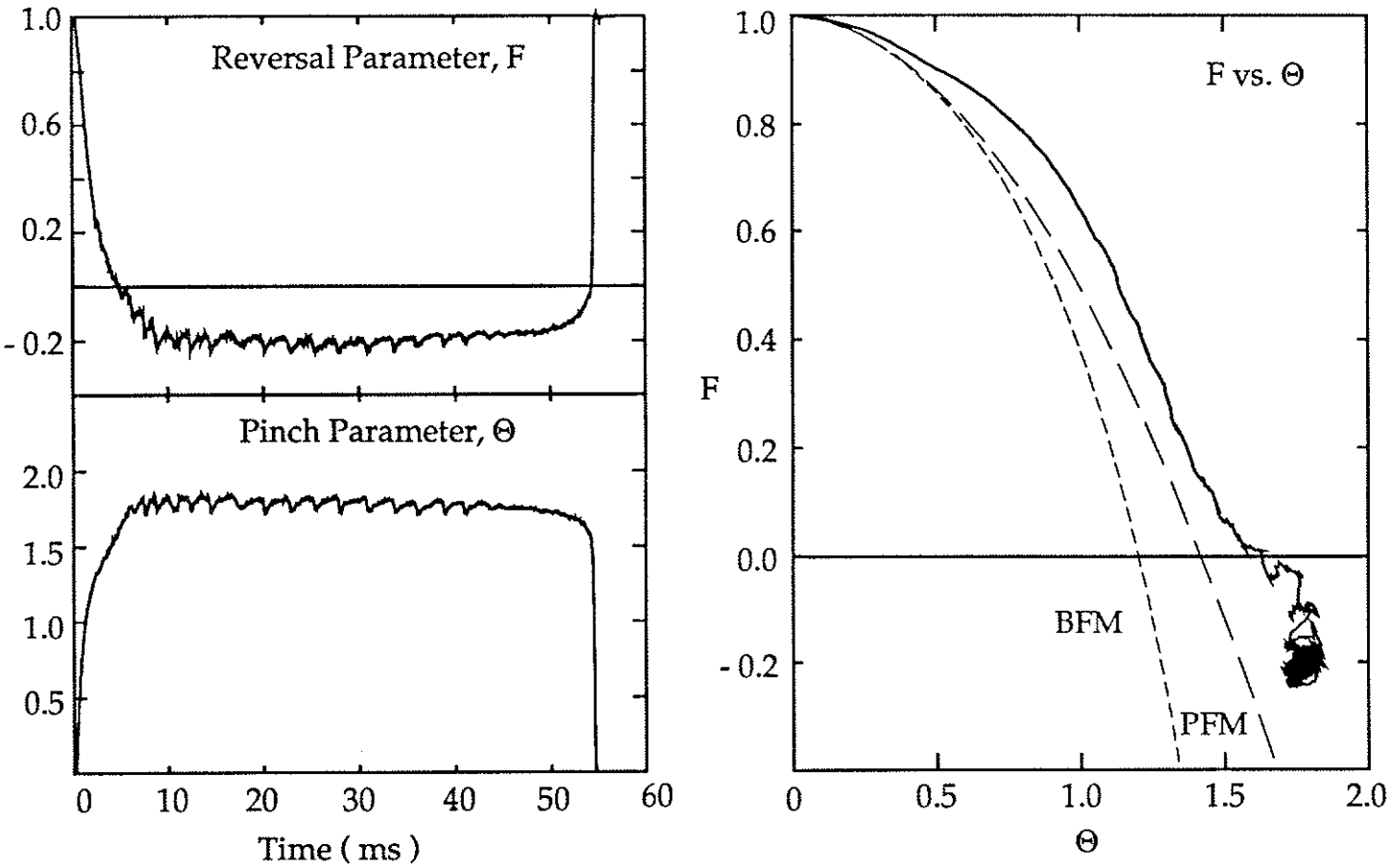

Figure 4.2 The F and Θ curves for the discharge shown in Fig. 4.1.

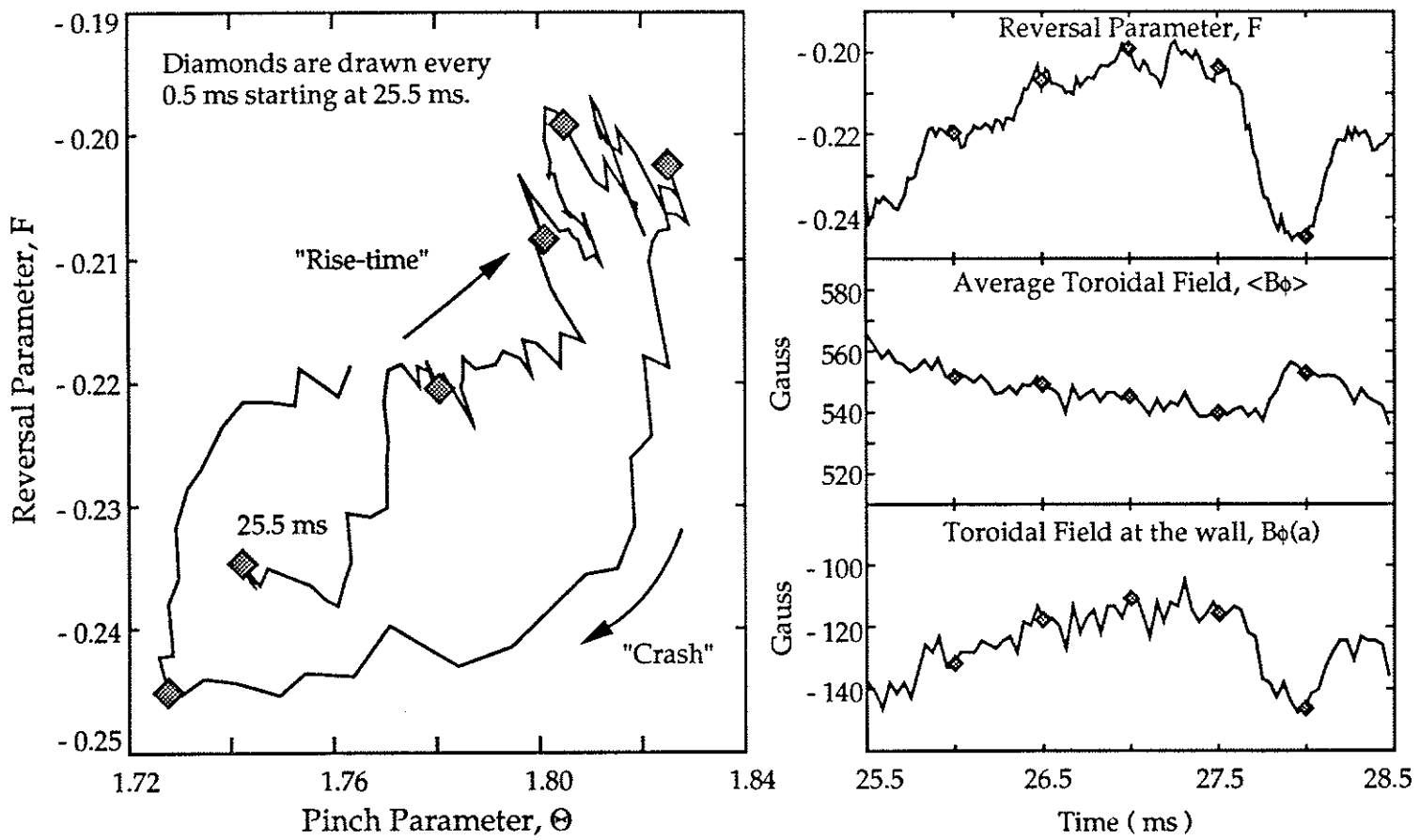

Figure 4.3 Expanded view of F - Θ curve shown in Fig. 4.2.

($t \approx 27.6$ ms), the plasma rapidly relaxes back towards the Taylor state. For the MST, the rise-time is ~ 1-5 msec, while the relaxation time is ~ 20-60 μsec. The variation of these two time intervals with other plasma parameters will discussed in more detail later in sections 4.6 and 4.7.

During a sawtooth crash, the total toroidal flux increases while the toroidal field at the wall decreases (becomes more negative). For a reversed discharge, the toroidal field at the wall is in the opposite direction to the axial toroidal field. As was described in section 2.1, the only way for positive toroidal flux to be introduced into the plasma externally is through the edge. This increases the toroidal field at the wall, rather than decreases it. On the other hand, if the reversal is driven deeper externally, the toroidal flux is decreased, not increased. In the case of the sawtooth crash, the additional toroidal flux must have been created internally. This *creation* of toroidal flux can be considered a discrete dynamo event.

Whether the dynamo is a discrete event in the case of the sawteeth or a continuous process, it must convert poloidal flux (which can be driven externally) into the toroidal flux needed to maintain the reversed state. This flux conversion occurs during a sawtooth crash. This is shown in figure 4.4 where the time rate of change of the poloidal flux as measured by a poloidal flux loop around the iron core, $V_\phi \propto \dot{\Phi}_\theta$, is plotted against the time rate of change of the toroidal flux as measured by a toroidal flux

loop inside the vacuum vessel, $V_\theta \alpha \dot{\Phi}_\phi$. This shows that the poloidal flux decreases and that the toroidal flux increases at the time of the sawtooth crash. A direct measurement of the flux conversion is not possible due to the difficulty in measuring the poloidal flux.

In many of the discharges on the MST, an increase in the plasma current, I_ϕ, is observed at the time of the sawtooth crash (see figure 4.1). This is believed to be primarily due to the way the plasma current is measured on the MST - the plasma current is typically derived from the primary current in the poloidal field system. The increase in this signal may be due to the strong coupling of the poloidal and the toroidal circuits. In many of the other RFPs, a decrease in the plasma current is correlated with a sawtooth crash.[1] The increase in the plasma current observed in the MST has little effect on the evolution of Θ during the sawtooth crash - the dominant change in Θ is due to the increase in the $<B_\phi>$ signal. Until a direct measurement of the plasma current is obtained, using internal Rogowskii loops, the increase in the plasma current will be passed over.

Between the sawtooth crashes, namely, the sawtooth rise-time, the overall field evolution is resistively diffusive in nature: the total flux is decaying while reversal is being lost, $B_\phi(a)$ is going towards zero. The resistive nature of the rise-time will be shown in more detail in chapter 5 where a 1-D transport simulation of the sawtooth rise-time will be described.

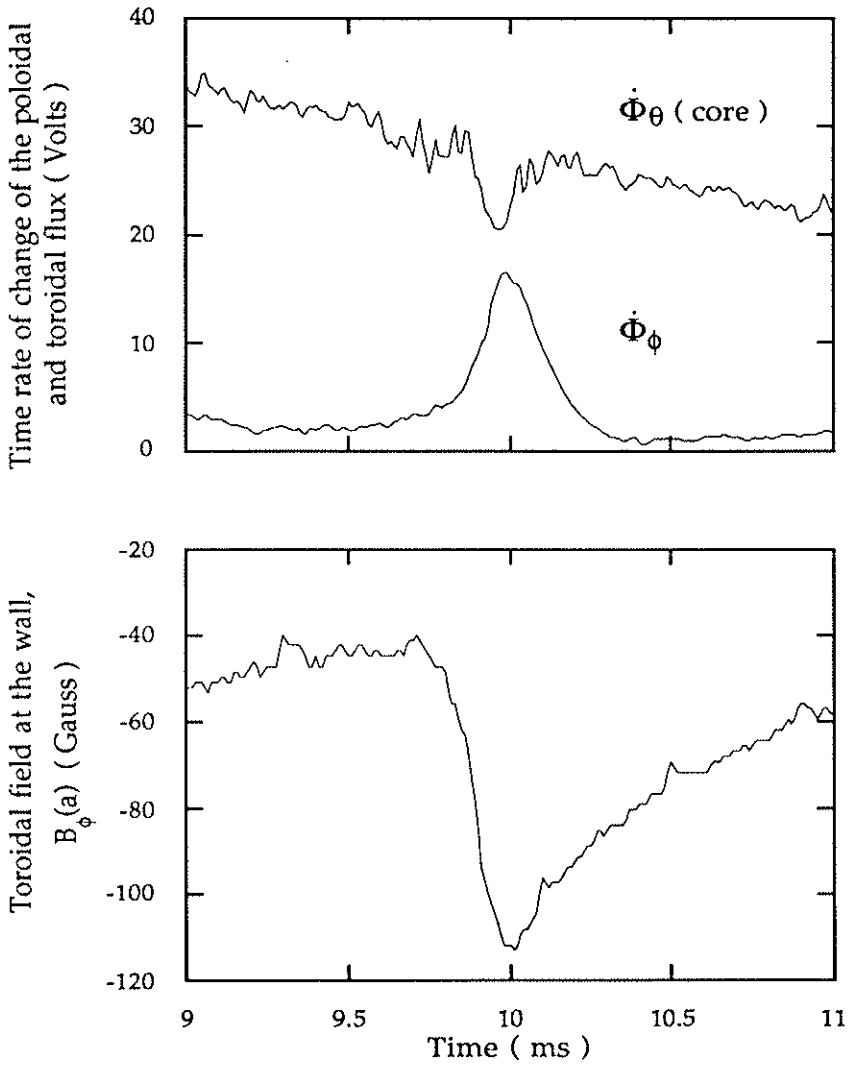

Figure 4.4 At the time of the sawtooth, the toroidal flux increases while the poloidal flux decreases.

During the rise-time of the sawtooth, low frequency (10-25 kHz) m = 1 oscillations are observed on edge magnetic signals as well as soft x-ray signals; see figure 4.5. (In this figure, the soft x-ray emission has begun to decrease before the *flux jump* occurs, $t \approx 11.4$ ms. This will be

discussed in more detail in section 4.2.) The magnetic and soft x-ray perturbations have a toroidal mode number, | n |, in the range of 5 to 8, and they are internally resonant. Their role in the RFP sawtooth is reminiscent of the m = 1 modes observed prior to the tokamak sawtooth crash. For this reason, the term *precursor* will be used to describe the m = 1 perturbations throughout this thesis. The helical structure of these precursor modes is consistent with resistive MHD simulations which predict $|\frac{n}{m}| \approx 2\frac{R}{a}$ (~ 6 for the MST) to be the dominant resistive instability in the RFP.[2] It is also consistent with the helicities observed on other RFP devices. For example, the ZT-40M RFP observes precursors with | n | in the range 10-15.[3] The aspect ratio of ZT-40M is 5.7.

In the 3-D simulations of Kusano and Sato[4] discussed in section 2.2, the sawtooth activity was stronger for simulations with a smaller aspect ratio. This is presumably due to the spacing of the m = 1 modes. These modes will be resonant at radial positions where $q = \frac{1}{n}$. For a low aspect ratio device such as MST ($\frac{R}{a} \approx 3$), these positions will be widely separated. The m = 1 modes can grow to a larger amplitude before they begin to interact. For a larger aspect ratio device such as ZT-40M ($\frac{R}{a} \approx 5.7$), the m = 1 modes would interact more frequently thus producing a more continuous-like dynamo. This is one possible reason for why the sawteeth are so prevalent on the MST device, and only present during high Θ operation on other devices such as ZT-40M.

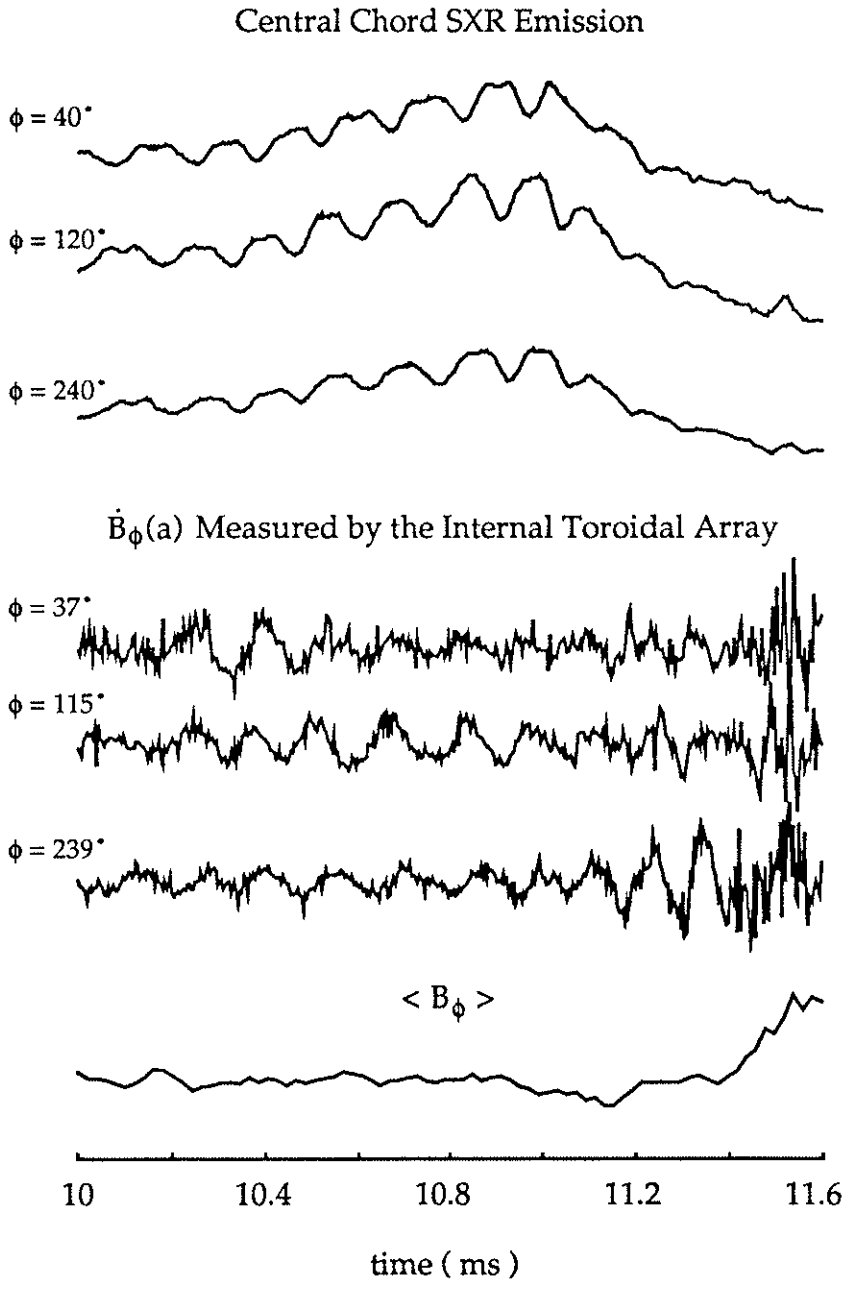

Figure 4.5: Low frequency oscillations are observed on edge magnetic signals, as well as soft x-ray signals.

The evolution of the precursor modes and their nonlinear coupling during a sawtooth crash will be described later in section 4.5.

An interesting feature of these precursors is that they are observed in the magnetic and soft x-ray diagnostics, but they are not evident in any of the line radiation diagnostics. This would suggest that although they are a perturbation in the current density and the plasma temperature, they have little effect on the plasma density. At the plasma edge temperatures of the MST (10s of eV), the line radiation is essentially independent of the variations in the plasma temperature, $I_{line} \alpha n_{ion} n_e \sigma(Te)$ where $\sigma(Te)$ is proportional to the excitation rate. The majority of the radiation comes from the outer portions of the discharge. The precursors are seen beyond $r = 0.6a$ in the soft x-ray signals; at $r = 0.6a$, there is significant impurity radiation, but no evidence of the precursors.

The general characteristics shown in figures 4.1 to 4.3 are common on all of the RFPs that have observed sawteeth. In many of these devices, sawteeth are not observed except during high Θ operation, $\Theta > 1.6$, although there is some speculation that a similar event is occurring at lower Θ.[5] In the MST, sawteeth are observed at nearly all values of Θ, even in nonreversed discharges, as illustrated in figure 4.6. The nonreversed sawteeth have the same phasing as the sawteeth observed in reversed discharges, $<B_\phi>$ increases and $B_\phi(a)$ decreases, and the $m = 1$ precursors are often observed. But the nonreversed sawteeth tend to be more rounded in character. At this point, it is unclear whether the same

phenomenon is driving the nonreversed sawteeth and the reversed sawteeth, namely the nonlinear interaction of the m = 1 tearing modes. However, sawteeth-like oscillations have been observed in the Reversatron II when operated as an ultra-low q device,[6] that is, a pinch formed without reversing the toroidal field. A similar theory to that published for the RFP[7] has been developed for the reconnection in ultra-low q discharges.[8]

The MST device tends to operate at a higher value of Θ for a given F value than do other RFPs - reversal usually occurs at $\Theta \approx 1.4 - 1.5$ for the MST. The reason for this is not known at this time. An error of ~ 5% in Θ can be accounted for owing to the measurements of the plasma current and the toroidal flux, but this is not large enough to account for the high Θ's observed. The *high* Θ operation of the MST may be a cause of the sawteeth being so prevalent in the MST device - other possibilities will be discussed throughout this chapter and in chapter 5.

While the MST does operate at a higher value of Θ, in general, the F-Θ curve will vary between various RFP devices. This is mainly due to variations in the plasma profiles from one device to another. For this reason, many of the plots in this thesis will rely on the value of Θ and comparisons will be made with other RFPs. These comparisons should only be viewed as a trend with Θ, and no direct comparison should be made at a given Θ value.

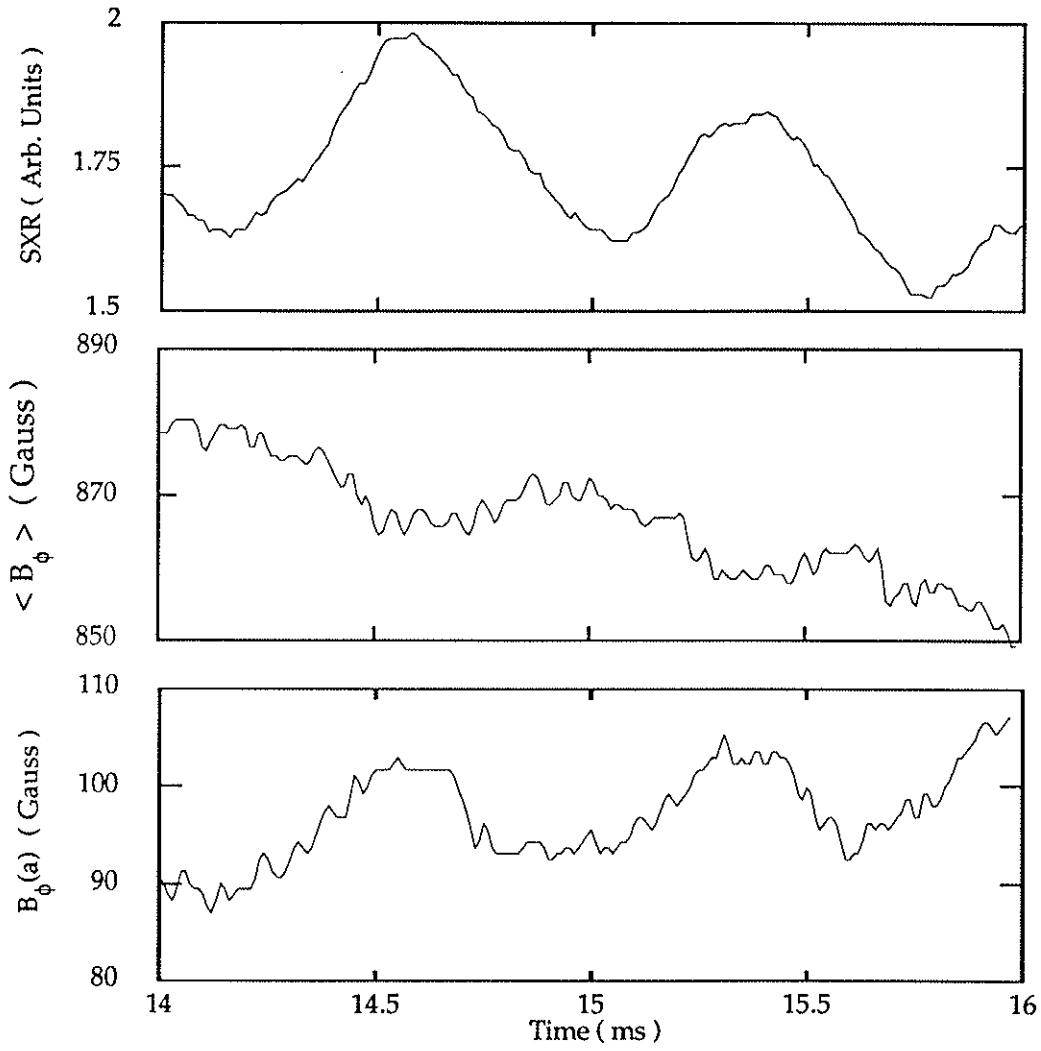

Figure 4.6 Sawteeth are also observed in nonreversed discharges.

4.2 Sawtooth peculiarities observed on the MST.

At this point a few peculiarities of the sawteeth observed on the MST will be presented. The impact of these features will be pointed out in the following sections. Many of these features have either a limited

explanation or no explanation at this time and are only presented here to simplify the explanation of experimental results which will be presented later in this chapter.

Even though the sawteeth are a dominant feature of many of the MST discharges, they have not always been present. During the initial operation of the device and the operation immediately following the completion of the PF winding, sawteeth were not present. As the vacuum vessel was cleaned, the loop voltage decreased. With these improved discharge characteristics, the sawteeth appeared. This is possibly due to the decrease in central resistivity allowing the current to diffuse radially inward - peaking the current profiles. This effect has also been reported for the HBTX1B.[9]

In many of the discharges, the *phase* between the soft x-ray decay and the *flux jump*, represented here by the decrease in $B_\phi(a)$, varies during the discharge; see figure 4.7. The soft x-ray emissivity has already begun to decrease before the toroidal flux is created, and in a few cases the flux jump occurs near the bottom of the soft x-ray oscillation, for example the flux jump that occurs at $t \approx 16$ ms in figure 4.7. Late in the discharge, the top portion of the soft x-ray emissivity is oscillatory in nature, and it has a $m = 0$, $n = 0$ structure. At the time of the *flux jump*, the soft x-ray emission drops suddenly independent of the phase of the oscillation as is the case for the earlier sawteeth. The reason for this phase difference is unknown - possibilities include a beating of the plasma column (either

temperature or density related), or the center of the plasma beginning to cool as the m = 1 perturbations grow.

Despite the rolling over of the soft x-ray emission, a burst is observed in the soft x-ray emission concurrent with the flux-jump; see figure 4.7. A simultaneous burst is observed in the hard x-ray emission. This burst could be due to a high energy electron component being lost to the wall generating high energy x-rays. At this time, no energy spectrum of the x-ray emission is available for the MST device. Initial results of soft x-ray tomography have concluded that the volume-averaged soft x-ray emission increases during this burst, but due to the limited radial extent of the soft x-ray array, it is unclear if the increase in the emission is due to the edge or to the center of the discharge.

In some of the discharges, the sawteeth appear to be present only during the rising current portion of the discharge. This is possibly due to the large, axial electric field which is present during this phase of the discharge. As a result, the current profiles may become peaked on axis causing the m = 1 modes to become unstable. The increase in the sawtooth activity during ramped current discharges has been shown on ZT-40M[10] and TPE-1RM15[11] where the plasma current is increased once an initial value has been achieved. An increase in the sawtooth activity is observed during these ramped current discharges. On the MST, a flatter plasma current trace can now be maintained for a longer portion of the discharge. This is due to the improved toroidal field programming and the lower loop voltages achieved since the

completion of the PF winding. This eliminates the large, driving electric field, but the sawteeth are still present in many of the discharges even with a flat current trace.

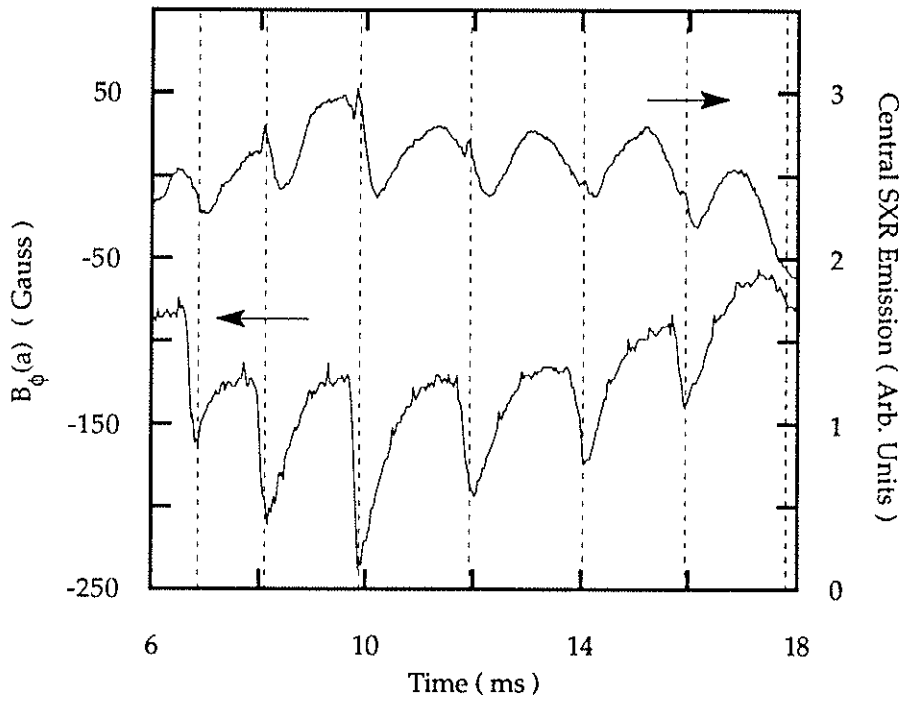

Figure 4.7 The phasing of the soft x-ray decrease and the flux jump varies during a reversed discharge. The vertical lines are times at which the flux jump occurs - this is determined by the maximum in the $\dot{\Phi}_\phi$ signal.

The opposite effect occurs during *ramped down* discharges. In the TPE-1RM15 RFP,[11] the sawtooth activity is decreased during discharges where the plasma current is slowly decreased from an initial value. This type of discharge usually exists in the MST for high plasma current

levels, $I_\phi > 300$ kAmps. This is due to the limits of the existing poloidal field circuitry. In this type of discharge, sawteeth are small - if present at all - after the peak current; see figure 4.8. The arrows indicate times where a flux jump has occurred as determined by a positive spike in the $\dot{\Phi}_\theta$ signal. The increase in the average toroidal field is observed, but is at a reduced level compared to the sawteeth which occur during the ramp-up portion of the discharge.

4.3 Profile modifications

At the time of the sawtooth crash, the central soft x-ray emission decreases while an increase is observed on various edge diagnostics; see figure 4.9. These trends suggest a decrease in the central plasma properties such as the density and the temperature, and an increase in the edge properties. This section will describe several experimental observations of the profile changes that occur during the sawtooth crash. In the MST, very few profiles are able to be measured due to the limited number of diagnostics; thus many of the profile changes are implied from experimental observations rather than measured. Profiles measured by other RFPs will be presented to support the observations on MST.

One of the few profiles measured on the MST is the soft x-ray emission profile. The "poloidal" array described in chapter 2 can be used to "view" the center of the discharge. Using the top 13 detectors of this array as a "radial" array, the soft x-ray profile decreases during a sawtooth

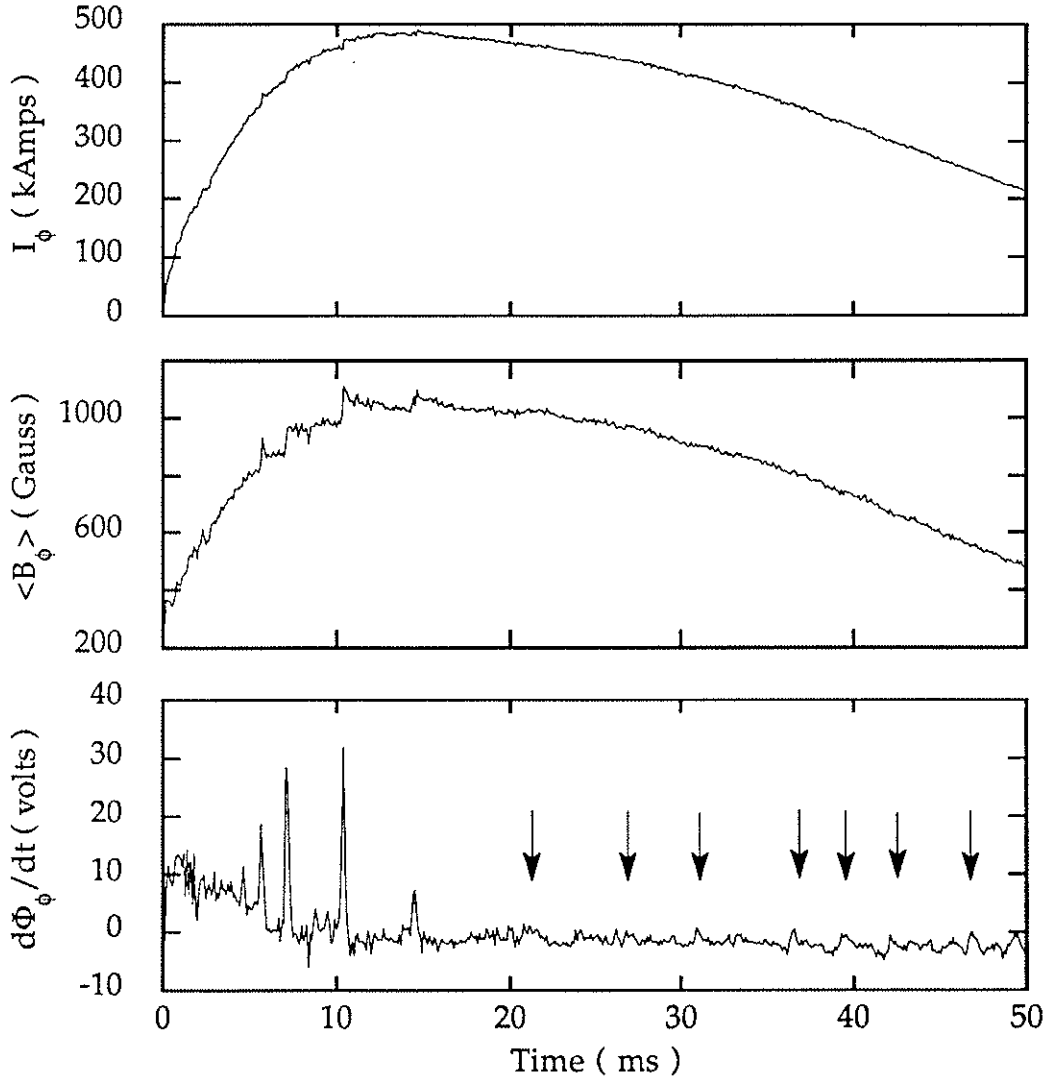

Figure 4.8 In high current discharges, the sawteeth occur after the peak current, but at a reduced level. The arrows mark times where sawteeth occur as determined by spikes in the $\dot{\Phi}_\theta$ signal.

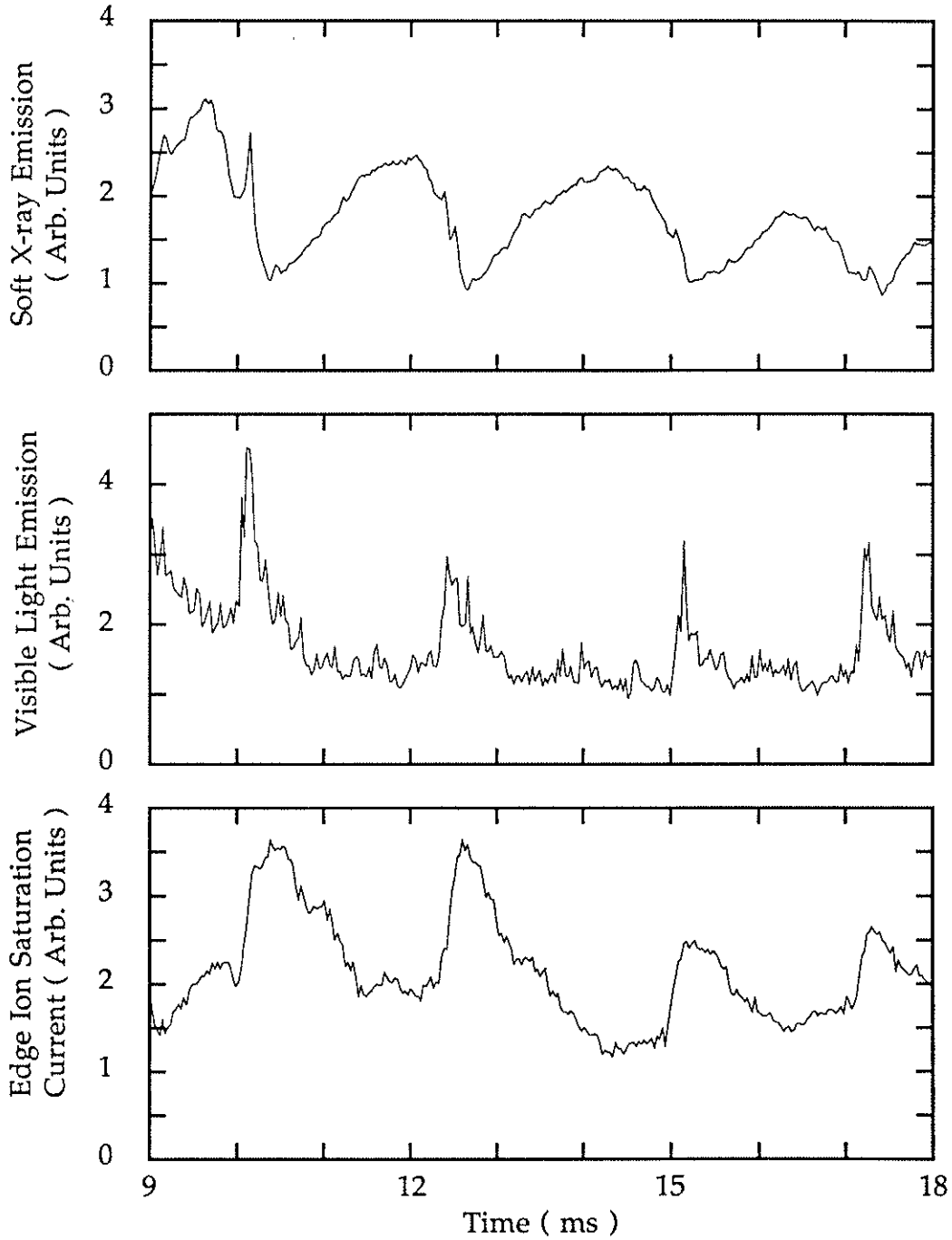

Figure 4.9: Sawteeth are seen on central chord soft x-ray signals, while inverted sawteeth are observed on edge diagnostics.

crash. This array only covers the central region of the discharge, $r \leq 0.6a$. Out to this radius, no inversion of the soft x-ray emission is observed, only a *cooling* of the central region. In the tokamak sawtooth, inverted sawteeth are observed outside of the $q \approx 1$ radius.[12] The inverted sawteeth are a result of the rapid radial transport of the *hot* central plasma into the *cooler* edge regions.

To determine if the entire MST plasma column was *cooling* or if the sawtooth crash resulted in energy being removed from the center of the discharge towards the edge as is suggested by the increase in other edge diagnostics, a swivel soft x-ray detector was installed. This detector could view the center of the discharge, $b \approx 7.6$ cm, as well as the edge, $b \approx 47.4$ cm (b being the impact parameter of the detector; see figure 3.6b). Indeed inverted sawteeth were observed in the edge soft x-ray emission; see figure 4.10. The inversion radius is ~ 35 cm or ~ 0.65 a - just outside of the "radial" array.

To obtain the soft x-ray profiles before and after the sawtooth crash, shot averaging was required. Deeply reversed discharges, $F \approx -0.2$, were used in order to have strong sawtooth activity. To determine the profiles, the sawtooth nearest to 10 ms was chosen. This time was chosen since the soft x-ray emission had reached its equilibrium value, and the sawteeth were still strong due to the ramping plasma current - the plasma current peak typically occurs near 15 ms; and at 10 ms, it is > 90% of its peak value. The time for the initial profile was taken as

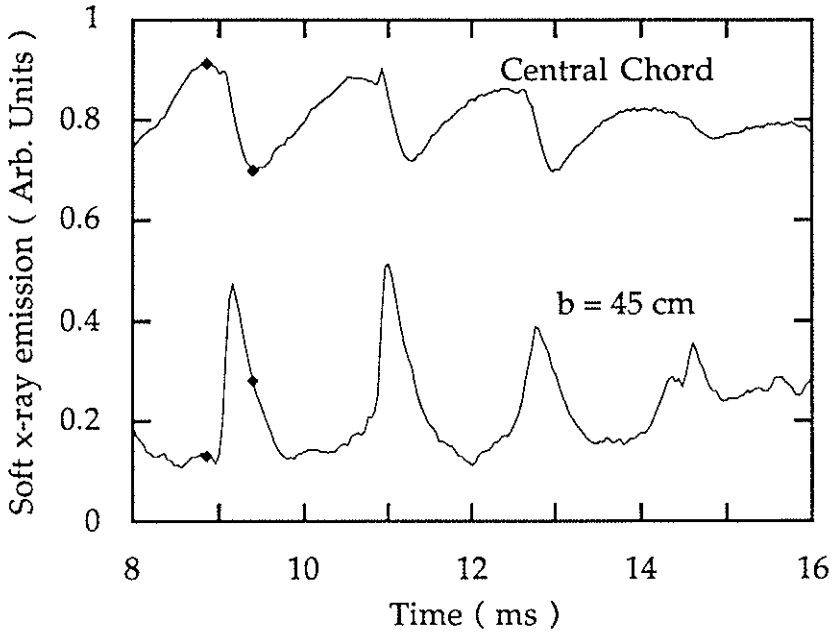

Figure 4.10: Inverted sawteeth are observed in the edge soft x-ray emission. Points marked are times used in the soft x-ray profile measurements; see Fig. 4.11.

being 0.25 ms before the sawtooth crash - the crash time determined by the peak of the change in the toroidal flux, $\dot{\Phi}_\phi$. The "after" profile was taken at the time of the minimum of the central chord signal. These times are marked in figure 4.10. The *after time* was typically after the peak of the edge soft x-ray emission. The profiles were determined at the minimum of the central chord to emphasize the change in the central region to the edge region. While the edge emission has decreased by about half its maximum, it is still an order of magnitude below the

central chord. This also avoided the burst observed in the soft x-ray emission which corresponds to the flux jump. The resulting profiles are shown in figure 4.11. The RFP sawtooth crash is similar to the tokamak sawtooth crash - the hotter plasma in the center is transported to the cooler edge.

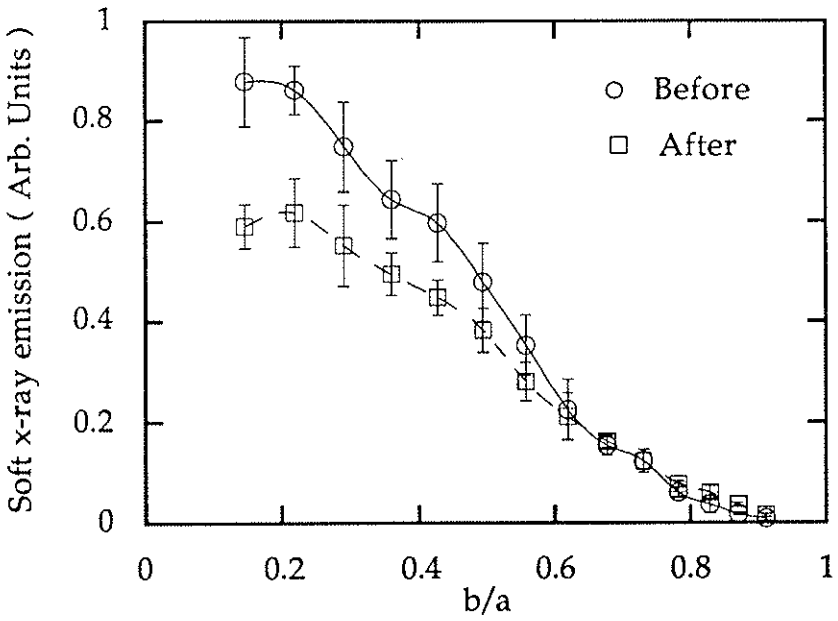

Figure 4.11: Radial profiles of the soft x-ray emission as measured by a movable soft x-ray detector. The inversion radius is at ~ 35 cm or $b/a \approx 0.65$. b is the impact parameter of the dectector.

The inversion radius measured on MST is consistent with other RFPs which have observed inverted sawteeth. For example, the ZT-40M RFP observes an inversion radius of ~ 0.6 a.[13] In both cases, the inversion radius is inside of the reversal surface ($r_{rev} \sim 43$ cm for MST).

Since the date of the above profiles were taken, soft x-ray tomography has been performed for the sawteeth on the MST.[14] Figure 4.12 shows the soft x-ray emissivity before and after the sawtooth crash. As in the case of the swivel detector profile, the central emissivity decreases. These reconstructions were obtained from the original poloidal array of detectors that were described in chapter 3. Due to the coverage of this array, no new information on the edge of the discharge can be obtained at this point, as discussed in section 3.2.3.

In high temperature plasmas like that of the RFP, the soft x-ray emission increases with both the plasma density and temperature. The dependence on each quantity is not known for the MST so no internal profile information can be extracted from the soft x-ray profiles at this time. But the profile modifications can be determined from other diagnostics. Many of these are implied, but are consistent with the profiles measured on other RFPs.

The electron density profile flattens during a sawtooth crash. This is implied by comparing the central chord, line averaged density to edge density measurements made with Langmuir probes. During a sawtooth

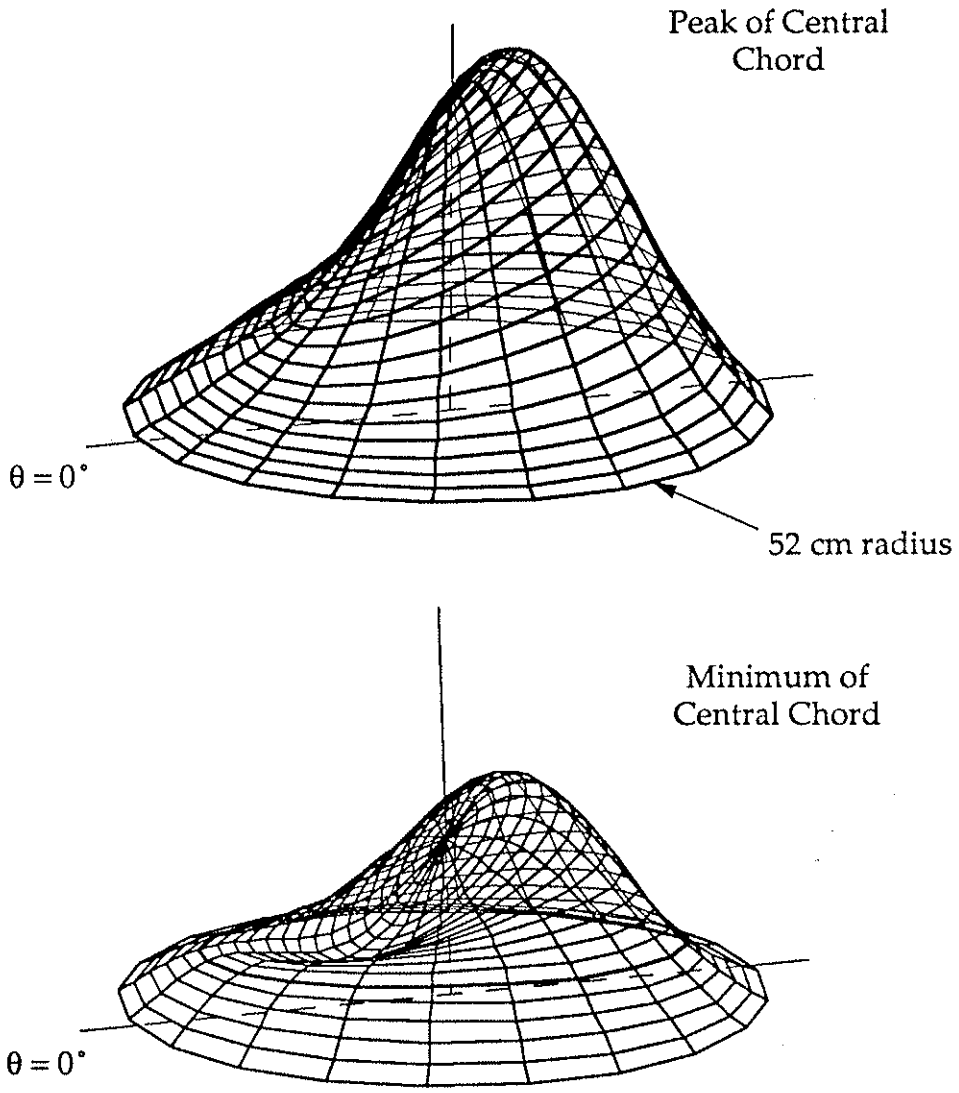

Figure 4.12 Soft x-ray tomography on the MST before and after a sawtooth crash.

crash, the line-average density decreases while the edge density increases; see figure 4.13. In this figure, the edge ion saturation current is plotted as a representation of the edge density (edge measurements suggest that the change in the ion saturation current is primarily due to an increase in the electron density.[15]) Also, many of the diagnostics which monitor the line-radiation due to plasma impurities show an increase as well. Although no profile information is available, these trends suggest that the sawtooth crash flattens the density profile, and that there is a rapid radial transport of density towards the edge. The "rapid" transport of the density is suggested by the rapid increase in the impurity signals. If the increase was due to recycling from increased wall interactions, a slower response would be expected.[16] The flattening of the profile has been measured by the ZT-40M group using several radial interferometer chords,[10] and indeed the central density decreases while the edge density increases - the density profile is flattened. A limited number of chords were used so no true profile changes could be obtained, except to demonstrate that the profile is flattened.

The ZT-40M group has also measured the central electron temperature and density during a sawtooth crash.[17] This was accomplished by phase-averaging the Thomson scattering data over the sawtooth crash of a central chord soft x-ray signal. The variation in $T_e(0)$ was of the order of 30% for a 120 kAmp discharge. A similar decrease in the central electron density was also measured. While the central temperature and density decreased, no direct measurement of the radial

temperature profile change has been accomplished. This phase-averaging technique has been applied to the MST sawteeth, but no clear change in $T_e(0)$ or $n_e(0)$ could be seen outside of the statistical error of the diagnostic.[18]

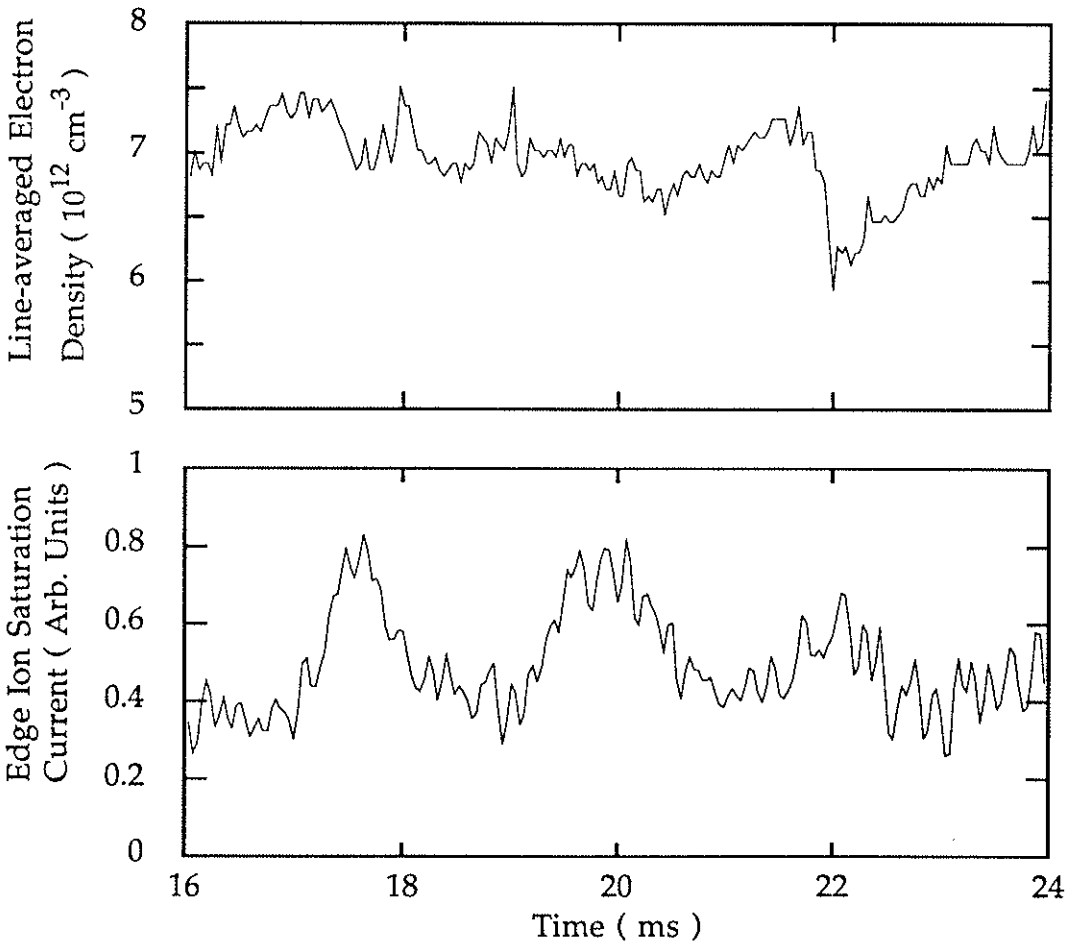

Figure 4.13: The line average density decreases, as the edge density increases.

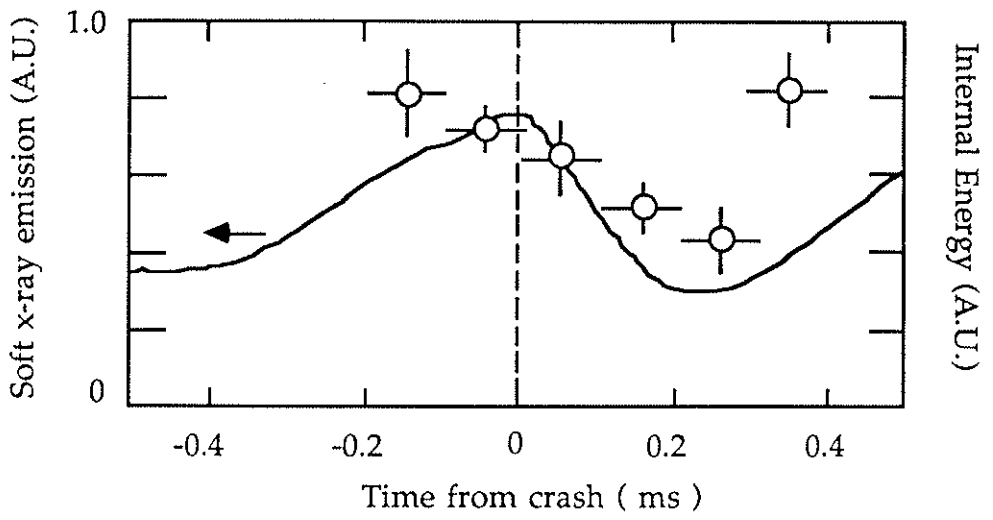

Figure 4.14: The internal energy of the plasma ($n_e(0)\ T_e(0)$) decreases during a sawtooth crash (adapted from Fig. 3 from Ref. 17).

From these phase-averaged measurements, the axial energy density ($n_e(0)\ T_e(0)$) of ZT-40M is plotted in figure 4.14 versus the soft x-ray emissivity.[17] The internal energy of the plasma recovers more quickly than the soft x-ray flux. This is believed to be due to a nonthermal component in the soft x-ray energy spectrum. This is evident in the time-averaged soft x-ray energy spectrum measured during high Θ discharges with sawteeth and during low Θ discharges without sawteeth in the ZT-40M device.[17] In the low Θ discharges, a high-energy component is observed. The temperature of this component is typically three to five times that of the bulk plasma. This component was not present during the high Θ discharges. The lack of the high-energy component in the high-Θ discharges is believed to be due to the degraded confinement for the high-Θ discharges so that the high energy tail does

not contribute as strongly to the soft x-ray energy spectrum. In order to make a direct connection between the sawteeth and this high energy tail, better time resolution of the energy spectra during a sawtooth event is required. At this time, no energy spectrum is available for the MST discharges. But if a high energy component is present in the MST discharges, this could explain the burst observed in the soft x-ray flux and in the hard x-ray flux described in section 4.2. The high energy component could also explain the large amplitude of the sawtooth crash compared to the *equilibrium* level in the soft x-ray emissivity.

Additional MST profile modifications can be inferred from the asymmetry factor calculated from edge magnetic signals. The asymmetry factor, Λ, is defined as

$$B_\theta(r, \theta) \approx B_{\theta_o}(r) (1 + \varepsilon \Lambda \cos \theta) \qquad 4.1$$

where ε is the inverse aspect ratio. Figure 4.15 shows the evolution of Λ during a sawtooth crash. In equation 4.1, Λ can be expressed by $\Lambda = \beta_\theta + \frac{\ell_i}{2} - 1$ where β_θ is the ratio of the plasma pressure to the magnetic pressure, $\beta_\theta \equiv \frac{2\mu_o<p>}{B_\theta(a)^2}$, and ℓ_i is the normalized energy inductance of the poloidal field, $\ell_i \equiv \frac{<B_\theta^2>}{B_\theta(a)^2}$.[19] The decrease in Λ during the sawtooth crash suggests either a flattening of the current profile, a flattening of the pressure profile, or a combination. No profile information is available for either of these effects on MST so detailed descriptions are limited. The flattening of the current profile could be an explanation of the

inward shift of the plasma during a sawtooth crash as interpreted from edge magnetic signals. The flattening of the current profile decreases the plasma inductance thus causing the equilibrium position of the plasma to shift inward.[20] On the other hand, if the changes in Te(0) and ne(0) for the MST were comparable to those discussed above for ZT-40M, the change in β_θ could also explain the decrease in Λ. But once again, no profile information is known for $T_e(r)$ and $n_e(r)$ to accurately determine the change in β_θ, and no current density profiles are known to determine ℓ_i.

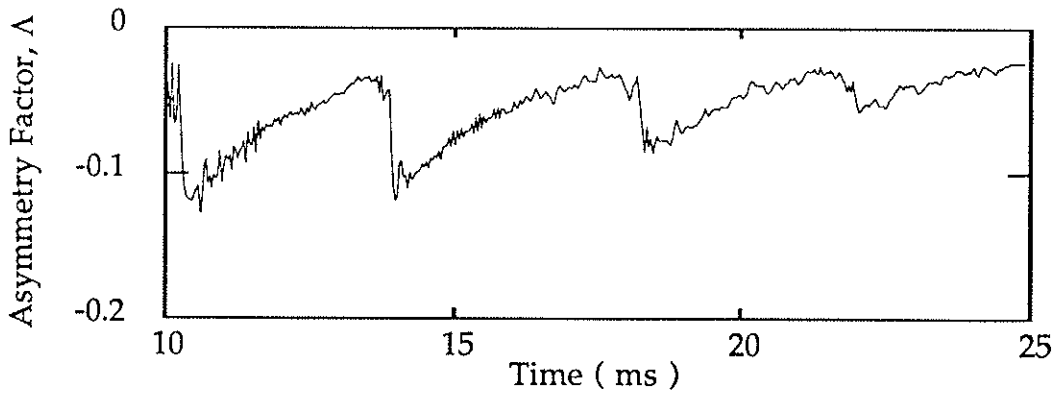

Figure 4.15 The asymmetry factor, Λ, decreases during a sawtooth crash.

While no direct measurement has been made for the MST, changes in the current profile have been measured by other RFP groups.[21, 22] The magnetic field profiles measured on the ETA BETA II RFP during a sawtooth crash are shown in figure 4.16. In this figure, the experimental

data points (~ 10 radial positions for each magnetic field component are equally spaced across the minor radius) have been fit to cubic splines and the resulting curves are shown. The magnetic field profile before the sawtooth crash has a sharper gradient in the central region than the profile after the sawtooth crash. This results in the on-axis current density being larger before the crash than after the crash - the sawtooth crash flattens the current profiles.

Also shown in figure 4.16 are the λ and q profiles derived from the measured magnetic field profiles. The sawtooth crash has flattened the λ profile. The flattening of the λ profile stabilizes the plasma to the m = 1 tearing modes which are the driving force behind the sawtooth crash.[23] In the above experiments,[21, 22] the sawtooth crash occurred when the central q value fell below $\sim \frac{2}{3}\frac{a}{R}$. This suggests a lower q limit for the RFP similar to the $q > 1$ stability limit for the tokamak.[24] For the MST, the MPFM model which was described in chapter 3 results in $q(0) \approx 0.23$. This is consistent with the q(0) limit predicted by Antoni, et. al. based on the stability of the plasma to the m = 1 tearing modes.[25] The raising of the q(0) is also consistent with the MHD theories described in chapter 2.

Although the profile modifications for the MST sawteeth described above are implied, the limited number of experimental observations are consistent with other RFP devices for which various profile changes have been measured. But as will be discussed below, to truly understand the RFP sawtooth and its effects on plasma confinement, better profile

information is required both for the equilibrium profiles and for the changes during a sawtooth.

4.4 Toroidal asymmetry of the crash

One difficulty in measuring the profiles described above is the toroidal asymmetry of the toroidal flux generation - this may require the profile changes to be measured at several toroidal locations. This effect is shown in figure 4.17 where the toroidal flux, Φ_ϕ, measured at two different toroidal locations is plotted along with their time rates of change, $\frac{d\Phi_\phi}{dt}$. The flux increase first appears at $\phi \approx 0^\circ$ (this is a flux loop placed as close as possible to the poloidal flange) and appears later in time at $\phi = 240^\circ$. The toroidal speed of the flux disturbance shown in figure 4.17 is $\sim 3 \times 10^6$ m/s (this speed is comparable to the Alfvén speed for this discharge). This flux *disturbance* transits the torus once - it does not reappear at the same location until the next sawtooth event, several milliseconds later. On the ZT-40M RFP,[10] the *disturbance* spreads out toroidally as it propagates around the torus. The rate of change of the flux is slower the further away from the initiation point. This is evident in both the rise and decay portions of the flux disturbance. This effect is not as dramatic on the MST and usually only appears in the rise phase, if apparent at all.

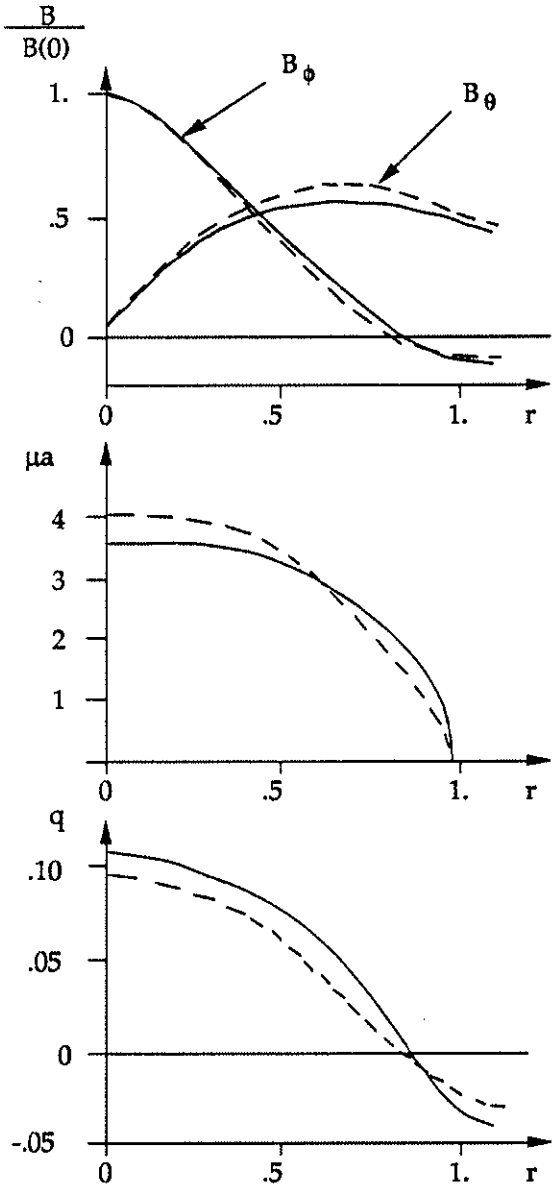

Figure 4.16 a) Magnetic field profiles measured during a sawtooth crash, b) λ profile and c) q profile derived from the magnetic profiles in (a) on Eta Beta II (Ref. 25).

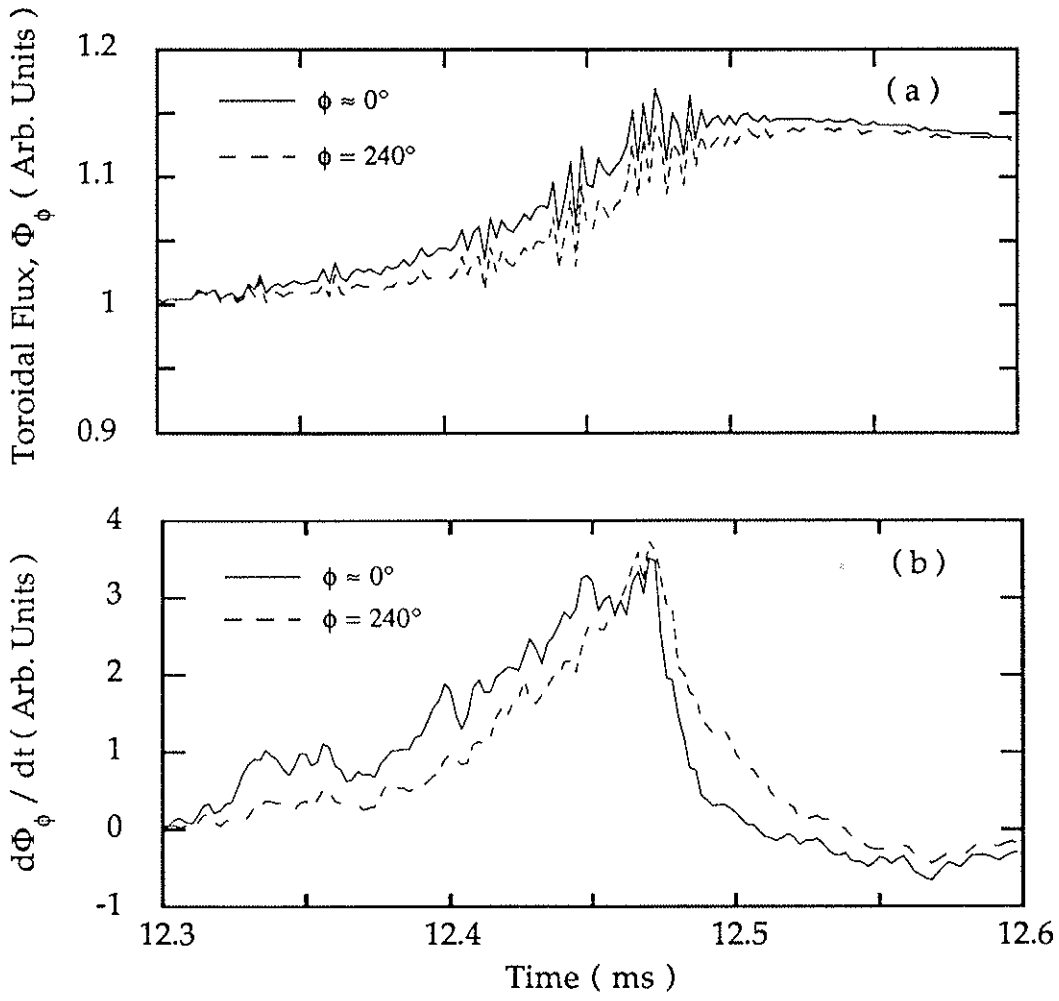

Figure 4.17 The toroidal flux generation is toroidally asymmetric. (a) The toroidal magnetic flux, Φ, measured at $\phi \approx 0°$ and at $\phi = 240°$. (b) The time rate of change, $\frac{d\Phi_\phi}{dt}$, measured at these same locations.

Although the flux generation was initiated at one toroidal location, there was no preferred toroidal position in the ZT-40M RFP. On the other hand, in the cases where a distinction can be determined, the flux generation is initiated at the poloidal gap, $\phi = 0°$, in the MST. This may be attributed to the magnetic field errors contributing to the interaction of the m = 1 tearing modes.[26]

The ZT-40M group has also observed a toroidal dependence in the soft x-ray emissivity.[27] Unlike Φ_ϕ, the toroidal dependence is only in the rate of decay of the soft x-ray signal. All soft x-ray signals begin to decrease with the initial creation of the toroidal flux. But the rate of decay is smaller for the signals farther away from the point of initiation. The synchronous drop in the soft x-ray emissivity with the initiation of the toroidal flux is attributed to the rapid thermal transport from the center of the discharge. The different decay rates are possibly due to different field-line path lengths from the core of the discharge to the edge.[28] This dependence has not been observed on the MST soft x-ray signals - all toroidal signals decay simultaneously within the 2 μsec time resolution set by the digitization rate. However, viewing such an event is hampered by the slow decay of the soft x-ray emissivity before the flux generation occurs, and by the *burst* in the soft x-ray signal which accompanies the flux generation. Both of these events were described in section 4.2.

The flux generation travels in the electron diamagnetic drift direction (parallel to I_ϕ). On the other hand, the precursors described in section 4.1 travel in the opposite direction. At this time, I am aware of no theoretical basis for these directions.

A physical picture has been proposed by Howell, et al.[29] of a m = 0 island forming at one toroidal location. The difference between the momentum transferred to the island from the electron and the ion collisions with the wall results in a net momentum transferred to the island. The difference in the speeds of the leading and trailing edges would also be due to the electron and ion collisions. The magnetic reconnection, which would be responsible for the generation of net positive toroidal flux, would occur when the leading edge catches up to the trailing edge of the island.

4.5 Mode evolution during a sawtooth

As described in section 4.1, m = 1 precursors are observed in the magnetic and soft x-ray signals prior to a sawtooth crash. These modes are believed to be responsible for the magnetic flux generation through their nonlinear interactions.[30] Many other RFPs have observed an increase in the m = 1 magnetic fluctuation level followed by an increase in the m = 0 fluctuations.[31] Using the internal edge magnetic coil arrays described in section 3.2.2, the mode evolution of the precursor fluctuations can be determined. This section will describe their linear

evolution up to the flux jump, and their nonlinear interaction occurring during the flux jump.

The time rates of change of the poloidal magnetic field, $\dot{B}_\theta$, as measured by the toroidal magnetic array are shown in figure 4.18. These signals are analog filtered in the 1-250 kHz range and are digitized at a rate of 500 kHz. The precursor structure is quite evident while the mode structure at the time of the flux jump is very complicated.

Linear mode analysis is performed on the toroidal array to obtain the n mode spectrum, $\dot{B}_\theta(\phi_i) = \sum_{n=0}^{n_{max}} a_n \cos(n\phi_i) + b_n \sin(n\phi_i)$. The same analysis is applied to the poloidal arrays to obtain the m spectrum. The toroidal and poloidal arrays are one dimensional thus the mode numbers can only be determined for all m or n, for example, $a_n = \sum_{m=0}^{\infty} a_{n\,m}$. No information can be extracted on helicity of the modes, (m, n) combinations other than generalities. The toroidal array has 64 coils; this limits the maximum number of n's to be 32 for a minimum of two points per wavelength. This limit is sufficient in determining the precursor modes, but as will be discussed below, it is not sufficient to determine the evolution during the flux jump.

From the poloidal array, the precursors are m = 1, and from the toroidal array, they have a modal structure in the range n = 5 - 8. The time evolution of the amplitude of the n = 6, 7, and 13 components are

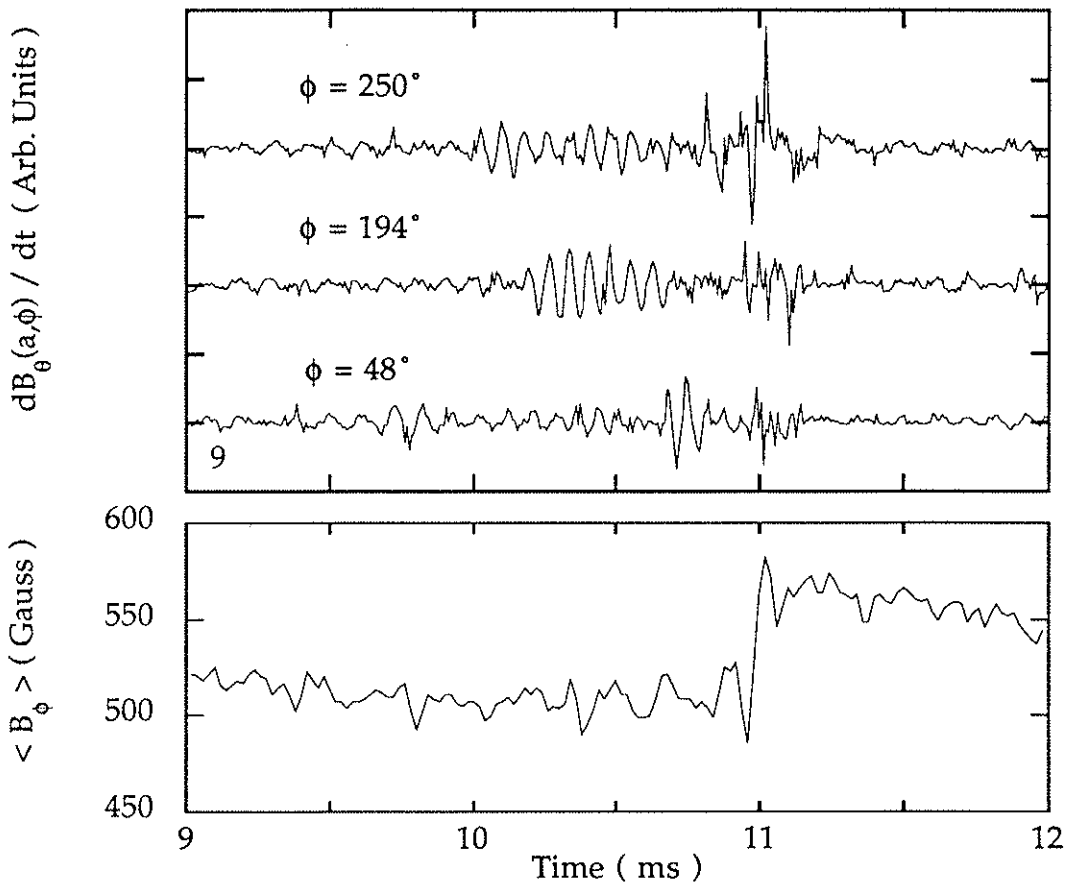

Figure 4.18 $\dot{B}_\theta$ during a sawtooth event as measured by the internal toroidal array and the average toroidal field for reference.

shown in figure 4.19, $A_n \equiv \sqrt{a_n^2 + b_n^2}$. The n = 6 and 7 modes begin to grow at $t \approx 9.5$ ms while the n = 13 component stays relatively constant. The n = 13 mode could be driven by the nonlinear interaction of the n = 6 and 7 modes, but it is only shown here as a representative of the level of the higher n modes which do not make up the precursor spectrum. The amplitudes shown in figure 4.19 are derived from the $\dot{B}_\theta$

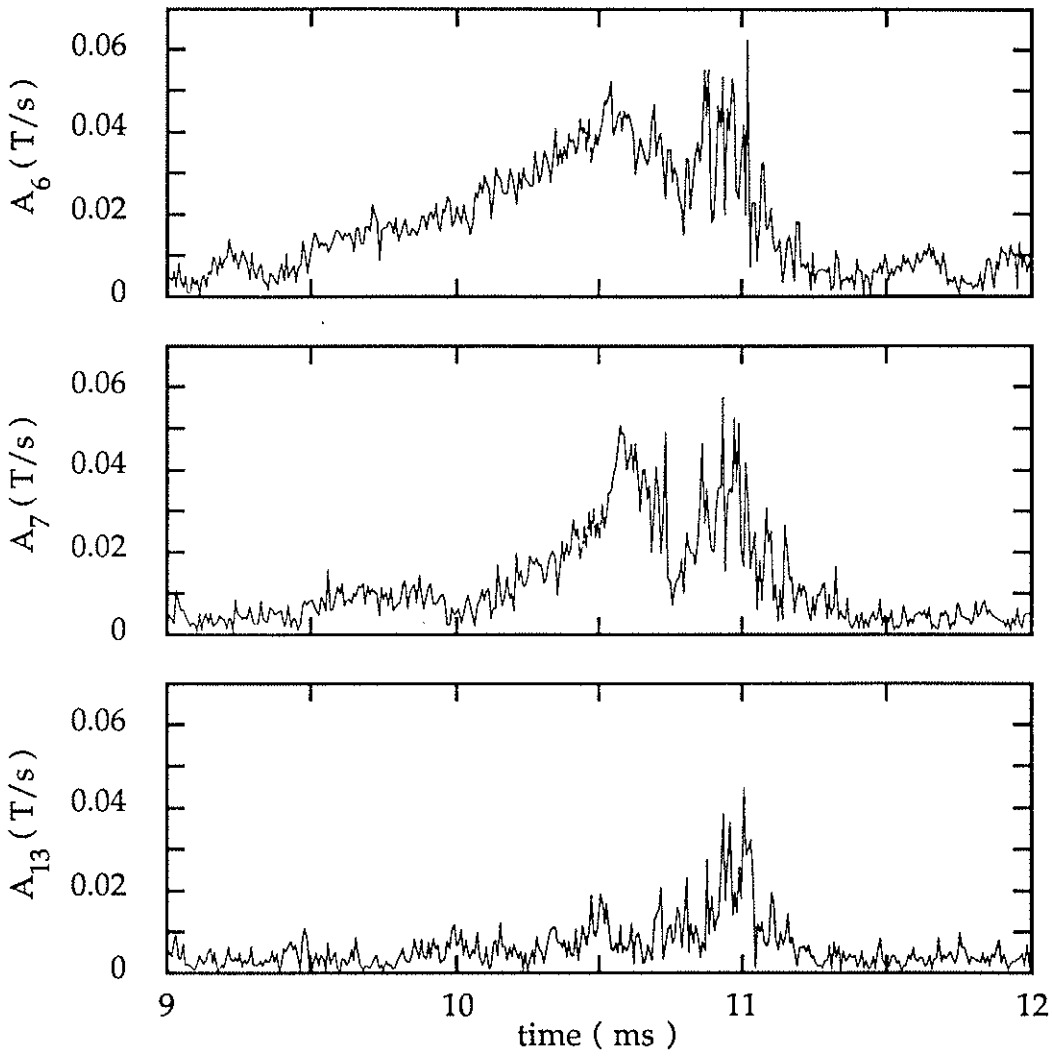

Figure 4.19 The amplitude of the n = 6, 7 and 13 modes during a sawtooth event.

signals - no integration has been applied either analog or digitally. For the rise phase of this sawtooth, t ≈ 9 - 10.5 ms, the precursor frequency remains constant. This is evident by the linear time dependence of the phase of the n = 6 mode which is shown in figure 4.20. Since the frequency is constant in this region, the increase in the $\dot{B}_\theta$ amplitudes, A_n, is representative of the true amplitude increase of the B_θ signals.[32] Similar increases are observed in the m = 1 and m = 0 mode amplitudes determined from the poloidal array.

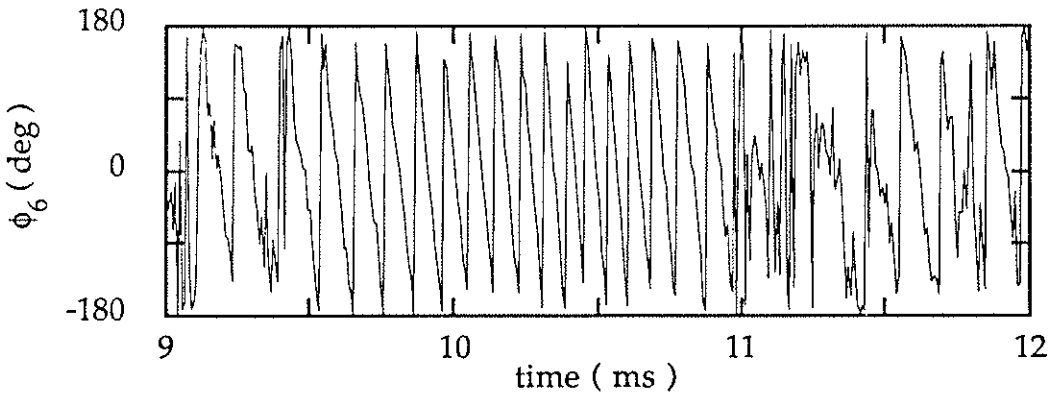

Figure 4.20 The phase of the n = 6 mode during a sawtooth event.

At the time of the flux jump, t ≈ 10.7 - 11 ms, the mode structure becomes quite complicated. Using 2-pt correlation techniques and ensemble averaging ~ 400 sawtooth events, the n spectrum is strongly peaked prior to the flux jump with the dominant n's in the range 5 - 8. When the flux jump occurs, the spectrum is broadened and extends out to n ~ 100. The higher n's are primarily due to the higher frequencies, 100-250 kHz. These high n numbers severely alias the linear

decomposition described above. For this reason, the mode evolution shown in figure 4.19 is not a reasonable representation during the flux jump interval.

Initial results of 2-pt bispectral calculations indicate that nonlinear coupling is occurring during the flux jump. These calculation have been performed in the frequency domain, and, at this time, no information can be obtained as to which modes are interacting. This would require bispectral decomposition in the k space.

While the MST has a complete toroidal array and two complete poloidal arrays, the mode analysis can only be determined in either the n or the m spectrum. No information can be determined for a given (m,n) combination. On TPE-1RM15, Hattori, et al.[33] have heuristically determined the mode evolution of the m = 0 and m = 1 modes using two partial toroidal arrays separated by $\theta = 180^{\circ}$. As the precursor modes grow, a broadening of the m = 1 n-spectrum is observed. Prior to the flux jump, an increase in the m = 0, low-n modes, with n = 1 being the dominant mode, is observed. This suggests that nonlinear coupling of the m = 1 modes is generating the m = 0 modes.

The nonlinear interaction of the m = 1 tearing modes is believed to be responsible for the generation of the toroidal flux observed during a flux jump.[34] Experiments have now been able to observe the growth of the m = 1 modes, termed precursors, prior to a flux jump. Initial results suggest that nonlinear coupling is occurring. Experiments have not been

able to answer the question as to which mode, the m = 1 or the m = 0, is responsible for generating the reversed field, as discussed in section 2.2.

4.6 The dependence of the sawteeth on the pinch parameter, Θ

Up to now the general characteristics of a sawtooth crash have been presented. In the next two sections, the dependence of the sawtooth characteristics on two global plasma parameters will be presented, namely Θ and I_ϕ. These two parameters are related by the definition of $\Theta, \frac{\mu_o I_\phi}{2\pi a <B_\phi>}$. In this section, I_ϕ is held constant, and Θ is scanned by varying the amount of reversal. Θ is used as the scanned parameter instead of F to be consistent with other publications. In section 4.7, Θ is held constant, and I_ϕ is varied.

The theoretical models described in chapter 2 predict that the sawtooth activity should be more dramatic at high values of Θ, that is, at deeper reversal. This has been observed in various RFPs,[35] and in many, the sawteeth are only observed at values of $\Theta \geq 1.6$. This nature is shown in figure 4.21a where the change in the toroidal flux, $\delta<B_\phi>$, during a sawtooth crash is plotted versus Θ for a set of MST discharges. The data points in this figure are for discharges with $I_\phi \approx 300$ kAmps, and only the sawteeth in the portion of the discharge where the current is > 90% of the peak current are included. The Θ values, <Θ>, are averaged over the period of the sawtooth including the crash portion. As <Θ> is increased, the amount of toroidal flux that is created during a sawtooth crash is

increased. Figure 4.21b shows the same data versus the sawtooth-averaged F value for comparison.

While some of the scatter is due to shot-to-shot variations, there is a large amount of scatter in one shot. This is shown in figure 4.22 where $\delta<B_\phi>$ is plotted for several shots all with shot-averaged $\Theta \approx 1.6$ (this is the average over the 90% peak current portion of the discharge). Even though all the sawteeth are within the 90% peak current interval, the ramped nature of the discharge has an effect on the amount of flux generated. The flux generated by a sawtooth crash is the largest during the rising current portion of the discharge.

For the discharges shown in figures 4.21 and 4.22, field reversal occurs for $\Theta \gtrsim 1.5$. In the MST, the sawtooth phenomena are observed at shallow reversal, $\Theta < 1.6$, as well as deep reversal. Also, a sawtooth-like oscillation is observed in nonreversed discharges as well; see section 4.1. Similar oscillations have been observed in the HBTX1B RFP when operated at low values of Θ but still reversed[36] and in the Reverstron II experiment when operated as a ultra-low q device - a "nonreversed" RFP.[37] The change in the toroidal flux for the nonreversed MST discharges is plotted in figure 4.21 for comparison with the reversed sawteeth. The increase with Θ appears to occur only for the reversed discharges. Limitations in the field programming, limited Θ to be $\gtrsim 1.2$.

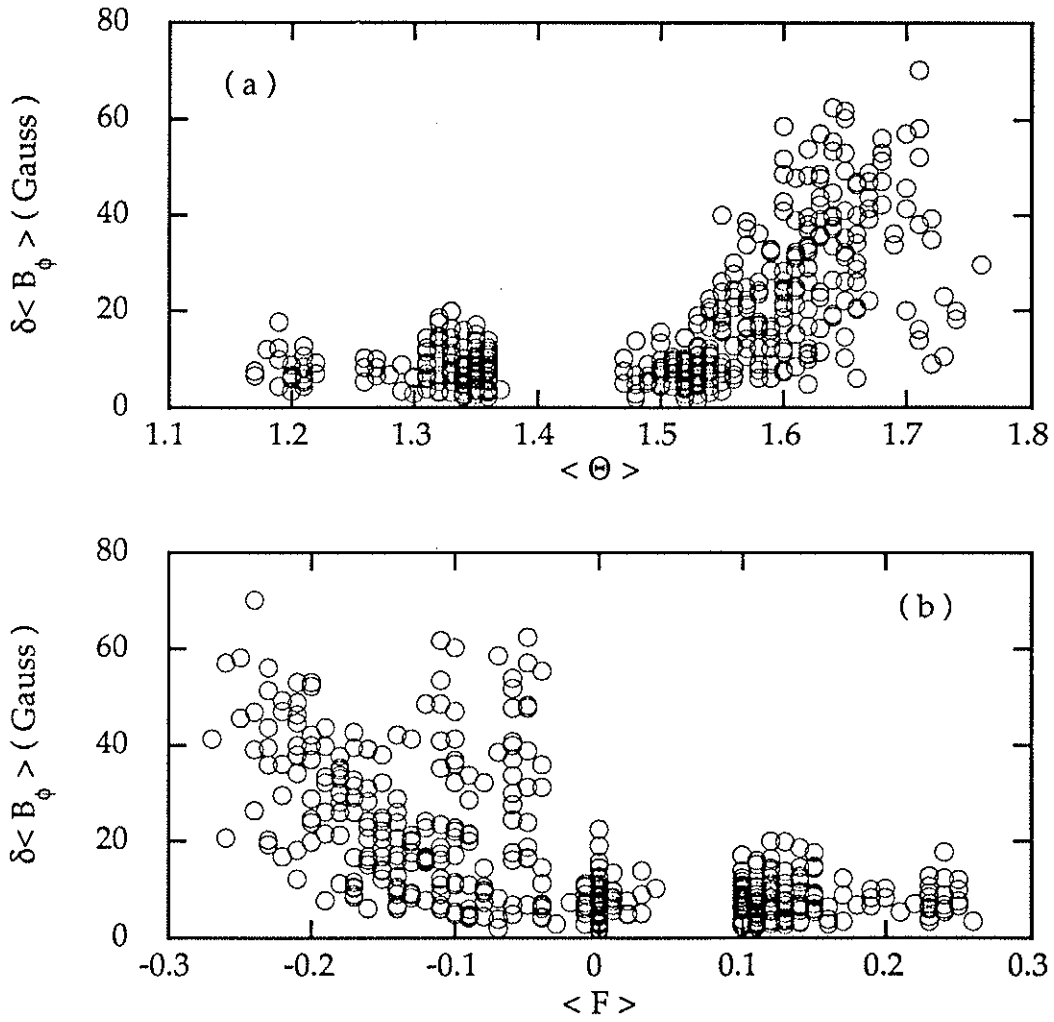

Figure 4.21 (a) The change in the toroidal flux, $\delta < B_\phi >$, versus the average Θ during each sawtooth, $< \Theta >$. (b) The same data plotted versus the average F, < F >.

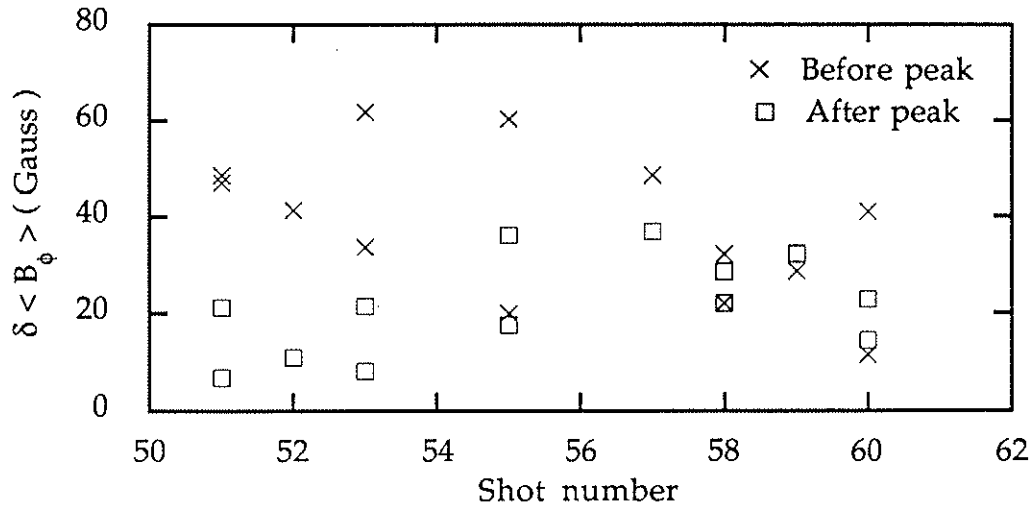

Figure 4.22 The change in the toroidal flux, Φ, for several shots all having the shot averaged $\Theta \approx 1.6$.

The period of the sawteeth also increases with Θ; see figure 4.23a. The period is defined as the time interval between the minimum of the $B_\phi(a)$ of the previous sawtooth to the minimum of the present sawtooth; see figure 4.23b. This is opposite to the HBTX1B oscillations; the HBTX1B period decreases with Θ,[36] while other RFPs have reported seeing no dependence of the period with Θ.[38]

Even though the sawtooth period and the change in the toroidal flux increase with $< \Theta >$, no clear correlation between the period and the change in flux is evident - a longer period does not result in a larger amount of flux being generated, or visa versa.

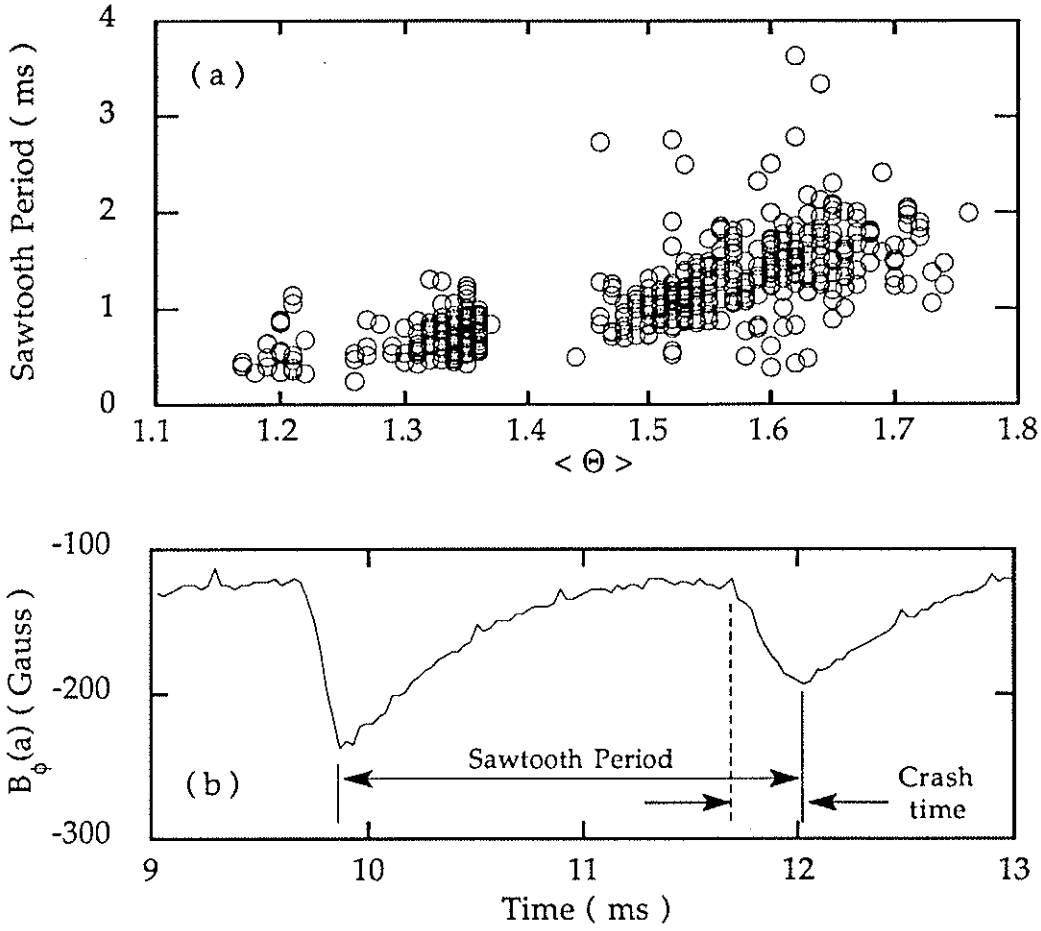

Figure 4.23 (a) The sawtooth period as a function of the sawtooth averaged Θ value. (b) The definition of a sawtooth period and of the crash time.

Unlike the previous quantities, the crash time of the sawteeth does not show a dependence on Θ; see figure 4.24. In this figure, the crash time is taken as the time interval for the change in the $B_\phi(a)$ signal to occur; see figure 4.23. Again, no correlation is observed between the crash time and either the period or the change in toroidal flux.

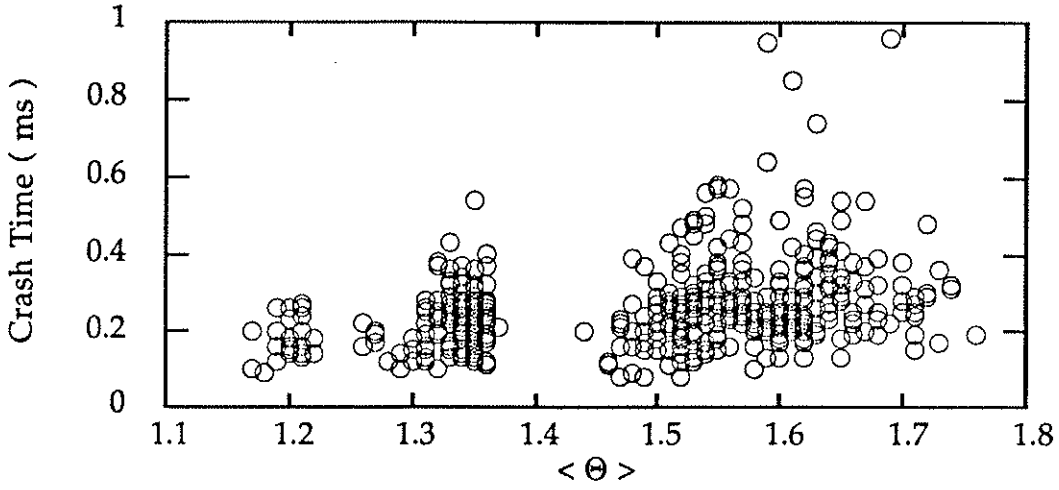

Figure 4.24 The sawtooth crash time does not have a strong dependence on $< \Theta >$.

The normalized root-mean square (RMS) fluctuation level in the soft x-ray emissivity increases with Θ for the reversed discharges; see figure 4.25. The normalized RMS level is defined as $\frac{\Delta I}{I} = \frac{RMS(I - I_{Equil})}{< I_{Equil} >}$ where I_{Equil} is the equilibrium level of the soft x-ray signal, digitally filtered below 200 Hz, and $< I_{Equil} >$ is the average of this signal over the 90% peak current time interval. The Θ values plotted in figure 4.25 are also averaged over the 90% peak current time interval. The upper frequency limit is 250 kHz and is set by the amplifiers used for the soft x-ray measurements, although most of the power lies below 100 kHz.

The opposite appears to be true for nonreversed discharges, the RMS level increases with decreasing Θ. At the lower limit of Θ available on MST, Θ ≈ 1.2, the strong oscillations were not present in the soft x-ray emission, although, the oscillations are still visible in the magnetic signals, $B_\phi(a)$ and $\langle B_\phi \rangle$. But at this time only a few *low* Θ points were available due to the limitations on the field programming for the MST so it is not clear if the soft x-ray oscillations reappear at a lower Θ, or at what Θ value the magnetic oscillations disappear.

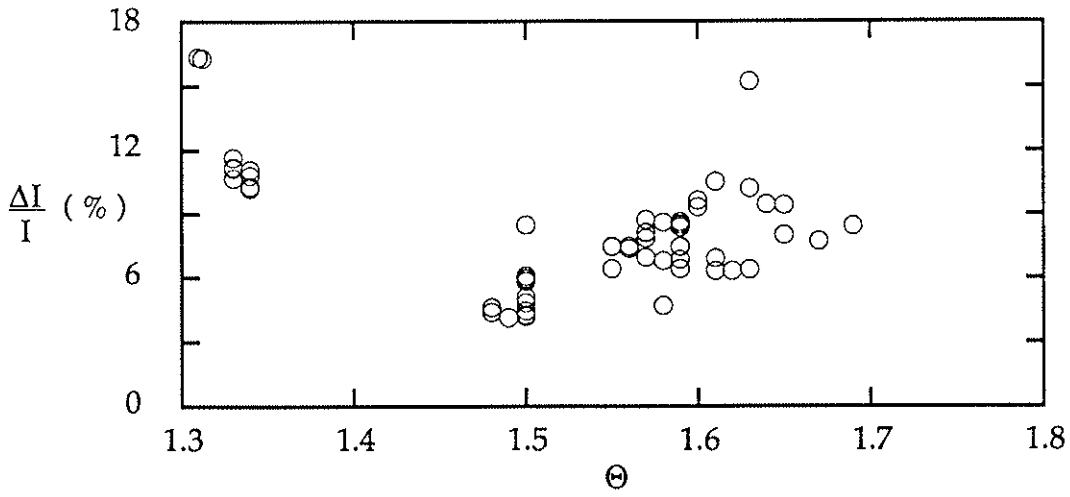

Figure 4.25 The normalized RMS level of the soft x-ray oscillations increase with Θ for reversed discharges.

The data shown in figures 4.21 to 4.25 were from the initial operation of the MST. In general, the trends are the same for data taken after the installation of the PF winding. The only difference being longer periods

have been observed after the PF winding installation. This will be discussed in the next section.

4.7 The dependence of the sawteeth on the plasma current or the plasma resistance

It has been mentioned previously that the sawtooth rise-time is a resistive diffusion process. As a result, the magnetic profiles evolve on a resistive time scale. The period of the sawtooth would then scale with the plasma resistance. A parameter which can be used to scale the resistance is the magnetic Reynolds number, $S \equiv \tau_R / \tau_A$. This effect has been simulated by Kusano and Sato,[4] and in these simulations, the sawtooth period increased with S; see figure 2.6. This section will describe the experimental observations based on the *resistance scaling* of the sawteeth.

To experimentally test the results of Kusano and Sato, a set of discharges was chosen in which the plasma current was scanned, 200 - 500 kAmps, while holding Θ constant, $\Theta \approx 1.8$. The Alfvén time is defined as $\tau_A \equiv a\sqrt{\mu_0 \rho}$ / B. The magnetic field strength is calculated from the plasma current, $B = \frac{\mu_0 I_\phi}{2\pi a}$, and the central electron density as measured by Thomson scattering is used for the mass density, $\rho = m_i n_e(0)$. For this scan, the density was maintained at $8 - 9 \times 10^{12}$ cm^{-3}, thus the Alfvén time should be inversely proportional to the plasma current, $\tau_A \propto I_p^{-1}$.

The resistive diffusion time is defined as $\tau_R \equiv \mu_o a^2 / \eta$ where η is the plasma resistivity. There are a variety of ways for calculating η in the RFP. The classical Spitzer resistivity[39] is given by

$$\eta_{Sp} \equiv 5.2 \times 10^{-5} \; Z_\sigma \ln \Lambda \; T_e^{-3/2}$$

where Z_σ is the resistive anomaly defined by the ion charge, and $\ln \Lambda$ is the Coulomb logarithm. For the electron temperatures measured in MST, $\ln \Lambda$ can be approximated by $\ln \Lambda \approx 31 - \ln(n_e^{1/2}/T_e)$ with T_e and n_e being the central electron temperature and density expressed in eV and m^{-3}, repetitively. For these set of discharges, a $Z_\sigma = 2.0$ has been assumed to be constant for all currents.[40] To account for the increased pitch of the magnetic field lines in the RFP, the Spitzer resistivity is multiplied by a "screw-up factor". The screw-up factor can be calculated from the field profiles derived from the PFM model[41] and is approximated by $\frac{11 (5 + 6 \Theta^2)}{5 (10 + \Theta^2)}$. The use of the Spitzer resistivity relies on knowing T_e and the Z_σ for the discharge, and it assumes both are constant across the plasma radius. A direct calculation of the resistivity is given by $\eta_{loop} = \frac{V_{loop}}{I_\phi} \frac{a^2}{2 R}$ where V_{loop} is defined as the resistive loss term in the energy equation of the discharge. This can be derived from experimental quantities using the PFM; see section 3.2.1.

The resistivity calculated by these three methods is plotted in figure 4.26. It is not in the realm of this thesis to describe the difference between the three curves (the references listed above can be consulted

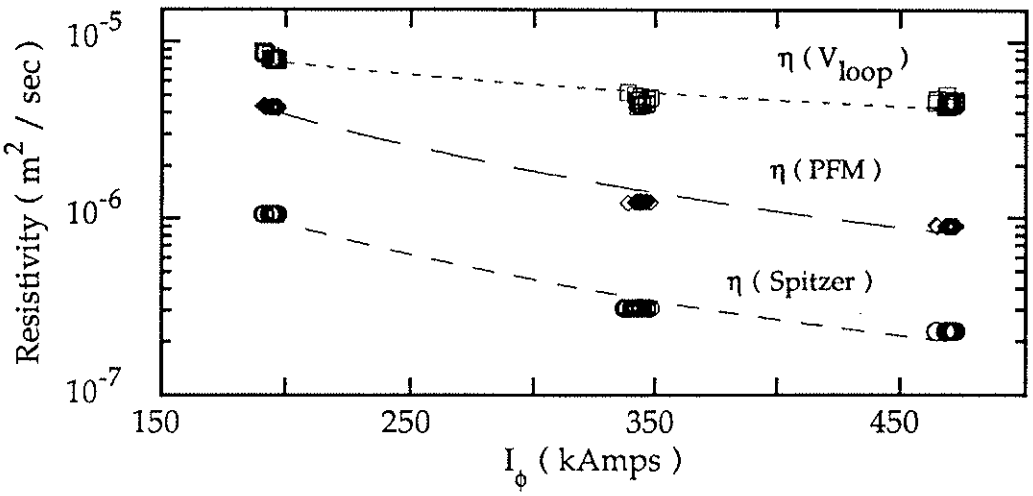

Figure 4.26 The plasma resistivity, η, calculated by the three methods discussed in the text.

for a more detailed description); they are only presented here to get a feel for the S "scaling" for the MST discharges. Using these resistivities, the *scaling* of S with the plasma current for this set of MST discharges is shown in figure 4.27. While there are differences, all resulting from the calculation of η, all three track with the plasma current approximately $S \alpha I^{2.8}$ for S(PFM) and S(Spitzer) to $S \alpha I^{1.7}$ for S(V_{loop}). For this reason, to determine the dependence of the sawtooth characteristics on S, the plasma current will be used as the *independent* variable instead of S. Connections to S will be made in order to compare the experimental trends to those predicted by simulations. In these comparisons, S(V_{loop}) will be used. One should also note that for this scan, the experimental

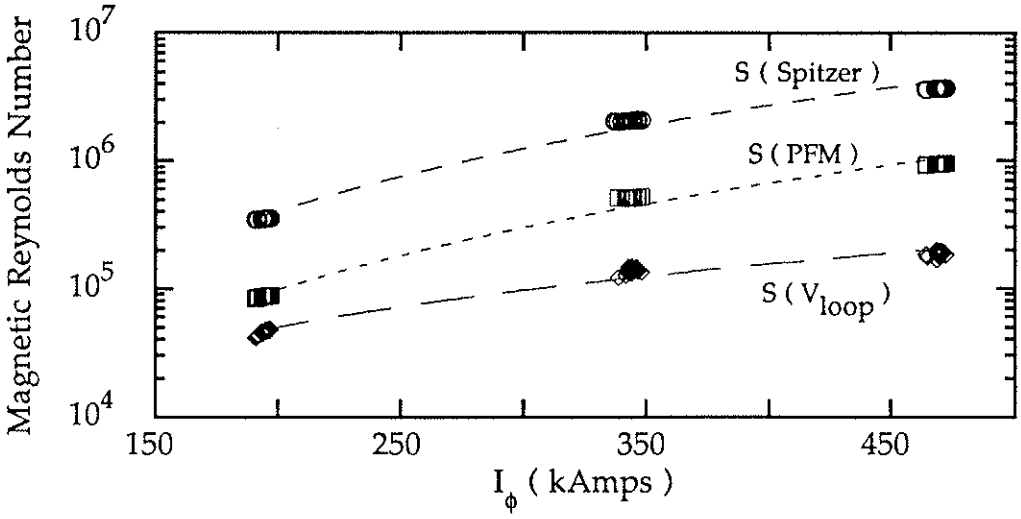

Figure 4.27 The magnetic Reynolds number, S, from the resistivities shown in Fig. 4.26.

range of S is less than an order of magnitude. This range should increase as the plasma characteristics continue to improve in the MST.

To compare with the results of Kusano and Sato, the period of the sawtooth is plotted versus the plasma current in figure 4.28. As in the Θ scan described above, each data point corresponds to a single sawtooth event, and only the sawteeth within the 90% peak current interval were chosen. Due to the *ramped down* nature of the high current discharges, $I_\phi \approx 500$ kAmps, and the longer periods observed at these high currents, many of the sawteeth were not included in the 90% selection process - typically only one or two sawteeth per discharge fell within this time interval. The boxed data points represent this type of sawtooth - a

sawtooth which began after the peak plasma current, but the sawtooth crash occurs after the 90% cutoff interval. While these periods are not the longest of the data set, they do represent the increase in the period as the current is increased. But how they should be included in the *scaling* is unknown since the ramped-down nature of the discharges also decreases the sawtooth activity (see section 4.2). From this plot, the sawtooth period does increase with plasma current and thus increases with S.

To make a direct comparison to the numerical simulations of Kusano and Sato, the normalized sawtooth period (T / τ_A) is plotted versus the magnetic Reynolds number, S(V_{loop}), in figure 4.29. Also plotted are the least squares fit to the data, $\frac{T}{\tau_A} \alpha S^{0.9}$, and the scaling of Kusano and Sato, $S^{1.2..4}$

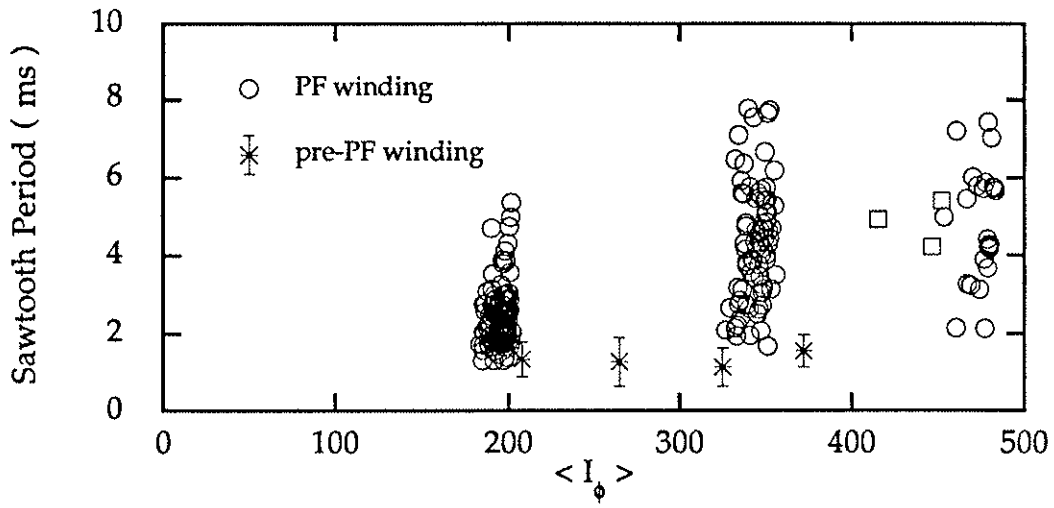

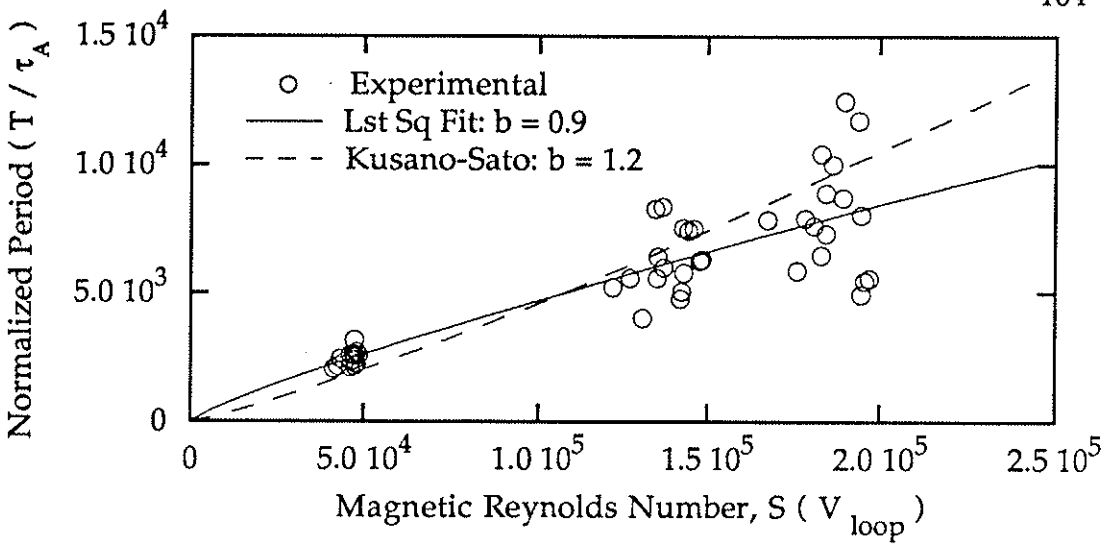

Figure 4.29 The normalized sawtooth period versus the magnetic Reynolds number, S. Curves represent the scaling of the data with S, $\frac{T}{\tau_A} \alpha S^b$.

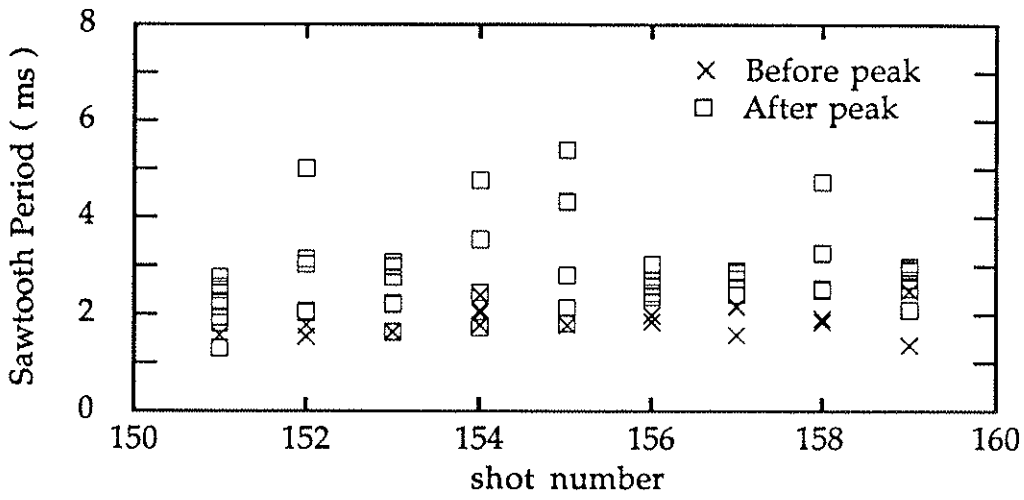

Figure 4.30 The sawtooth period for several discharges with $I_\phi \approx 200$ kAmps.

Like the Θ dependence, there is a large amount of scattering in a single discharge. This scatter may be attributed to the plasma current varying during the data selection window - initially ramped, and later decaying. This is shown in figure 4.30 where the period for several discharges with $I_\phi \approx 200$ kAmps are plotted. The sawteeth before the peak current tend to have a shorter period than those which occur after the peak. Besides the ramped nature of the discharge, the scatter may be due to the higher plasma resistance which is present during the initial portion of the discharges on the MST - the loop voltage tends to be a minimum shortly after the time of the peak current. This higher resistance would lower S, and thus the sawtooth period. In general, there is enough shot-to-shot scatter in both the *before* and the *after* points so that the general trends observed in figures 4.28 and 4.29 are not influenced by the inclusion of both sets of data points.

The increase in the period with plasma current was not observed in a similar scan before the installation of the PF winding. This scan is also plotted in figure 4.28, although for these discharges, the average period is plotted for simplicity. One striking difference between the two current scans is that the periods before the installation of the PF winding are shorter than those after the installation. The lower loop voltage (hence a lower plasma resistivity) achieved with the PF winding could be a factor, but the difference is not enough to account for the change in periods assuming a scaling with S. Another possible explanation is the reduction of the magnetic field errors with the PF winding installed.

The field errors, particularly the m = 1, can enhance the internal kink modes, thus possibly enhancing the sawtooth activity.[42]

For each of these current scans, the loop voltage was approximately constant; thus the general scaling of the period with the plasma current can also be viewed as a scaling with the resistive diffusion time, $\tau_R \alpha \frac{I_\phi}{V_{loop}}$. Alper and Martin[43] have compared the sawtooth period to τ_R for several RFP devices and indeed the period increased with τ_R and appeared to saturate at lower resistances, that is, longer τ_R. This is in qualitative agreement with the results observed on MST. The period increases with τ_R. If added to the device to device comparison, the global trend would appear to saturate, period $\approx$ 4 ms and $\tau_R \approx$ 70 ms for the MST. Although, the scaling with τ_R cannot be directly converted to scaling with S due to the τ_A variations between the devices.

Like that of the Θ scan, the sawtooth crash time does not depend on the plasma current; see figure 4.31. Again, most of the scatter is due to variation within a single shot, although no distinction can be made between the before and the after peak current trends. This is the same for discharges before and after the installation of the PF winding. For this set of discharges, the product $(\tau_A \tau_R)^{1/2}$ is ~0.2 ms and is roughly constant over this current region and the $\eta(V_{loop})$ has been used in calculating τ_R. This product is known as the Kadomtsev scaling for the reconnection process to occur for the tokamak sawtooth crash.[44] Even though the MST crash times are larger than the Kadomtsev scaling, they are in agreement in the trend, constant for this current scan. If $S(V_{loop})$

is used to scale the crash time normalized to the Alfvén time, t_{crash} / τ_A, the crash time scales as $S^{0.7}$, see figure 4.32. This comparable to the simulations of Caramana, et al.[45]; who observed the time for their first reconnection to scale as $S^{0.5}$. The second reconnection scaled as S and would probably not be observed in experiments since the field profiles evolve at this same rate. The experimental scaling arises due to the normalization of the crash time to the Alfvén time - the Alfvén time decreases with the current and thus with S for this plasma current scan. These scaling are only presented as a comparison to theoritical results. The *correct* parameter which to scale the period or the crash time to is in reality unknown.

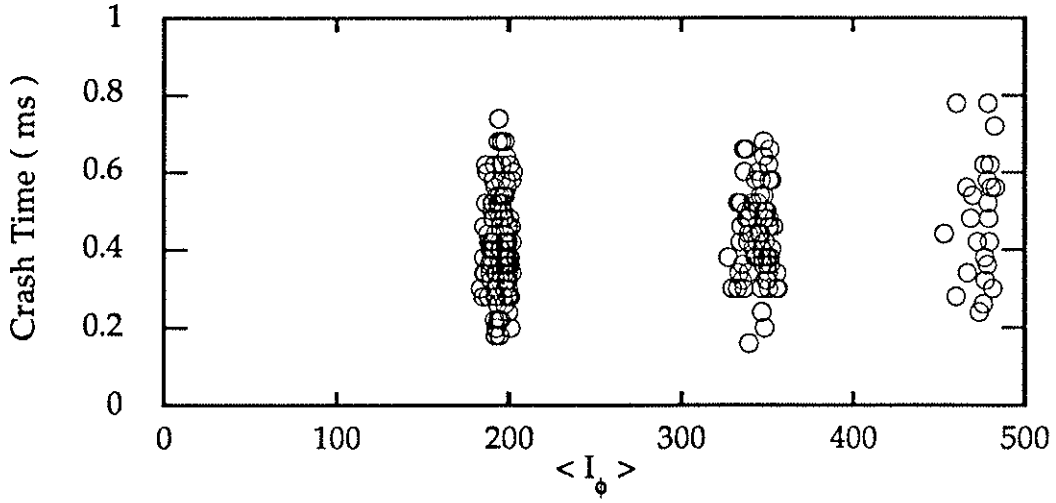

Figure 4.31 The sawtooth crash time does not depend on $< I_\phi >$.

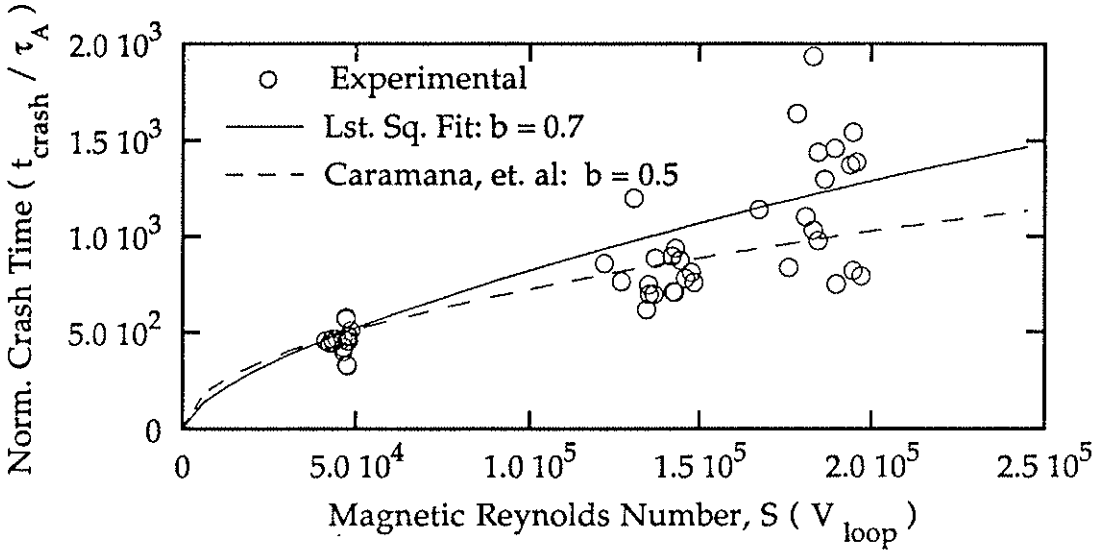

Figure 4.32 The normalized sawtooth crash time versus the magnetic Reynolds number, S. Curves represent the scaling of the data with S, $\frac{t}{\tau_A} \alpha S^b$.

The amount of flux that is created at each sawtooth crash, $\delta\langle B_\phi \rangle$, appears to increase with the plasma current, at least in the scatter if not the trend; see figure 4.33a. This trend is more dramatic in the sawteeth which occur before the peak current than in those which occur afterwards, although the percentage of the flux that is created does not show a strong dependence; see figure 4.33b. This is due to the larger values of $\langle B_\phi \rangle$ at the higher current since Θ was held constant in this scan. The increase of $\delta\langle B_\phi \rangle$ with Θ, which was discussed in section 4.6, is not changed if the percentage of flux is plotted instead of the amount of flux; see figure 4.21a. This is a result of the decrease of $\langle B_\phi \rangle$ as Θ is

increased (the Θ scan was done at constant I_ϕ) which enhances the percentage of flux generated.

As was the case in the Θ scan, section 4.6, no correlation can be made between the period, the crash time, or the amount of flux created.

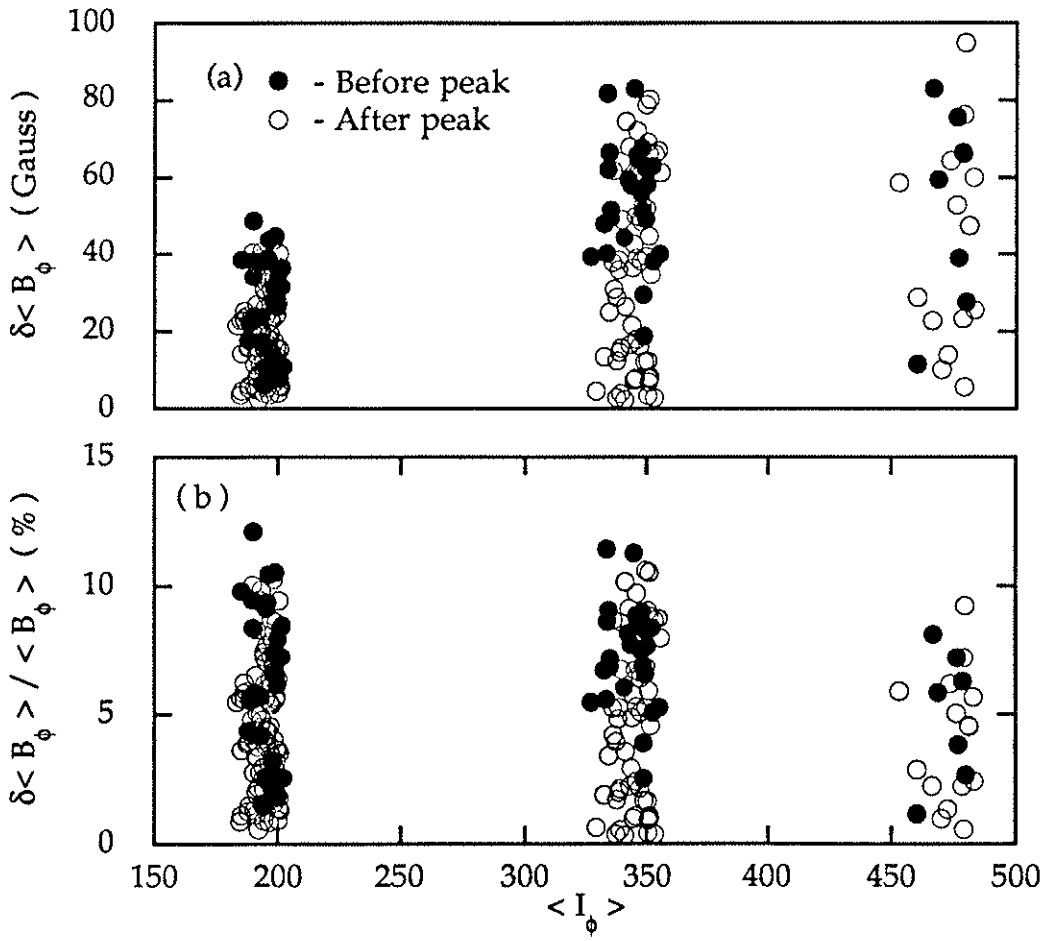

Figure 4.33 (a) The change in the toroidal flux, $\delta\langle B_\phi\rangle$, and (b) the percentage of the flux generated versus the average plasma current during each sawtooth, $\langle I_\phi\rangle$.

4.8 Experimental summary

At this point, a summary of the experimental results will be given. A more detailed summary will be given in chapter 6 along with the overall conclusions of this thesis.

The general characteristics of the MST sawteeth are the same as those observed on other RFPs. The driving mechanism of sawtooth instability is the inward diffusion of the plasma current. As the current diffuses inward, the plasma is *pushed* further away from the relaxed Taylor state - the BFM F-Θ curve; see figure 4.3. This destabilizes the $m = 1$ tearing modes. $m = 1$ precursor oscillations with helicities near $\frac{n}{m} = 2\frac{R}{a}$ are observed in magnetic diagnostics as well as in soft x-ray diagnostics. A broadening of the n-spectrum is observed at the time of the flux jump with n extending into the 100's for the high frequencies. Also initial bispectral calculations in the frequency space show that nonlinear coupling is occuring.

The sawtooth crash flattens the soft x-ray emission profile with inverted sawteeth observed for $r \gtrsim 0.7a$. At the time of the flux jump, a rapid increase in the soft x-ray emission is observed. This increase may be a high energy component, but at this time no energy spectrum of the soft x-ray emission is available. The sawtooth crash flattens the current, the temperature, and the density profiles as well. These profile changes are implied for the MST sawteeth, but they are consistent with the profile changes that have been measured by other RFP groups.

The flux generation is asymmetric suggesting a $m = 0$ type of reconnection. In the MST, the flux jump originates at the poloidal gap suggesting a connection to the magnetic field errors.

As predicted from the theories described in chapter 2, the sawteeth are more dramatic at higher Θ. Both the amount of toroidal flux generated and the period of the sawteeth increase with Θ. The sawtooth period also increases with the plasma current. For the MST, this suggests that the period also increases with the magnetic Reynolds number, S. The experimental scaling is consistent with the theoretical predictions. In both the Θ scan and the current scan, the sawtooth crash time did not scale with either parameter. No correlations can be made between the sawtooth period, the amount of flux created, or the crash time.

In all the experimental parameters that have been observed, for example, the sawtooth period or crash time, there is a wide variety of scatter between discharges and between sawteeth within one discharge. Due to these variations, it is my feeling that to truly understand the sawteeth event, profile changes - magnetic as well as temperature and density - are needed for each event. The general characteristics can be determined by shot averaging, as was done in this thesis, but the individual characteristics of the sawteeth may then be lost.

References

[1]see for example, R. G. Watt, and R. A. Nebel, Phys. Fluids **26**, 1168 (1983).

[2]see for example, Y. L. Ho, Ph.D. thesis, University of Wisconsin-Madison (1988).

[3]R. B. Howell, J. C. Ingraham, G. A. Wurden, P. G. Weber, and C. J. Buchenauer, Phys. Fluids **30**, 1828 (1987).

[4]K. Kusano, and T. Sato, submitted to Nucl. Fusion.

[5]V. Antoni, and S. Ortalani, Phys. Fluids B **30**, 1489 (1987).

[6]P. Schmid, G. Barrick, P. Greene, and S. Robertson, submitted to Phys. Fluids.

[7]see for example, E. J. Caramana, R. A. Nebel, and D. D. Schnack, Phys. Fluids **26**, 1305 (1983).

[8]K. Kusano, T. Sato, H. Yamada, Y. Murakami, Z. Yoshida, N. Inoue, Nuc. Fusion, **28**, 89 (1988).

[9]B. A. Alper, private communication.

[10]R. B. Howell, J. C. Ingraham, G. A. Wurden, P. G. Weber, and C. J. Buchenauer, Phys. Fluids **30**, 1828 (1987).

[11]K. Hattori, Y. Hirano, T. Shimada, Y. Yagi, Y. Maejima, I. Hirota, and K. Ogawa, in *U.S./Japan Workshop on Fluctuations in RFP and ULQ Plasmas*, (March 12-15, 1990, Madison, WI).

[12]see for example, G. L. Jahns, M. Soler, B. V. Waddell, J. D. Callen, and H. R. Hicks, Nuc. Fusion **18**, 609 (1978).

[13]G. A. Wurden, Phys. Fluids **27**, 551 (1984).

[14]G. Chartas, R. N. Dexter, S. A. Hokin, and J. S. Sarff, Bull. of Am. Phys. Soc. **9**, 2106 (1989).

[15]T. D. Rempel, private communication

[16]R. N. Dexter, private communication

[17]R. G. Watt, and E. M. Little, Phys. Fluids **27**, 784 (1984).

[18]D. J. Den Hartog, Ph.D. Thesis, University of Wisconsin-Madison (1989).

[19]see for example, I.H. Hutchinson, *Principles of Plasma Diagnostics* (Cambridge Univ. Press, Cambridge 1987), p. 27-30.

[20]see for example, V. D. Shafranov, in *Reviews of Plasma Physics* **2** (Ed. M. A. Leontovich, Consultants Bureau, New York), p. 130.

[21]V. Antoni, P. Martin, S. Ortolani, Plasma Physics Contr. Fusion **29**, 279 (1987).

[22]N. Asakura, A. Fujisawa, R. Fujita, Y. Fukada, H. Hottori, N. Inoue, S. Ishida, K. Itami, Y. Iwata, H. Ji, Y. Kamada, K. Kusano, S. Matsuzuka, K. Miyamoto, J. Morikawa, C.P. Munson, Y. Murakami, Y. Nagayama, H. Nihei, S. Onodera, M. T. Saito, T. Sato, S. Shinohara, H. Toyama, Y. Ueda, M. Utumi, and H. Yamada, in *Plasma Physics and Contolled Fusion Research*, 1986, Proceedings of the 11th International Conference, Kyoto (IAEA, Vienna, 1987), Vol. 2, p. 433.

[23]D.C. Robinson, Nucl. Fusion **18**, 939 (1978).

[24]see for example, J. P. Friedberg, Rev. Mod. Phys. **54**, 801 (1982).

[25]V. Antoni, D. Merlin, S. Ortolani, and R. Paccagnella, Nucl. Fusion **26**, 1711 (1986).

[26]R. A. Nebel, private communication

[27]R. B. Howell, J. C. Ingraham, G. A. Wurden, P. G. Weber, and C. J. Buchenauer, Phys. Fluids **30**, 1828 (1987).

[28]*Ibid.*, p. 1830.

[29]*Ibid.*, p. 1836.

[30]see for example, E. J. Caramana, R. A. Nebel, and D. D. Schnack, Phys. Fluids **26**, 1305 (1983).

[31]see for example, R. G. Watt, and R. A. Nebel, Phys. Fluids **26**, 1168 (1983).

[32]S. Assadi, private communication.

[33]K. Hattori, T. Shimada, Y. Hirano, Y. Yagi, and K. Ogawa, submitted to Phys. Rev. Lett.

[34]see for example, E. J. Caramana, R. A. Nebel, and D. D. Schnack, Phys. Fluids **26**, 1305 (1983).

[35]see for example, V. Antoni, and S. Ortolani, Phys. Fluids **30**, 1489 (1988).

[36]R. J. Hayden, and B. Alper, Plasma Physics Contr. Fusion **31**, 193 (1989).

[37]P. Schmid, G. Barrick, P. Greene, and S. Robertson, submitted to Phys. Fluids.

[38]V. Antoni, and S. Ortolani, Phys. Fluids **30**, 1489 (1988).

[39]see for example, I. H. Hutchinson, *Principles of Plasma Diagnostics* (Cambridge Univ. Press, Cambridge 1987), p. 18.

[40]D. J. Den Hartog, private communication.

[41]J.C. Sprott, Phys. Fluids **31**, 2266 (1988).

[42]R. A. Nebel, private communication

[43]B. Alper, and P. Martin, Proc. 16th European Conf. on Controlled Fusion and Plasma Physics - Venice, Italy March 13-17 '89.

[44]B. B. Kadomtsev, Fiz. Plasmy **1**, 710 (1975) [Sov. J. Plasma Phys. **1**, 389 (1975)].

[45]E. J. Caramana, R. A. Nebel, and D. D. Schnack, Phys. Fluids **26**, 1305 (1983).

CHAPTER 5

MODELING OF THE SAWTOOTH RISE-TIME

As discussed in the previous chapters, the toroidal field is decaying classically during the rise-time of the sawtooth. This interval has been shown to be a purely resistive process by Werley, et. al. on the ZT-40M RFP.[1] Using a 1-D transport code, the ZT-40M sawtooth rise-time was successfully modeled without the inclusion of any dynamo term. In an attempt to further characterize the MST sawteeth and make a comparison with the ZT-40M sawteeth, this same code was applied to the MST sawteeth. Due to the similarities between the MST simulation and that of Werley, et al., this chapter will follow the general outline of reference 1. Section 5.1 will give a brief overview of the transport code and the assumptions that were made. The results of the MST simulations will be presented in section 5.2. Finally, comparisons with the ZT-40M simulations will be made in section 5.3.

5.1 Description of the 1D transport code

The simulation of the sawtooth rise-time is carried out using a 1-D cylindrical transport code.[1] The plasma and the magnetic configurations are evolved through a series of equilibrium states. The transport equations are listed in table 5.1. For these simulations, only one ion,

hydrogen, was used. The initial conditions and boundary conditions for the rise-time simulations are summarized in table 5.2.

Since no profile information is available for the plasma temperature or the plasma density for the MST, profiles of the form $f(r) = f(0) \{ 1 - \alpha (r/a)^{\beta} \}$ were used. The central values, $n_e(0)$ and $T_e(0)$, were set by the experimentally measured Thomson scattering data. To match the experimental particle confinement times, an anomalous diffusion coefficient is used. This diffusion coefficient is specified by a fraction of the Bohm diffusion. To maintain the density profile shape and its central value, a 1-D slab geometry code for neutral transport called SPDNUT is used. This code, which is included in the transport code, uses an edge neutral source to fuel the plasma. The source profile is calculated from charge exchange and ionization rates based on the simulated plasma properties. To maintain the temperature profile, the thermal conductivity was adjusted to keep $T_e(0)$ constant during the MST simulation. Also, the initial ion temperature was set equal to the electron temperature. As discussed in section 4.3, Watt and Little[2] have been able to measure the electron temperature evolution during a sawtooth crash for the ZT-40M device. For this reason, Werley, et al. allow the central temperatures to evolve according to the experimentally measured values of $T_e(0)$. The implications of this assumption will be discussed in section 5.3. The shape of the profiles used in the MST simulations will be discussed in section 5.2.

Table 5.1 Transport equations used in the sawtooth rise-time simulations

Continuity (ions)	$\dot{n} + \nabla \cdot (n\vec{V}) = 0$
Energy Conservation (ions and electrons)	$\frac{3}{2} n (\dot{T} + \vec{V} \cdot \nabla T) + P \nabla \cdot \vec{V} = \nabla \cdot K \nabla T + Q$
Faraday's Law	$\dot{\vec{B}} = - \nabla \times \vec{E}$
Generalized Ohm's Law	$\vec{E} = - \vec{V} \times \vec{B} + \overleftrightarrow{\eta} \vec{J} + \frac{1}{en_e} \vec{R_T}$
Ampere's Law	$\vec{J} = \frac{1}{\mu_o} \nabla \times \vec{B}$
Pressure Balance	$\nabla P = \vec{J} \times \vec{B}$
Equation of State	$P = \sum_i n_i T_i + n_e T_e$
Quasi Neutrality	$\sum_i Z_i n_i = n_e$
and	$Q_i = Q_{equilibration}$
	$Q_e = (\overleftrightarrow{\eta} \vec{J}) \cdot \vec{J} + \frac{1}{en_e} \vec{R_T} \cdot \vec{J} - P_{rad} - Q_i$
	$P_{rad} = P_{cyclotron} + P_{Bremsstrahlung}$

Table 5.2 Initial profiles and boundary conditions used in the sawtooth rise-time simulations on MST.

density	$n_e(r) = n_e(0)\ \{\ 1 - 0.8\ (r/a)^8\ \}$
	$n_e(0,t) =$ constant
Temperature	$T_e(r) = T_e(0)\ \{\ 1 - 0.8\ (r/a)^6\ \}$
	$T_i(\ r, 0\ ) = T_e(\ r, 0\ )$
	$T_e(0,t) =$ constant
Magnetic profiles	$\lambda(r) = \lambda_o\ (\ 1 + a_6\ r^6 + a_8\ r^8\ )$
Applied toroidal voltage	$V_\phi(t) = V_\phi(0) + b_1\ t$
Toroidal magnetic field at the wall	$B_\phi(a,t) = B_\phi(a,0) + b_2\ t$
	or
	$B_\phi(a,t) = B_\phi(a,0) + \beta\ e^{-\alpha t}$

The initial magnetic field profiles are obtained by expanding the λ profile ($\lambda = \mathbf{J} \cdot \mathbf{B}\ /\ B^2$) as a power series in $(r/a)^2$. The λ profile and the toroidal field strength on axis, $B_\phi(0)$, are varied to match the initial edge magnetic fields and the toroidal flux of the experiment, and thus to match the initial experimental F, Θ, and $\langle B_\phi \rangle$ values.

The boundary conditions used in the simulations are summarized in table 5.2. They include the toroidal magnetic field at the wall, $B_\phi(a,t)$ and the externally applied toroidal voltage, $V_\phi(t)$. The toroidal voltage is evolved linearly in time. Two types of boundary conditions were used for $B_\phi(a,t)$, as shown in table 5.2. The form of the time dependence was chosen to best match the experimental $B_\phi(a,t)$ evolution. The exponential time dependence fit was primarily used for the MST sawteeth, while the linear dependence was used for the ZT-40M sawteeth.[1] The coefficients b_1 and either b_2 or β and α, are determined by fitting the experimental evolution of $V_\phi(t)$ and $B_\phi(a,t)$ to the appropriate curve.

To match the time evolution of the discharge, the resistivity profile is used as a free parameter. This was chosen since the experimental resistivity is unknown, either its profile or its connection to the temperature or other plasma parameters. This is accomplished by using an effective temperature profile, $T_\eta(r)$, to calculate a "Spitzer" resistivity, $\eta(T_\eta, Z_{eff})$. The effective temperature profile is given by

$$T_\eta(r) = T_e(0) \{ 1 - c_1 [1 - \exp(- c_2 (\frac{r}{a})^2)] \}$$

$$\text{and } c_1 = [1 - T_\eta(a)/T(0)] / [1 - \exp(- c_2)].$$

This effective temperature profile is used in place of the plasma temperature in calculating the Spitzer resistivity[3]

$$\eta(T_\eta, Z_{eff}) = \eta_{Spitzer} * \left(\frac{T_e(r)}{T_\eta(r)} \right)^{3/2}$$

$$\eta_{Spitzer} = \frac{\pi\, e^2\, m_e^{1/2}}{(4\pi\, \varepsilon_o)^2} Z_{eff} \ln \Lambda\, T_e(r)^{-3/2}$$

$$\text{and } Z_{eff} = \text{const.}$$

The use of this resistivity results in three free parameters, c_2, $T_\eta(a)/T(0)$ and Z_{eff}, which are used to match the temporal evolution of the experimental I_ϕ and $< B_\phi >$. The parameter c_2 controls the shape of the resistivity profile, $T_\eta(a)/T(0)$ controls the relative resistivity near the wall, and Z_{eff} controls the magnitude. In these simulations, Z_{eff} is constant across the radius, and all three parameters are held constant during a simulation. The parameters $T_\eta(a)/T(0)$ and Z_{eff} are first varied to match the decay of the toroidal flux. Then the toroidal current is matched by varying c_2.

As will be shown below, a strong gradient in the resistivity is required in the center of the discharge in order to match the experimental time evolution.

5.2 Results on the MST

The rise-time of the MST sawteeth can modeled with the 1-D transport code. One such example is shown in figure 5.1. This section will describe the characteristics of these simulations.

For the MST, the initial temperature and density profiles are listed in table 5.2. The constraints of matching the experimental particle

confinement times (~ 1 msec),[4] and holding the central density and temperature constant resulted in the respective profiles. If either the density or temperature profile was varied, either a sharper fall off or a flatter profile in the case of the temperature, the constraints used would quickly evolve the profiles to those listed. This is primarily a result of the limited experimental measurements for the MST particle confinement time and the thermal conductivities. Since the simulations are only matching the magnetic evolution of the discharge, the temperature and density profile variations are not believed to strongly influence the results. The types of profiles used for these simulations are consistent with the initial results of 1-D quasi steady-state transport simulation recently performed by Veerasingam and Nebel for the MST RFP.[5]

To match the experimental data shown in figure 5.1, the simulation required [c_2, $T_\eta(a)/T(0)$, Z_{eff}] = [7.0, 0.25, 2.0]. The effective temperature profile, $T_\eta(r)$, for this simulation is shown in figure 5.2, along with the resulting resistivity profile. For comparison, the results of a flat resistivity profile, $T_\eta(a)/T(0) = 1.0$, are also plotted in figure 5.1. Although the experimental toroidal flux is matched, the plasma current increases for the flat resistivity. Also plotted in figure 5.1 and in figure 5.2 are the results of a simulation with the resistive gradient farther out in the edge of the discharge, [c_2, $T_\eta(a)/T(0)$, Z_{eff}] = [0.25, 0.25, 2.0]. This type of resistivity profile is expected if the resistivity

were classical, that is Spitzer. Again, the toroidal flux decay is matched, but the plasma current increases.

In all cases, the $B_\phi(a)$ signal is matched due to the boundary condition applied. In the three cases shown in figure 5.1, the toroidal flux decay is reproduced within the experimental noise. The flux does increase slightly for the "flat resistivity" case, but still within the noise. In the other two cases shown, $T_\eta(a)/T(0)$ and Z_{eff} have the same values. These two parameters are used together in matching the experimental flux decay. If a higher Z_{eff} is used, $T_\eta(a)/T(0)$ must also increase which keeps the edge resistivity at the level required to match the decay of the toroidal flux. Once the toroidal flux evolution is simulated, the parameter c_2 is used to match the plasma current evolution. In the case of the simulation shown in figure 5.1, a lower value of c_2, $c_2 = 6$ or below, would increase the current, while a higher value would cause it to decay. If Z_{eff} is made too large, typically ~ 5, $T_\eta(a)/T(0)$ can still be adjusted to match the toroidal flux, but the plasma current cannot be matched. This is similar to the flat resistivity simulation. For several simulations run for the MST, the resistivity has the general shape of that shown in figure 5.2b - slight variations are needed for each simulation, $c2 = 6 - 10$ and $T_\eta(a)/T(0) = 0.20 - 0.35$ for $Z_{eff} = 2.0$, but all required an anomalous resistivity.

The *high* edge resistivity causes the plasma current to diffuse radially inward. This is shown in figure 5.3 where the initial and final

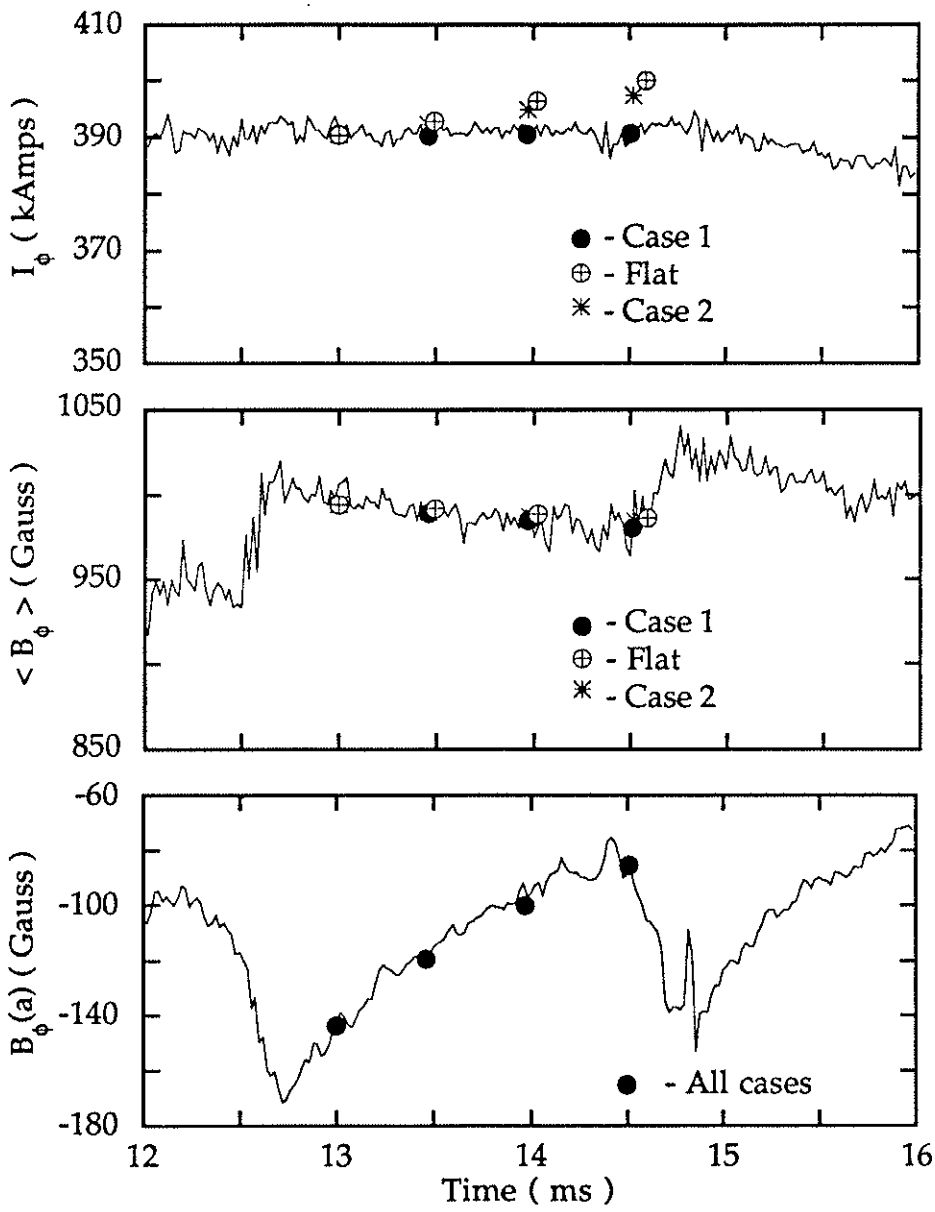

Figure 5.1 A sawtooth oscillation during the initial operation of MST. The simulated data points are also shown for

Case 1: [c_2, $T_\eta(a)/T(0)$, Z_{eff}] = [7.0, 0.25, 2.0],

Flat: [7.0, 1.0, 2.0] and Case 2: [0.25, 0.25, 2.0]

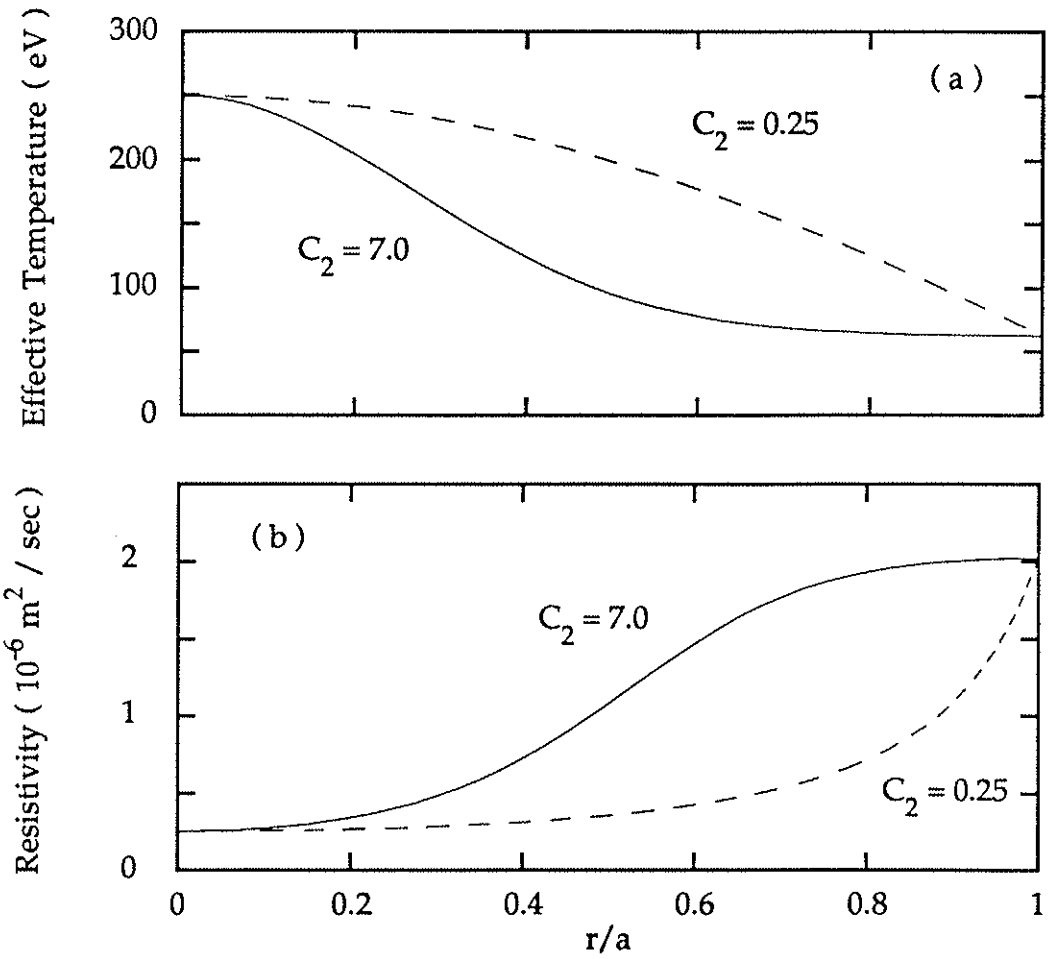

Figure 5.2 (a) The effective temperature profiles and (b) the resulting resistivity profiles required to match the experimental data in Fig. 5.1, $c_2 = 7.0$, and a classical-like profile, $c_2 = 0.25$.

(t = 1.5 ms) current densities are plotted for the MST simulation. The inward *shift* of the plasma current causes the magnetic pitch ($P = r B_\phi / B_\theta$) on axis to decrease; see figure 5.4. This is analogous to the lowering of the central q value discussed in section 4.3 ($q = P / R$). In

this simulation, the central q value does not drop dramatically but does decrease from 0.22 to 0.21. This is comparable to the lower limit set by Antoni, et al.[6] of $\frac{2}{3}\frac{R}{a} \approx 0.23$.

In this simulation, the experimental data could be matched until the time of the next sawtooth crash. As described in section 4.1, the m = 1 precursors are observed in experiments prior to the sawtooth crash. The lowering of the central pitch causes the m = 1 tearing modes to become unstable. This effect has been checked by doing a stability analysis on the simulated λ profiles, and indeed the m = 1, n = 6 - 8 tearing modes begin to become unstable by about 0.5 ms for this simulation.

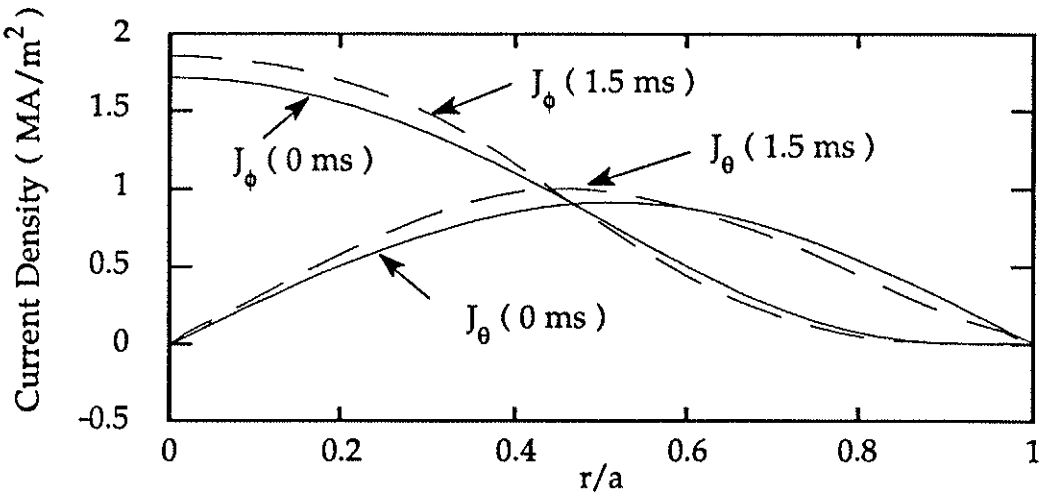

Figure 5.3 The initial and final simulated current density profiles for the simulation shown in Fig. 5.1.

The simulation shown here is a sample of the simulations which have been performed for the MST device. The results of other simulations are similar, with only modest differences in the free parameters required to match the experimental evolution. Due to the limited availability of the Thomson scattering diagnostic on the MST, the simulations have only been done on high-Θ sawteeth. It has not been determined if the 1-D simulation models the nonreversed sawteeth as well. Likewise, due to the higher Θ values in the MST after the installation of the PF winding, difficulties in fitting the λ profile to obtain the experimental F and Θ values have hampered simulations. At this point, no comparisons can be made between the discharges before and after the PF winding installation.

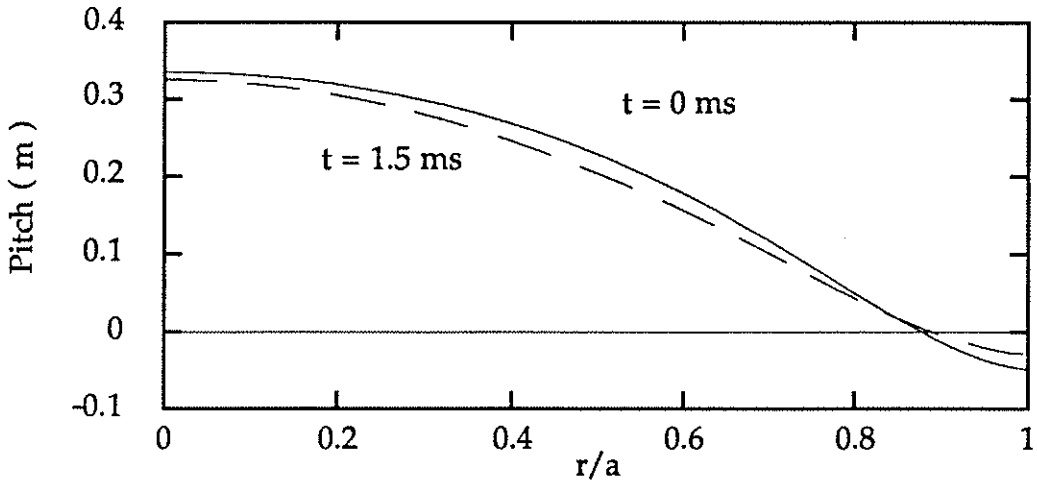

Figure 5.4 The initial and final simulated pitch profiles for the simulation shown in Fig. 5.1.

5.3 Comparison with ZT–40M results and discussion

The results of the ZT-40M simulations will be discussed in this section. Although the simulations have been carried out for different discharge characteristics, the results of the simulations are very similar. References 1 and 7 can be seen for a more detailed discussion of the ZT-40M results.

To match the ZT-40M sawtooth characteristics, Werley, et al. used the free parameter set of $[c_2, T_\eta(a)/T(0), Z_{eff}] = [12.0, 0.25, 2.0]$. The effective temperature and resistivity profile for this simulation are shown in figure 5.5. These profiles are similar to the profiles used in the MST simulations, also plotted in figure 5.5 for comparison. Once again, the current density diffuses radially inward lowering the central magnetic pitch. The peaking of the current density is a stronger effect in the ZT-40M simulations than in those of MST, as illustrated in figure 5.6.

As mentioned in section 5.1, the $T_e(0)$ was allowed to evolve between the limits of the Thomson scattering measurements for the ZT-40M simulations, and it was held constant for the MST simulations. If the temperature is allowed to evolve within the error of the experimental data for the MST simulations, a slight variation in the resistivity profile was required. For the simulation shown in figure 5.1, the experimental central temperature was $T_e(0) = 270 \pm 50$ eV, and the parameter set $[c_2, T_\eta(a)/T(0), Z_{eff}] = [8.0, 0.20, 2.0]$ was required if the temperature was

allowed to evolve from 220 to 320 eV. A slight increase in the current density is observed over that of the previous simulation, but still the strong peaking of the ZT-40M profiles is not observed. At this point, there is no reason to suspect either result, either not enough peaking of the current in MST or that the ZT-40M simulations are over-peaked. Both show the current diffusing radially inward which causes the plasma to become unstable to the $m = 1$ tearing modes. To truly understand if the simulations are correct, the 1-D model will have to be applied to a discharge where the current profiles are known throughout the sawtooth rise-time.

In an attempt to determine if the resistivity profile used in the simulations was caused by either classical or anomalous effects, Nebel, et al.[7] have applied the 1-D simulations to low-Θ discharges without sawteeth, as well as high-Θ discharges. The 1-D model was not able to successfully describe the low-Θ discharges regardless of the resistivity profile. This is similar to the original transport simulations of Caramana and Baker.[8] These discharges appear to have a continuous dynamo mechanism. In high-Θ discharges where the electron density was increased (~ 60% increase in the line-averaged density over *normal* high-Θ operation), the coherent sawtooth activity was not present. Although the fluctuation level of the F and Θ curves was higher than those of the low-Θ discharges, no coherent structure was present. With results similar to the low-Θ discharges, this type of discharge could not be modeled using the 1-D code. It also appears to have a more continuous

dynamo mechanism. In low-density, high-Θ discharges, sawteeth were evident, and the rise-times could be modeled with the 1-D transport code. The dynamo appears to occur only during the sawtooth crash.

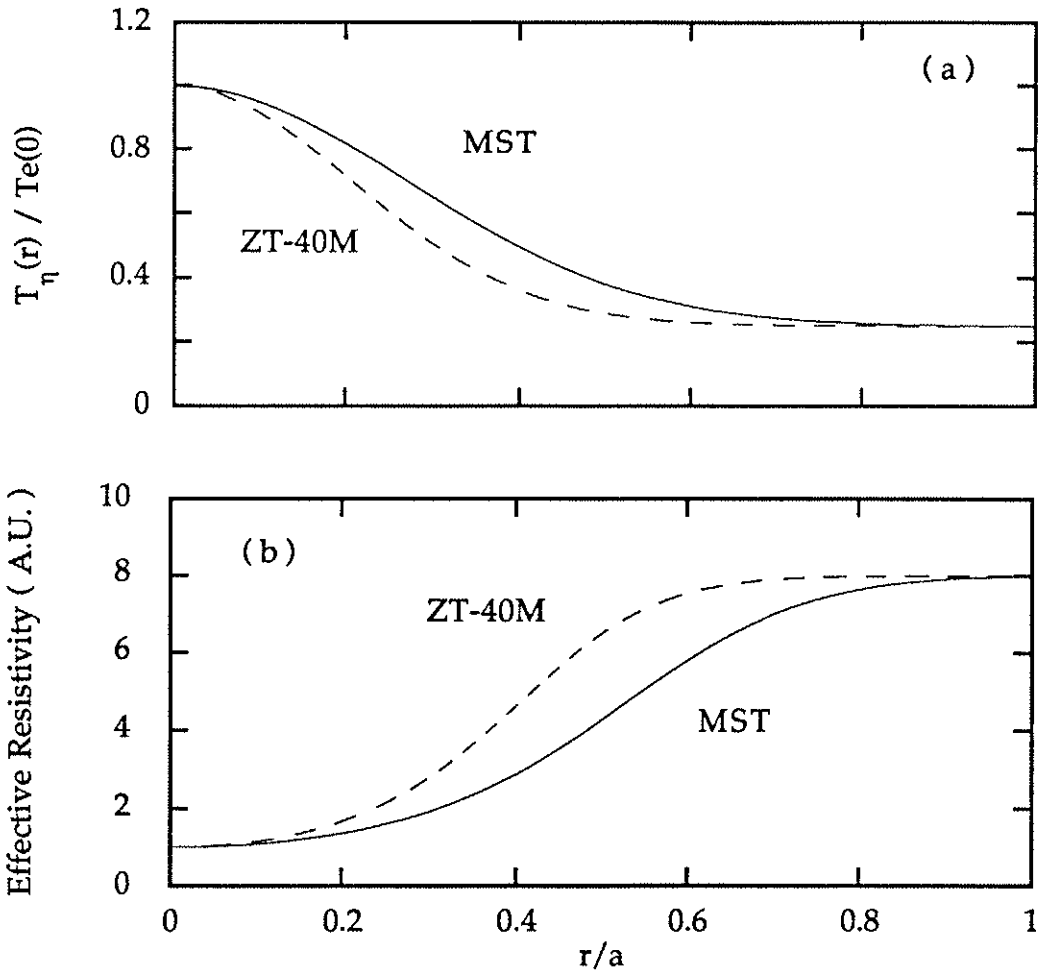

Figure 5.5 Comparison between (a) the effective temperature profiles and (b) the effective resistivities required to match the ZT-40M and MST sawtooth rise-times.

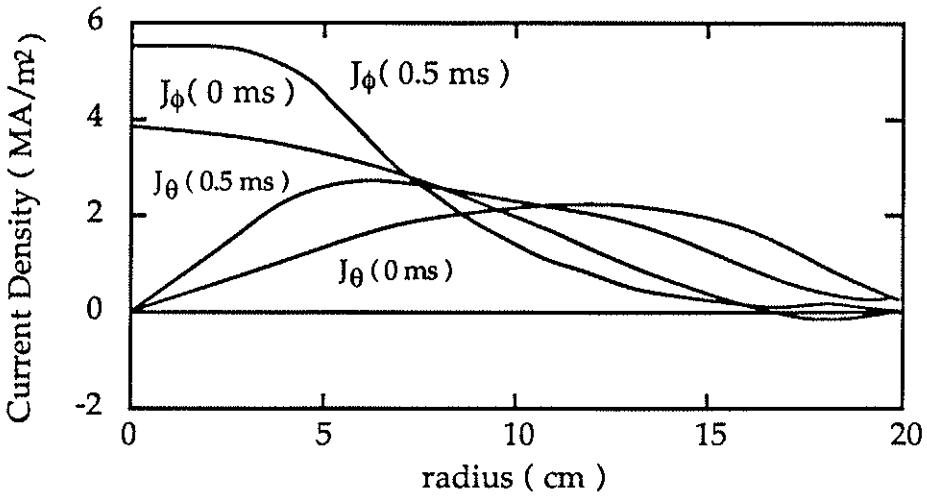

Figure 5.6 The initial and final current density profiles from the ZT-40M sawtooth simulation (adapted from Ref. 1).

In the high-Θ discharges where sawteeth were present, the streaming parameter was large, ~ 25%. The streaming parameter, ξ, is defined as the ratio of the electron drift velocity, $V_{De} = J_{||} / (en_e)$, to the electron thermal velocity, $V_{th} = \sqrt{kT_e / m_e}$. The streaming parameter in the high-Θ discharges without the sawteeth was ~ 15%. The streaming parameter for these simulations is calculated using the Thomson scattering temperature and density, while $J_{||}$ is determined from the λ profiles used to fit the experimental F and Θ values. A high streaming parameter, $\xi \approx 0.2$, would result in a large population of *slideaway* electrons which could provide a source of the anomalous resistivity.[9]

To obtain the higher densities, pulse discharge cleaning in conjunction with gas puff fueling was used to raise the density throughout the discharge. The higher density would decrease the

streaming parameter, thus affecting the anomalous resistivity. However, the gas puff fueling cools the edge of the discharge increasing the resistivity gradient and enhancing the sawtooth activity. The streaming parameter was lowered, and the sawteeth were suppressed. This would suggest that the resistivity is anomalous, not classical.

For the MST simulation discussed in section 5.2, the streaming parameter is ~ 30%, comparable to the high-Θ discharge of ZT-40M. Attempts have been made to increase the density of MST by neutral gas puffing, up to central densities of 3×10^{13} cm^{-3}. No suppression of the sawteeth has been observed. At the high densities, the discharges start to degrade so alternative fueling methods are being investigated. The slideaway electrons, which could be present as a result of the high streaming parameter, could generate the high-energy component of the soft x-ray signals discussed in section 4.4.

In summary, the sawtooth rise-time can be modeled by a 1-D transport code on both the ZT-40M RFP and the MST RFP. On the ZT-40M RFP, low-Θ discharges which do not have sawteeth, and high-Θ discharges with the sawteeth suppressed, cannot be successfully modeled. This supports the claim that the dynamo mechanism is only occuring during the sawtooth crash, and that the dynamo is more continuous in the ZT-40M discharges where the sawteeth are not present. To match the experimental time evolution, a strong gradient in the central resistivity profile was required. The high streaming parameter derived

from the simulations could be the cause of the anomalous resistivity required to simulate the sawtooth rise-times on both ZT-40M and MST. Sawteeth have been *suppressed* in the ZT-40M device by increasing the electron density which in turn lowers the streaming parameter. Increasing the density may be a method of suppressing the sawteeth on the MST, although so far no success has been achieved with the present fueling capabilites of the MST device which has a plasma radius ~2 times larger than ZT-40M.

References

[1]K. A. Werley, R. A. Nebel, and G. A. Wurden, Phys. Fluids **28**, 1450 (1985).

[2]R. G. Watt, and E. M. Little, Phys. Fluids **27**, 784 (1984).

[3]L. Spitzer, Jr., *Physics of Fully Ionized Gases* (Wiley, New Uork, 1962), p. 73.

[4]S. A. Hokin, private communication.

[5]R. Veerasingam, private communication.

[6]V. Antoni, D. Merlin, S. Ortolani, and R. Paccagnella, Nuc. Fusion **26**, 1711 (1986).

[7]R. A. Nebel, K. A. Werley, and M. M. Pickrell, Los Alamos National Laboratory Report LA-10653-MS (1986).

[8]E. J. Caramana, and D. A. Baker, Nuc. Fusion **24**, 423 (1984).

[9]R. A. Nebel, K. A. Werley, and M. M. Pickrell, Los Alamos National Laboratory Report LA-10653-MS (1986) p. 18.

CHAPTER 6

CONCLUSIONS AND FUTURE PROSPECTS.

In this chapter, the conclusions of this thesis will be presented, as well as possible extensions to this research. Many of the conclusions presented in section 6.1 are similar to those presented by other theoretical and experimental groups around the world, many of whom have made valuable contributions to this research. In section 6.2, possible areas of future work in the RFP and particularly those related to the RFP sawteeth will be presented. Many of these are vital to the success of the RFP program as a whole, as well as to understanding the nature of the RFP sawtooth.

6.1 Conclusions

The RFP sawteeth are discrete dynamo events. Each sawtooth consists of a slow diffusion away from the minimum energy state - the BFM curve or a similar model such as the PFM - and a rapid relaxation back towards the relaxed state. The dynamo mechanism occurs only during the relaxation process, the sawtooth crash.

The rise-time of the sawtooth is a purely resistive process. This has been modeled using a 1-D transport code without the inclusion of a dynamo mechanism. To match the experimental time evolution of the plasma, an anomalous resistivity was required. Similar results have

been obtained for the ZT-40M sawteeth.[1] The anomalous resistivity is believed to be a result of a high value of the streaming parameter, V_{De} / V_{th}.[2] The streaming parameter observed, 25 - 30%, could result in a significant population of "slide-away" electrons leading to an anomalous resistivity. On the ZT-40M, the high streaming parameter has been reduced by operating at a higher density than used during normal, low-Θ operations. The use of this technique on the MST has not resulted in a suppression of the sawteeth. This may be a result of the limited fueling capacity currently available.

During the rise-time of the sawtooth, the current density diffuses radially inward, lowering the central magnetic pitch. This destabilizes the plasma to the m = 1 tearing modes. These "precursor" modes are observed to grow prior to a sawtooth crash. Their helicities are consistent with simulations which predict the m = 1, n = 2R/a tearing mode to be the dominant mode in the RFP.[3]

Initial experimental results indicate that nonlinear coupling of the m = 1 modes is occurring during the sawtooth crash. These observations are consistent with MHD simulations; see sections 4.5 and 2.2. At this time, it can not be experimentally determined if the maintenance of the reversed field is due to the reconnection of the m = 1 modes or the m = 0 modes (the m = 0 modes can be a result of the nonlinear coupling of the m = 1 precursor modes).

The sawtooth crash results in a rapid relaxation of the plasma back towards the minimum energy state. This relaxation flattens many of the plasma profiles, including the current, the temperature, and the density. As a result, the plasma is once again stable to the m = 1 tearing mode. Many of these profile modifications are only inferred for the MST, but the experimental observations are consistent with measured profile changes measured by other RFP groups; see section 4.3.

As predicted by the MHD simulations,[4] the sawtooth activity increases with Θ. This is believed to be due to the stabilization of the m = 1 modes by the conducting wall. At higher values of Θ, the m = 1 resonant surfaces are further from the wall, thus allowing these modes to grow larger in amplitude resulting in their interaction being more severe. Likewise, simulations indicate that the sawteeth are more prevalent in a low aspect ratio device like MST than in a larger aspect ratio device like ZT-40M.[5] Again, this is a result of the fact that the m = 1 modes are able to grow to a larger amplitude before they interact.

Since the rise-time of the sawteeth is purely a resistive process, the period should increase inversely with the plasma resistance. This has been observed numerically,[5] and experimentally on MST, as well as on a device to device comparison.[6]

No correlation between the sawtooth period, the amount of flux generated at each sawtooth crash, and the crash time can be made at this

time. Thus, a longer period does not result in a more severe sawtooth crash.

While other RFP devices must operate at high values of Θ, typically $\Theta > 1.6$, to observe the sawtooth activity, sawteeth are present at all values of Θ in the MST. A sawtooth-like event is also observed for nonreversed discharges. At this time, it is not known experimentally whether the underlying physics of this event is the same as the sawteeth observed in reversed discharges. However, 3-D simulations indicate that the $m = 1$ modes are responsible for the oscillations, but the nonlinear coupling is not required in the nonreversed discharges.[7]

A variety of reasons for the prevalence of the sawteeth on the MST have been stated throughout this thesis, many of the responsible features may be able to be eliminated; the prospects for eliminating these will be discussed in the next section on proposed future work.

For this thesis, the general features of the RFP sawteeth have been characterized. It was hoped that due to the dominant nature of the sawteeth in MST, a great deal of insight could be presented as to the nature of the RFP sawtooth event. This was not the case, primarily due to the limited diagnostics currently available on MST. All observations indicate that the RFP sawtooth crash is a discrete dynamo event and is the only occurrence of the dynamo in this type of discharge. The driving mechanism behind the RFP sawtooth is similar to that of the Tokamak sawtooth; namely, the inward diffusion of the current density. This

lowers the central safety factor, q(0), and causes the plasma to become unstable to the m = 1 tearing modes.

6.2 Suggestions for Future Work

This section will discuss possible extensions of the research performed for this thesis. Many of these proposals pertain to the MST device directly, and many of them pertain to the RFP configuration in general. All of the proposals are aimed at extending the knowledge of the RFP sawtooth event, but many of them are required to understand the RFP plasma in general.

The most obvious choice is to determine why the sawteeth are so prevalent in the MST RFP in comparison with other RFP devices. Several possibilities have been mentioned throughout this thesis; examples include the low aspect ratio of MST, a high streaming parameter, and the field errors which still remain. The effect of the low aspect ratio cannot be eliminated with the present configuration. However, if the proposed limiter studies are carried out on the MST, the aspect ratio dependence can be determined, although there will be the added effect of the stabilization of the distant wall on the plasma's performance.[8]

The high streaming parameter has been reduced on the ZT-40M device. It may also be able to be controlled on the MST with an

improved fueling system. The use of pellet injection may increase the on-axis density thus lowering the streaming parameter.

The flux generation starting at the poloidal gap on the MST suggests a connection to the magnetic field errors still present. While there has been significant plasma improvement with the installation of the PF winding, the sawteeth still remain and appear to be influenced by the poloidal gap. With the continued success in the reduction of the field errors, it will be interesting to find out if the initiation of the flux generation moves away from the gap region and becomes random such as occurs in other RFPs.

While the magnetic field profiles have been measured on other RFP devices, no such measurements have been successful on the MST except for the edge region. Due to the high temperatures involved, these profiles may not be able to be determined by the conventional technique of magnetic pickup coils. Understanding how the profiles evolve in the rise-time of the sawtooth, as well as in the sawtooth crash, is essential to understanding the RFP sawtooth. This has been investigated on smaller devices, but how do the profiles of MST compare to the smaller devices? Are the profiles on MST similar to other RFPs as has been assumed, or are they slightly different which may cause the sawteeth to be more dominant?

Not only are the magnetic profiles required to understand the evolution of the instabilities which drive the sawtooth, but the plasma

temperature and density profiles are required to understand the sawtooth's influence on transport. Are the sawteeth "bad things" which destroy the confinement of the RFP, or are they a central perturbation which redistributes the plasma energy as in the case of the Tokamak sawteeth (this does not include the major disruptions observed in Tokamaks)? The RFP sawteeth are probably a more detrimental perturbation since the tearing modes involved are resonant farther out in the plasma; thus, the influence of the sawteeth on the edge confinement may be more severe.

As mentioned in chapter 4, MST tends to operate at a higher Θ value than other devices. At this time, this can not be explained as being due to errors in the measurements of the toroidal flux and the plasma current. The MPFM can match the F-Θ trajectory, but this requires a higher β than is expected from Thomson scattering measurements.[9] Again, no profiles are known for the MST to accurately determine β.

A key measurement that is needed, particularly for the MST, is the soft x-ray energy spectrum; not only the equilibrium spectra, but the spectra evolution during a sawtooth crash. Are the large excursions in the soft x-ray emission due to a high energy component, or are they due to variations in the equilibrium distribution?

In conclusion, what if the question were to be posed the other way around, "why are sawteeth not observed at lower values of Θ" ? The MHD simulations show that the process is occurring, and indeed, the

reversal is maintained in the experiments. Profile information is needed to answer the question of why the "continuous" dynamo process is "suppressed" during the rise-time of the sawtooth for high-Θ discharges, but is able to occur at lower values of Θ.

References

[1]K. A. Werley, R. A. Nebel, and G. A. Wurden, Phys. Fluids **28**, 1450 (1985).

[2]R. A. Nebel, K. A. Werley, and M. M. Pickrell, Los Alamos National Laboratory Report LA-10653-MS (1986).

[3]see for example, Y. L. Ho, Ph.D. thesis, University of Wisconsin-Madison, 1988.

[4]see for example, E. J. Caramana, R. A. Nebel, and D. D. Schnack, Phys. Fluids **26**, 1305 (1983).

[5]K. Kusano, and T. Sato, submitted to Nucl. Fusion.

[6]B. Alper, and P. Martin, Proc. 16th European Conf. on Controlled Fusion and Plasma Physics - Venice, Italy March 13-17 '89.

[7]K. Kusano, T. Sato, H. Yamada, Y. Murakami, Z. Yoshida, N. Inque, Nuc. Fusion, **28**, 89 (1988).

[8]Y. L. Ho, Ph.D. thesis, University of Wisconsin-Madison, 1988.

[9]J. C. Sprott, private communication.